SPECinc
stratton park engineering company inc
cloud physics and instrumentation

NASA NRA Final Report

on

A New Digital Holographic Instrument for Measuring Microphysical Properties of Contrails in the SASS (Subsonic Assessment) Program

Submitted to the:

National Aeronautics and Space Administration
Ames Research Center
Moffett Field, CA 94035-1000

NASA SASS Contract Number NAS2-14258
December 7, 2000

5401 Western • Boulder, CO 80301 • 303-449-1105
FAX: 303 449-0132

SPECinc
stratton park engineering company inc
cloud physics and instrumentation
5401 Western Ave., Boulder, Colorado 80301, Tel (303) 449-1105, Fax (303) 449-0132

Final Report
NASA SASS Contract No. NAS2-14258

A New Digital Holographic Instrument for Measuring Microphysical Properties of Contrails in the SASS (Subsonic Assessment) Program

December 7, 2000

1. Introduction

SPEC Incorporated was awarded a two-year contract on 5 June 1995 to:

- Design, build and install a new cloud microphysics instrument on the NASA DC-8.
- Collect data with the new instrument in the SUCCESS field experiment planned for the spring of 1996.
- Develop preliminary software and do quick-look processing of data collected by the new instrument.

On 16 May 1997, the original contract was modified to:

- Provide additional software to process data from the new instrument.
- Analyze SUCCESS data and publish results.

Additional milestones were added to the modified contract as shown below:

1) Completion of ice crystal classification of location, concentration, size, shape, ice water content and location in cirrus and contrails for SUCCESS flights on 4/20/96 and 5/12/96.

2) Completion of ice crystal classification of location, concentration, size, shape, ice water content and location in cirrus and contrails for SUCCESS flights on 4/30/96, 5/2/96 and 5/8/96.

3) Completion of manuscript for submission to Journal of Geophysical Research on the formation of ice crystals and how they are distributed in contrails.

4) Compilation of data base of scattering phase functions and ice crystal habits from the Colorado State University cloud chamber.

5) Completion of correlation of individual ice crystal habits scattering phase functions from SUCCESS flights on 4/20/96 and 5/12/96.

6) Completion of correlation of individual ice crystal habits and scattering phase functions from SUCCESS flights on 4/30/96, 5/2/96 and 5/8/96.

7) Completion of review of current parameterizations of radiative transfer from cirrus and contrails used in GCMs and development of new candidate parameterizations based on analysis of scattering phase function and crystal habit from cloud chamber and SUCCESS data.

8) Completion of numerical simulations and evaluation of candidate parameterizations to be used in GCMs.

Milestones ***1) – 6)*** were completed and results can be found in 32 monthly reports and an interim report submitted on 21 July 1997. The completion of Milestones ***7) & 8)*** was delayed slightly and the results are included in this final report. In addition, the final report contains a brief summary of work completed since 1995, a list of publications resulting directly from this research and also papers and conference proceedings that are an extension of this research. Finally, Appendix A contains reprints of three journal articles, two of which are from the SUCCESS special issue of *Geophysical Research Letters*, and a third that is from the NASA FIRE III special issue of the *Journal of Geophysical Research*. The *JGR* paper is a report of microphysical properties of Arctic stratus and cirrus clouds, based largely on analysis of data collected by the SPEC cloud particle imager (CPI), an outgrowth of the particle imager developed

for the SUCCESS project. Also, we anticipate submitting the results from investigations of Milestones ***7) & 8)*** for publication in a scientific journal.

2. Summary of Results (Milestones 1 – 6)

The new instrument developed for the SUCCESS project was called a Π-Nephelometer, because it simultaneously performed particle imaging (i.e., Pi or the Greek letter Π) and measured the light scattered around the imaged particle.

The initial SPEC proposal which generated the original (two-year) contract contained a time frame where the instrument would be developed in the first year and flight tested in the second year. However, the SUCCESS field project was subsequently scheduled to take place ten months after the contract was signed. Both NASA and SPEC scientists acknowledged the desirability of having the Π-Nephelometer available for the field project, so it was agreed that SPEC would attempt to accelerate the development of the new instrument. It was understood at the time that the development effort would be streamlined, and that there were risks involved, with the possibility that the Π-Nephelometer would not be available in time for SUCCESS. There were substantial challenges facing both NASA and SPEC engineers, including:

1. The probe and digital data acquisition system were unique. There was no existing instrument which produced digital particle images with 5 μm resolution, simultaneously measured the scattering phase function and recorded all of the data on a high-rate digital data acquisition system.

2. The probe could not be installed in a standard PMS canister and required a special mount at the zenith-1 location on the DC-8. NASA and SPEC engineers designed a special mount which was fabricated by NASA. Also, SPEC had no previous experience with the installation of sensors or instrument racks on the DC-8, so new ground needed to be broken in this area.

The overall effort to build and install the Π-Nephelometer on the DC-8 and to operate it during the field project was successful (**Figure 1**). However, the instrument and data system were literally completed within a few days of the last day the DC-8 was available for installing equipment. As a result there were aspects of the instrumentation which did not function perfectly. This was expected due to the highly accelerated schedule under which the instrument was designed and built.

The optical imaging system, which was new and previously untried, performed exceptionally well and high-resolution (5 μm) digital images of ice crystals were recorded. The digital data system was designed to operate at a

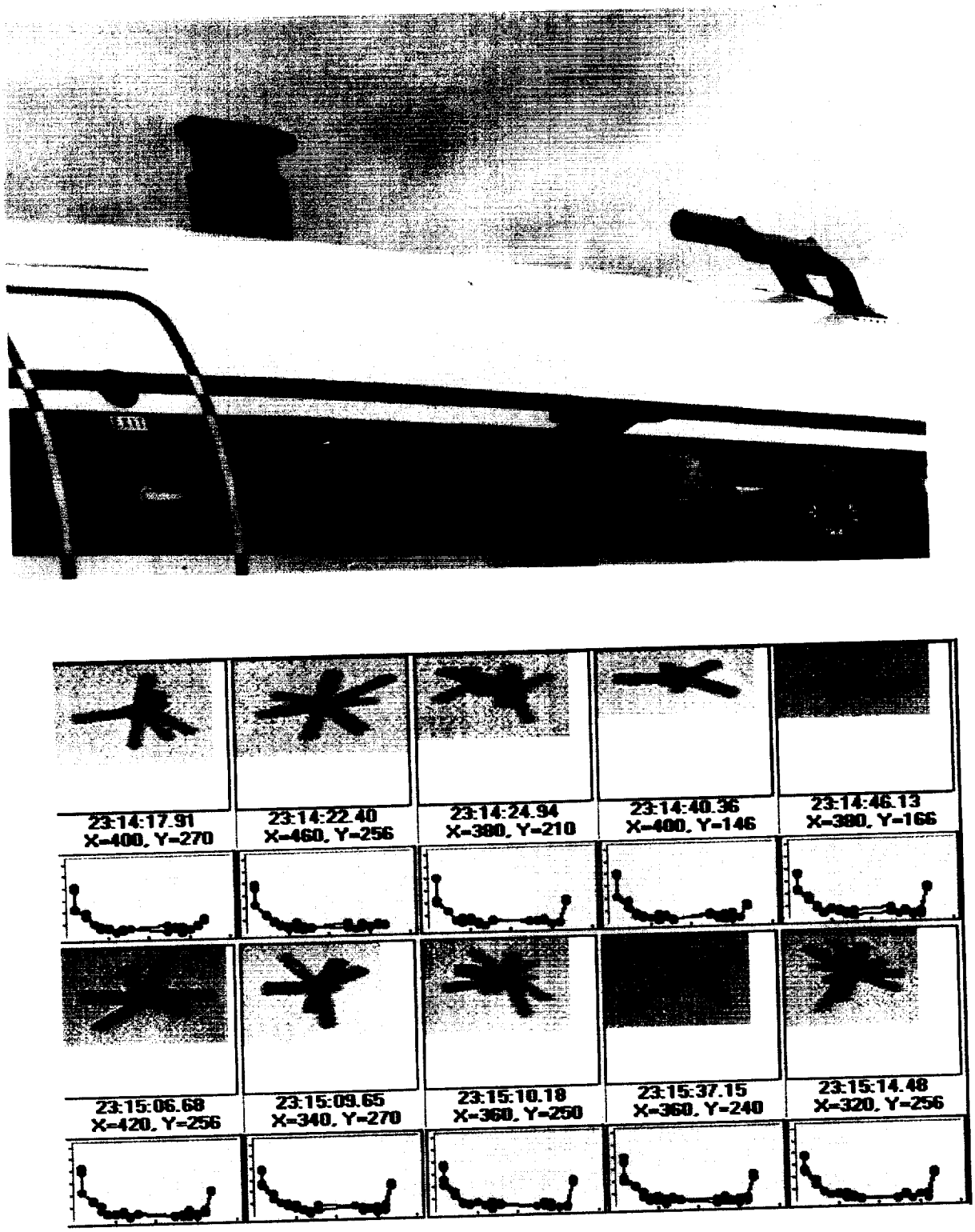

Figure 1. (top) The Π-Nephelometer installed on the NASA DC-8 and (bottom) examples of rosettes imaged during the SUCCESS field project, April-May of 1996.

maximum (asynchronous) rate of 25 frames s^{-1}, however, due to a bug in a software driver, the maximum obtainable rate was 5 frames s^{-1}. Thus, while image quality was excellent, the quantity of image data was less than anticipated. However, even though the software bug limited the rate of image data, the instrument still counted all particles larger than about 20 μm while the imaging system was inactive. Thus, it was possible to statistically enhance derived quantities such as particle concentration and ice water content. Analysis of SUCCESS microphysical data collected in contrails and scattering phase functions for particles typically observed in contrails are reported in Heymsfield et al. (1998) and Lawson et al. (1998). Reprints of these articles are found in Appendix A.

The particle imaging system and the digital data acquisition system were substantially improved after SUCCESS as a result of parallel funding provided by the National Science Foundation (NSF). The improvements were made to an instrument built for NSF, called the cloud particle imager (CPI). The CPI was installed on the NCAR C-130 for the FIRE III arctic field program conducted May - July 1998. Results from the FIRE III field project are reported in Lawson et al. (2000), which is included in Appendix A.

3. Results from Milestones 7 and 8.

3.1 Introduction

The impact cirrus clouds and aircraft contrails have on earth's radiation balance is poorly understood. Cirrus clouds regularly cover 20% to 30% of the earth (Warren et al. 1986). Contrails can grow into cirrus clouds, and can expand to cover the entire sky if conditions are favorable. Radiative modeling has shown that the radiative properties of cirrus cloud particles are extremely important (Fu 1996). Detailed measurements of crystal size, shape, and radiative properties are necessary to better understand the impact of cirrus clouds and contrails (Stephens 1989).

Model simulations by Fu (1996) showed that optically thin cirrus clouds with high concentrations of small particles (less than 10 microns) can have a cooling effect at the surface. This is because, visible light energy is reflected while infrared energy upwelling from the surface passes through the cloud, since small ice crystals act as Rayleigh scatterers for longwave radiation (Wallace and Hobbs 1977). This results in a net out-flow of energy. Understanding the radiative properties of cirrus particles would improve understanding of the radiative impact of cirrus clouds and contrails.

SPEC designed and fabricated a new instrument, called a Particle Imaging Π-Nephelometer, and operated it on the NASA DC-8 during the

Subsonic Aircraft: Contrail and Cloud Effects Special Study (SUCCESS) project. The Π-Nephelometer imaged cloud particles and made measurements of the scattering phase function. Due to instrument problems, the Π-Nephelometer was unable to take scattering phase function measurements during the field project. The scattered light measurement system in the Π-Nephelometer was repaired and the instrument was later taken to the Colorado State University (CSU) cloud chamber. Ice particles similar to those previously imaged in cirrus and contrails during the SUCCESS project were generated and scattering phase function measurements were collected (Lawson et al. 1998).

In Section 3.2 of this report, the scattering phase function measurements collected in the CSU cloud chamber are described and analyzed. A review of common atmospheric model parameterizations is made and new parameterizations based on the Π-Nephelometer data are developed and compared. It was found that discrepancies between parameterizaters calculated from the Π-Nephelometer data and commonly used parameterizations were greatest for small particles. A cirrus cloud model with the newly created Π-Nephelometer parameterizations is run in Section 3.3 of this report. Results from parameterizations commonly used in the literature are compared to model runs using parameterizations based on Π-Nephelometer measurements.

3.2 Development of New Parameterization (Milestone 7)

3.2.1 Review of Parameterizations found in the Literature

Climate and weather prediction models define clouds with parameterizations based on the cloud's properties. The following is a list of parameters commonly used in models and how they are related to the Π-Nephelometer measurements.

- Optical Depth: Optical depth is simply the measure of the cloud's optical thickness. The Π-Nephelometer was not designed to make gross cloud optical depth measurements. A microphysical optical depth can be calculated if one knows the concentration and projected area of the cloud particles. The Π-Nephelometer measures projected area exceptionally well and is therefore useful in calculating a microphysical optical depth.

- Single Scattering Albedo: The single scattering albedo is the ratio of scattered light vs. total extinction. The laser used by the Scattered Light System (SLS) has a visible wavelength and therefore, very little absorption. The single scattering albedo is therefore very close to 1.0.

- Asymmetry Parameter: The asymmetry parameter is a measurement of how much light is scattered by a particle in the forward direction versus the backward direction. The asymmetry parameter is calculated from the scattering phase function $P(\theta)$ which was measured by the Π-Nephelometer.

Optical Depth

Microphysical optical depth is shown in eq 1.

$$\tau = A_E * N \qquad \text{Eq. 1}$$

τ is the optical depth, A_E is the extinction per particle (in the visible, A_E is twice the projected area of the particle) and N is the number of particles in the column. The more conventional definition of optical depth, based on Beers Law, is defined as:

$$\tau = -\ln\left(\frac{I}{I_0}\right) \qquad \text{Eq. 2}$$

where I is the observed radiative intensity and I_0 is the incident intensity. Equation 2 is a bulk optical depth measurement. These definitions converge at small optical depths (less than 0.5) where multiple scattering is less important.

Asymmetry parameter

Numerous experimental and theoretical studies have been carried out to determine the value of the asymmetry parameter, g, for ice clouds. **Table 1** shows a summary of some of the research efforts as well as results from this work. For ice crystals, ray tracing models have been run using basic particle shapes (e.g., Takano and Liou 1995). More recently, complex crystals such as aggregates and planar polycrystals, as well as ice crystals with inclusions, have also been studied (e.g., Mischenko and Macke 1999).

The literature contains few experimental measurements of g. Aircraft and satellite measurements have yielded values of 0.7 to 0.8 (Gerber et al. 2000). Laboratory measurements have indicated values of g from 0.82 to 0.85 (from data in Volkovitsky et al. 1979 and Sassen and Liou 1979). Francis (1995) noted that these measured values agree well with simulations, but also noted that errors in measuring the forward scattering peak could cause considerable uncertainties when calculating g from measured phase functions.

Ray Tracing results from Takano and Liou 1995		
Particle Shape	Asymmetry Parameter	Particle Maximum Dimension
Bullet Rosettes	0.786 and 0.831	120 and 240 μm
Equal projected area solid columns	0.814 and 0.834	200 μm
Hollow Columns	0.843 to 0.858	L = 300 μm hollow 0-75 μm
Dendrites	0.820 to 0.842	10 and 40 μm
Solid Plates	0.814	40 μm
Capped Column	0.865	250 μm
Ray Tracing results from Macke et al. 1993		
Koch-fractal	0.740	1000 μm
Macke and Mishchenko 1999		
Crystal with inclusions	As low as 0.550	
Parameterizations		
Plates (Mitchell et al. 1996)	0.85 to 0.95	30 to 2000 μm
Columns (Mitchell et al. 1996)	0.75 to 0.87	30 to 3000 μm
Generalized (Fu 1996)	0.76 to 0.83	20 to 200 μm
Aircraft and Satellite measurements		
CIN Probe Gerber et al. (2000)	0.737	Glaciated cloud
Satellite Wielicki et al. 1990	0.70	Landsat Re = 60 μm
Laboratory measurements/calculations		
Volkovitsky et al (1979)	0.85	
Sassen and Liou (1979)	0.82	

Particle Maximum size (μm)	**Column**	**Irregular**	**Rosette**	**Spheroid**	**Fu**	**Mitchell** for columns	**Mie**
20	0.822	0.834		0.847	0.772	0.736	0.867
40	0.814	0.813	0.800	0.822	0.778	0.759	0.870
60	0.810	0.813	0.808		0.789	0.773	0.877
80	0.810	0.812	0.812		0.800	0.783	0.879
100	0.825		0.821		0.801	0.790	0.879
120	0.824		0.822		0.809	0.797	0.880
140			0.829		0.816	0.802	0.881
160			0.837		0.823	0.807	0.882
180			0.830		0.828	0.811	0.884

Table 1. Compilation of some measured and theoretical values for the asymmetry parameter.

3.2.2 Instrumentation

The Π-Nephelometer's scattered light system (SLS) consists of an array of fourteen detectors at different angles around the scattering plane. The measurement angles are: 20, 28, 37, 45, 53, 61, 70, 110, 118, 127, 135, 143, 152, 160. A forward scattering detector catches light scattered from approximately 2.8 degrees to 9.8 degrees. The SLS laser and optics produced a (nominaly 100:1) polarized beam with a rectangular cross-section. The forward scattering detector was a circular detector with a rectangular dump spot to block the SLS laser.

The SLS was calibrated using measured water drops and Mie theory. The forward scattering detector was calibrated for the value of the Mie curve at 11 degrees. Light scattered off the surface or through the surface of a water drop can be highly polarized depending on the angle of incident or refraction. If polarized light is incident onto a water drop it may show much less scattered light at certain angles depending on the polarization orientation. The Π-Nephelometer SLS laser was polarized at an angle that could make this effect significant, however, the angles where this would cause the most error in the phase function (60 to 150 degrees) measurement have very little contribution (<2%) to the asymmetry parameter calculation. **Figure 2** shows a plot of the Mie theory curve along with the SLS measurement for 20 micron water drops.

3.2.3 Calculating Asymmetry Parameter from Π-Nephelometer Data

First, values were log-linearly interpolated between measured points. For the two unmeasured end regions (0 to 11 and 160 to 180 degrees) Mie theory phase functions calculated for 20 micron spheres was substituted. A multiplication factor was applied to the end segments so that the values lined up with the last measured values. Errors introduced by this are discussed below.

The definition of asymmetry parameter is given below.

$$g = \int_0^{\pi} P(\theta)\cos\theta\sin\theta d\theta \qquad \text{Eq. 3a}$$

Where g is the asymmetry parameter, $P(\theta)$ is the phase function and θ is the scattering angle. For our data with 1 degree increments equation 3a reduces to equation 3b.

$$g = \sum_0^{180} P(\theta)\cos\theta\sin\theta \qquad \text{Eq. 3b}$$

Before applying eq 3b the phase function needs to be normalized according to equation 4:

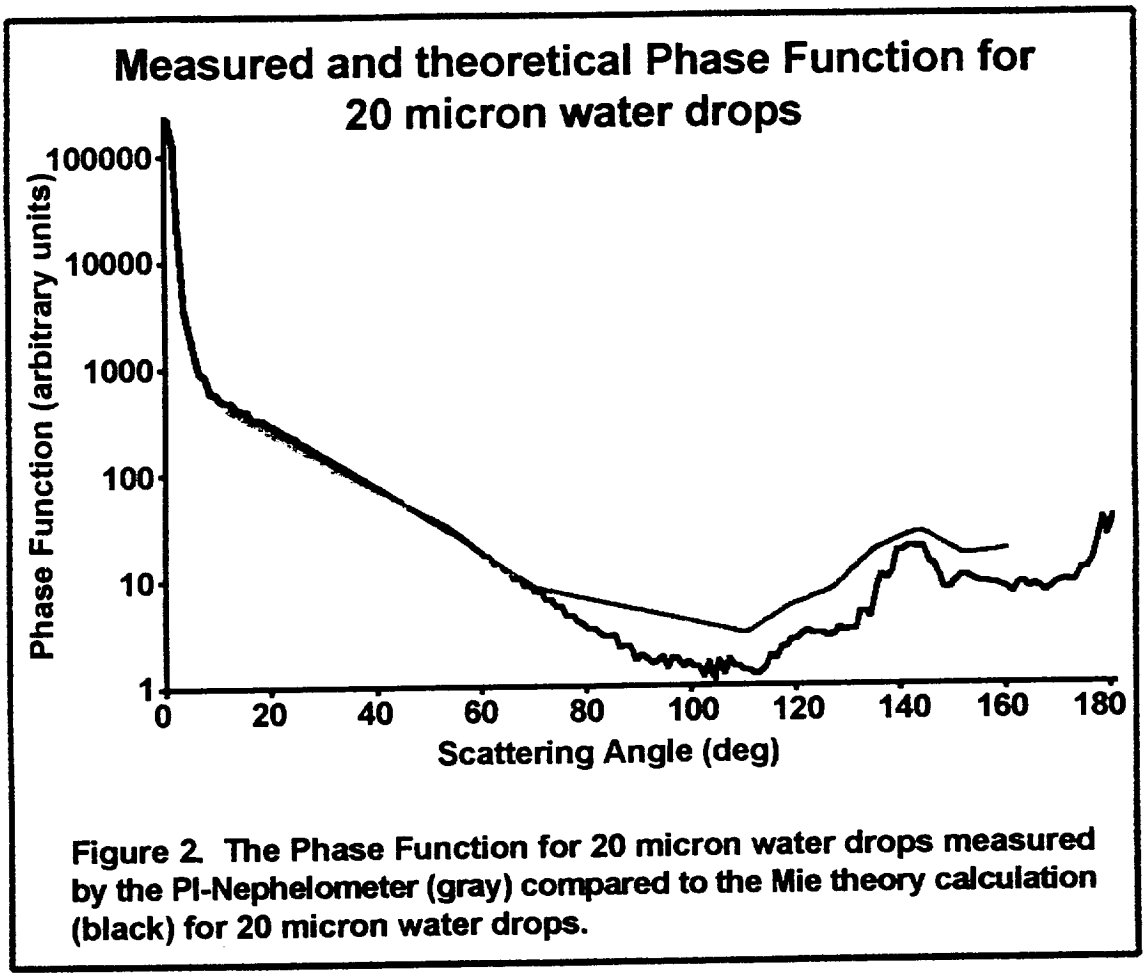

Figure 2. The Phase Function for 20 micron water drops measured by the PI-Nephelometer (gray) compared to the Mie theory calculation (black) for 20 micron water drops.

$$\sum_{0}^{180} P(\theta)\sin\theta = 1 \qquad \text{Eq. 4}$$

After normalization the phase function is multiplied by sin(θ)cos(θ) and then summed to give the asymmetry parameter (Eq. 3b).

Typical theoretical values of asymmetry parameter range from 0.5 to 0.9 depending on size and shape of particle. A value of 1.0 would indicate all forward scattering, while a value of –1.0 would be all back-scattering (Mitchell et al. 1996). The asymmetry parameter is highly dependant on the forward scattering peak. **Figure 3** shows a graph of the significance as a function of angle for the phase function for a 20 micron water drop. The significance simply shows the contribution to the asymmetry parameter from each angular measurement as a percentage of total scattered light.

Mishchenko (personal communication) suggested calculating the asymmetry parameter in two parts, the measured phase function part and the diffraction part similar to the process described in Mishchenko and Macke (1998). The measured phase function calculation can be treated as the Geometric Optics phase function after any diffraction peak is truncated. The diffraction component of the asymmetry parameter is the light diffracted by the particle in the forward direction. The diffraction asymmetry parameter is always very close to 1.0 in the visible. The measured phase function component of the asymmetry parameter is the asymmetry parameter calculated as above except the diffraction peak is removed from the phase function. For particles with a size parameter (size parameter = $2\pi a/\lambda$ where a is radius and λ is wavelength) greater than 50 or so, half of the scattered light is from diffraction. The smallest particles in this study had a size parameter near 60. Therefore the asymmetry parameter is:

$$g = \frac{g_d + g_{meas.}}{2} \qquad \text{Eq. 5}$$

Where g_d is the diffraction part of the asymmetry parameter and g_{meas} is the asymmetry parameter calculated from the measured phase function (used as the geometric optics phase function in Mishchenko and Macke 1998).

For the Π-Nephelometer data the diffraction peak (that came with the Mie Theory curve) was truncated at 2.5 degrees. Angles smaller than 2.5 degrees were given the same value as the 2.5 degree value. Errors introduced by this are discussed below.

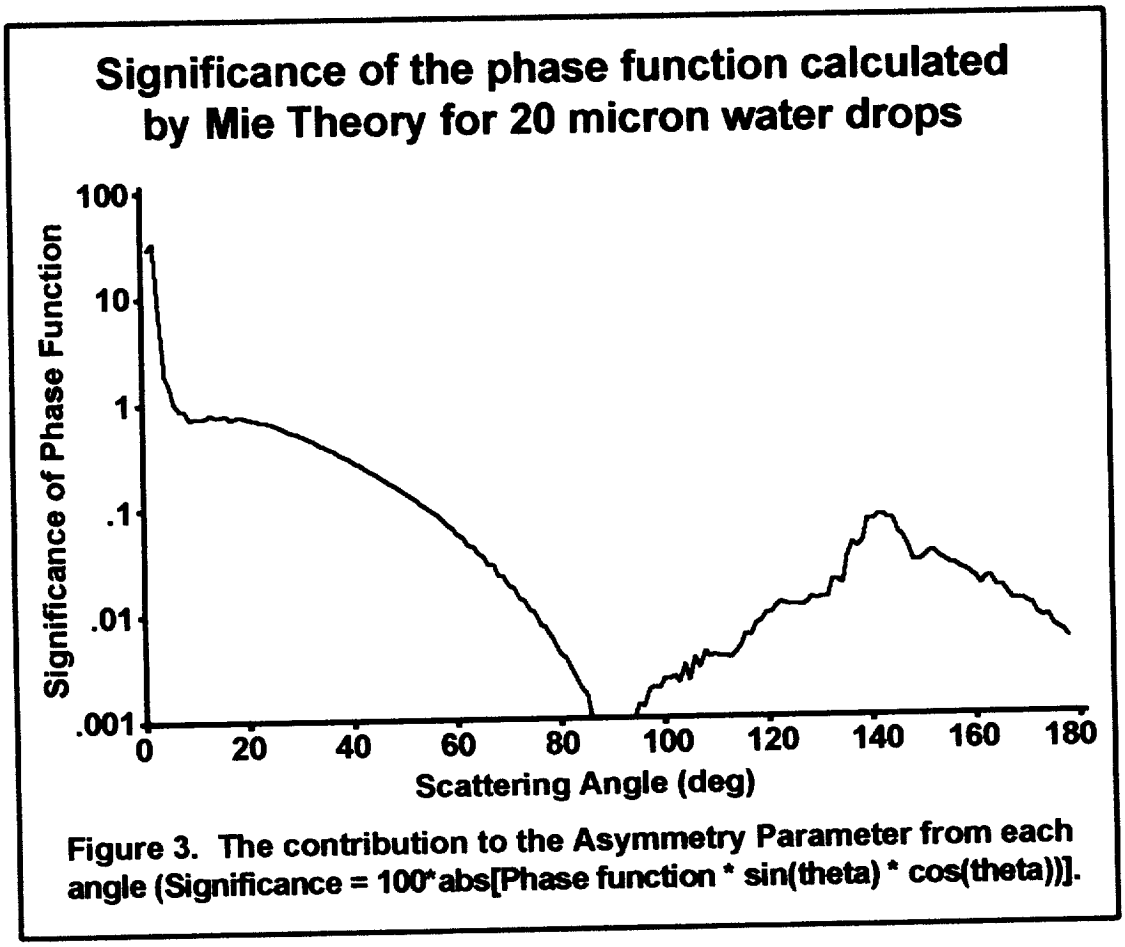

Figure 3. The contribution to the Asymmetry Parameter from each angle (Significance = 100*abs[Phase function * sin(theta) * cos(theta))].

3.2.4 Asymmetry Parameter Results and Comparison to Values Found in the Literature

Figure 4 shows the asymmetry parameters calculated from the Π-Nephelometer data. Asymmetry parameter parameterizations calculated from Fu (1996), Mitchell et al. (1996) as well as Mie theory are compared to the Π-Nephelometer calculations on **Figure 4**. The bottom of **Table 1** shows the data used to make **Figure 4**.

An interesting observation is that the smallest particles always have asymmetry parameters much larger than the parameterizations. The smallest particles observed by the Π-Nephelometer (as well as small particles observed in cirrus) were generally spheroidal in appearance. Fu's parameterization is based on ray tracing for hexagonal ice crystals. The scattering properties of ice spheres and pristine hexagonal plates or columns are quite different (compare the Fu and Mitchell parameterizations with Mie theory on fig. 3). The Π-Nephelometer data shows that small spheroidal ice particles have asymmetry parameters closer to those calculated by Mie theory than to the hexagonal particle parameterizations. **Figure 5** shows a typical example of particles observed in cirrus. The particular cloud particles were observed over Oklahoma by the CPI (the probe developed after the Π-Nephelometer). Particle habit classification by concentration as well as radiatively important projected area are also shown on **Figure 5**. The small particles are mostly spheroidal in appearance. Concentration estimates have shown that cirrus can be made up of 90% or more particles like these. Contrails observed by the DRI cloudscope have been shown to be composed of numerous small pristine hexagonal crystals. The Fu and Mitchell parameterizations for smaller particles may be more appropriate for contrails than for cirrus.

Possible errors

The introduction of errors by using Mie theory for 20 micron water drops to fill in the missing end segments of the measured phase functions were thoroughly investigated. Indeed, it seems ludicrous to use theoretical data for 20 micron spheres to patch in holes for data collected looking at up to 200 micron rosettes. To test the reasonableness of this technique, Mie theory for 50 micron drops (similar projected area to 150 micron bullet rosettes) was substituted where Mie theory for 20 micron drops had been used previously. The error was less than 1% when the asymmetry parameter was calculated using eq 5. This result becomes obvious when one notices that the main difference between Mie theory phase functions between zero and 11 degrees is the height and width of the diffraction peak. **Figure 6** shows the diffraction peak for the different Mie theory curves. The diffraction peak for the 50 micron drops

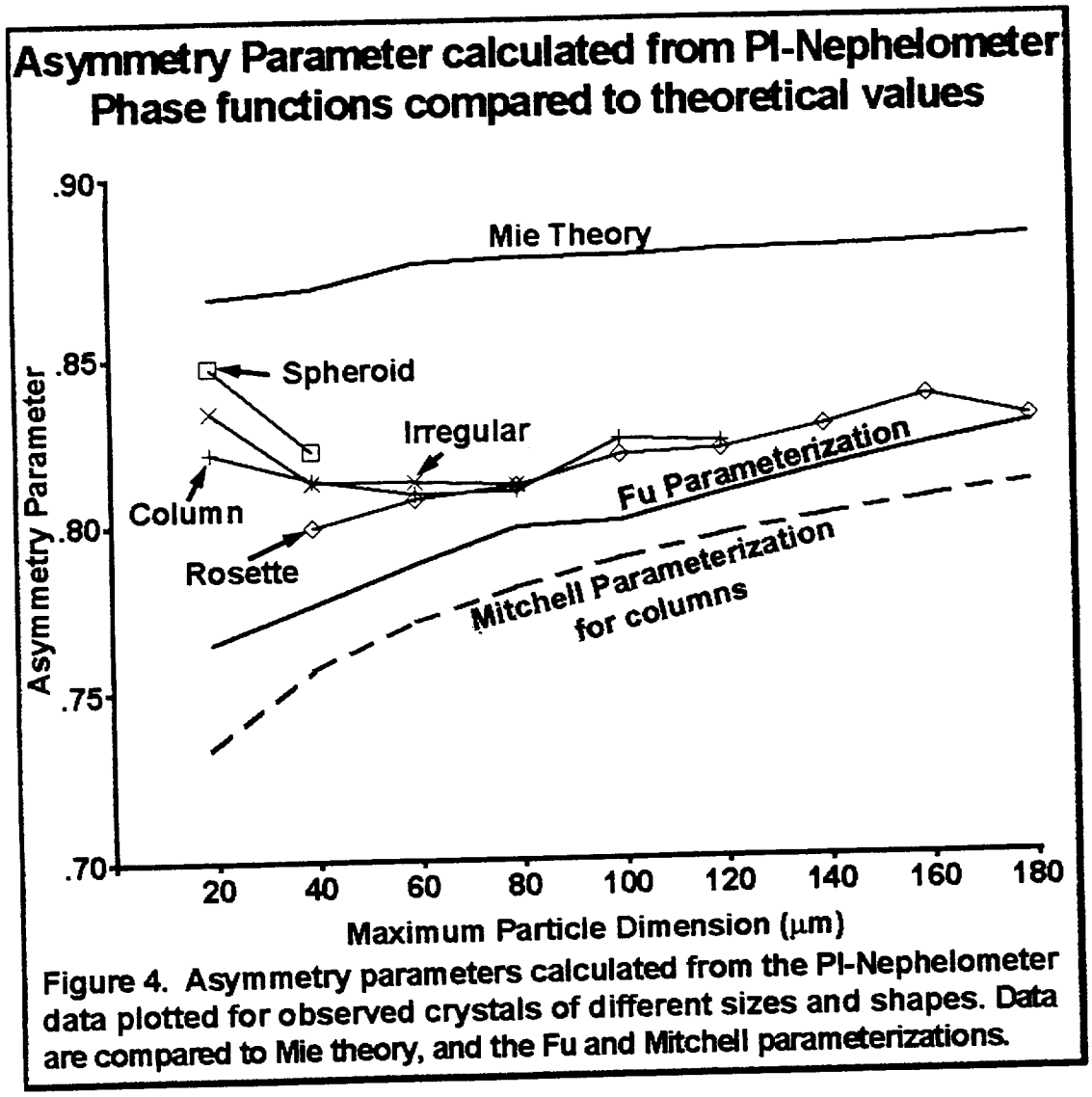

Figure 4. Asymmetry parameters calculated from the PI-Nephelometer data plotted for observed crystals of different sizes and shapes. Data are compared to Mie theory, and the Fu and Mitchell parameterizations.

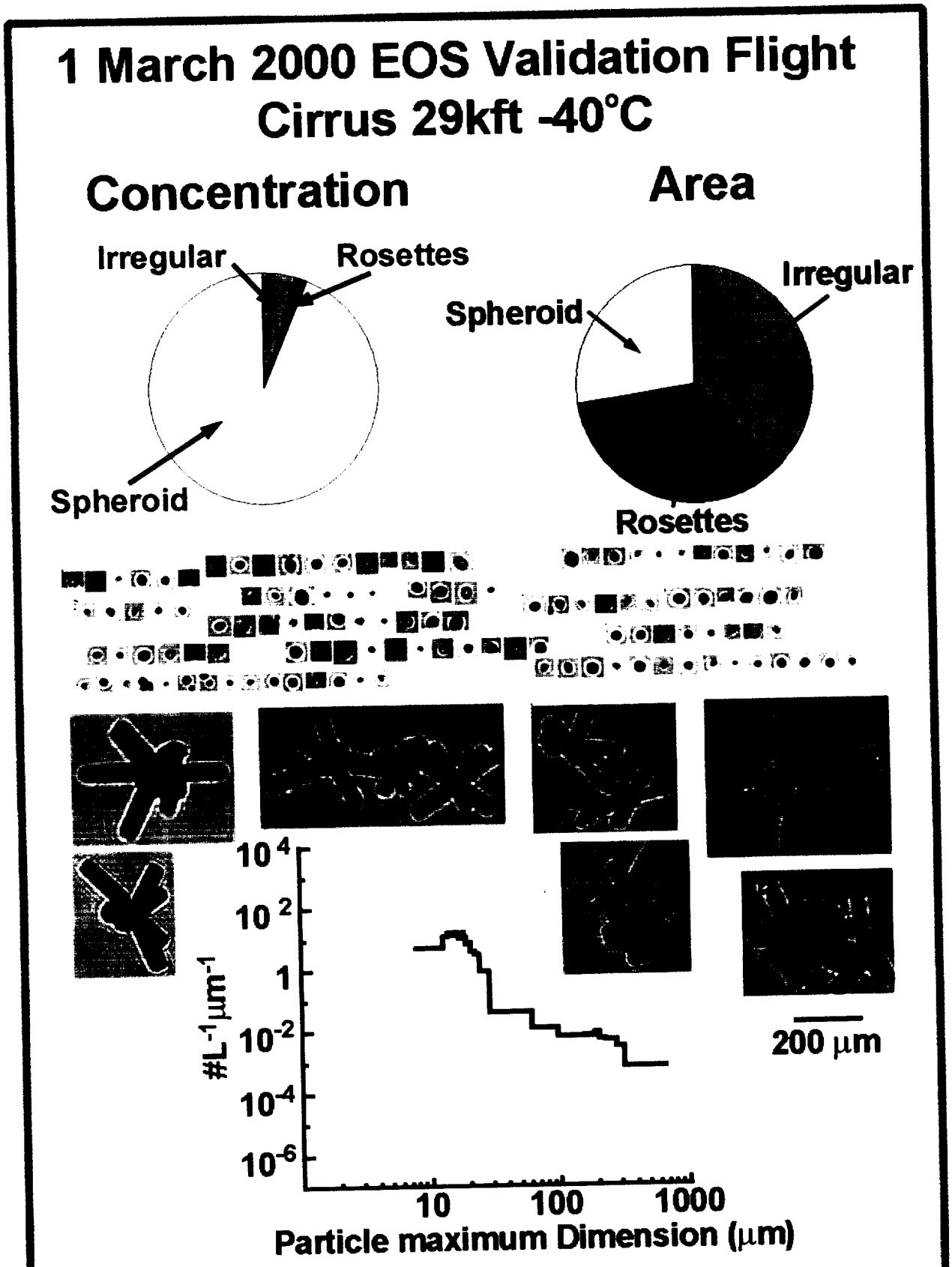

Figure 5. Particle Habit Classification (based on concentration and area) example images of crystals and CPI Particle Size Distribution for Mid-Latitude Cirrus cloud.

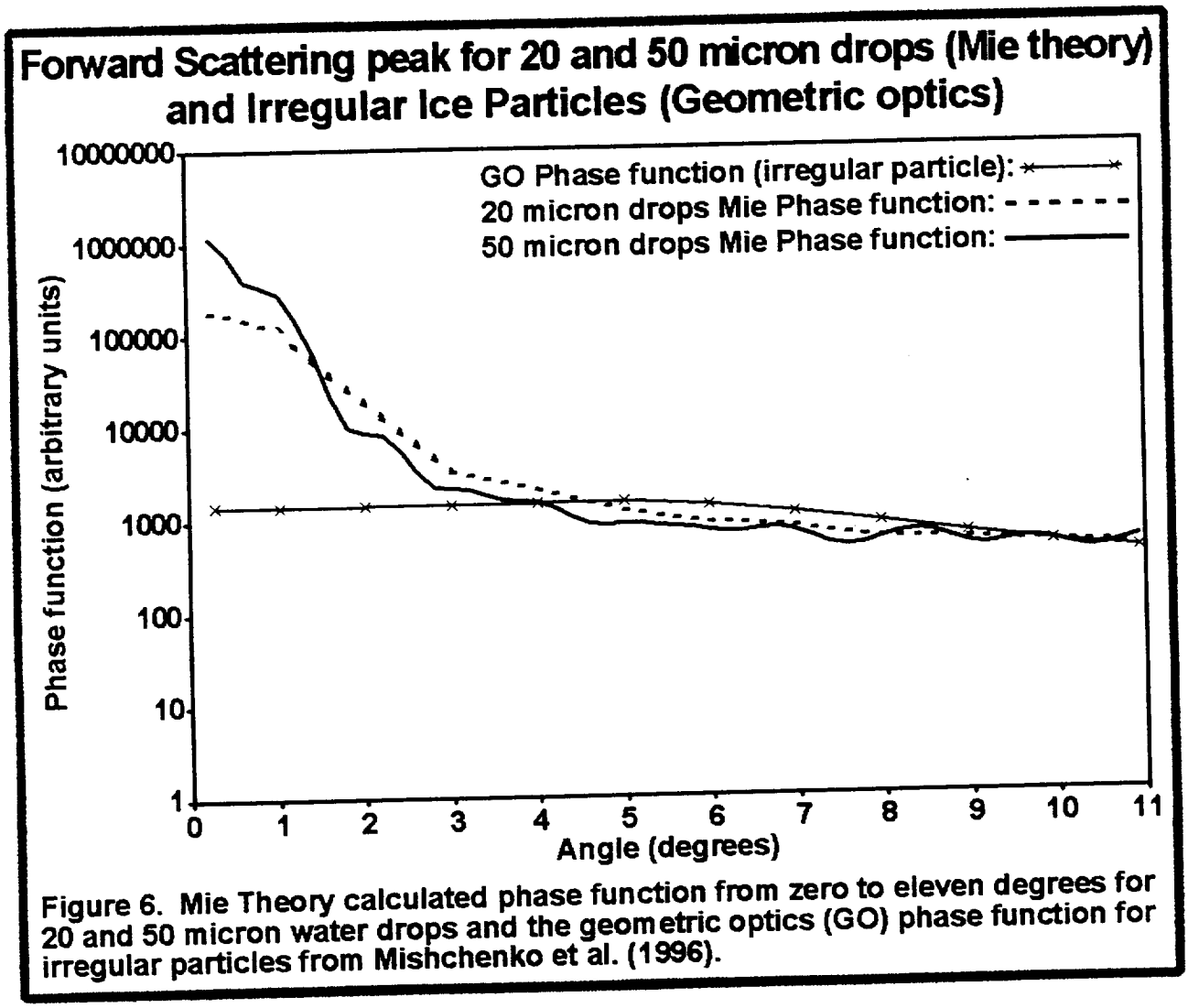

Figure 6. Mie Theory calculated phase function from zero to eleven degrees for 20 and 50 micron water drops and the geometric optics (GO) phase function for irregular particles from Mishchenko et al. (1996).

is much higher at angles less than 1.5 degrees than curve for 20 micron drops. The use of the phase function from Mie theory for 20 micron spheres in the backscattering region caused almost no change in the calculated asymmetry parameter compared to using zeros or interpolating to four times the 160 value at 180.

The degree of truncation of the diffraction peak is a possible source of error. To test the magnitude of possible errors the diffraction peak was cut off at several different angles from 2.5 degrees to 9.5 degrees. This had little effect on the asymmetry parameter (less than 2%). One would expect this to be the case from looking at the diffraction peak in **Figure 6**. The Geometric Optics asymmetry parameter for an irregular ice particle (from Mishchenko et al. 1996) scaled to the other curves is also shown in **Figure 6**. This confirms that the truncation procedure does not cut off any of the Geometric Optics scattered light. The Mie theory phase functions slopes are relatively flat in the 2.5 to 11 degree region similar to the Geometric Optics phase function.

3.2.5 Summary and Conclusions (Milestone 7)

The Π-Nephelometer cloud probe design by SPEC Inc gathered scattering phase function data during laboratory measurements in the CSU cloud chamber. These phase functions have been used to calculate the asymmetry parameter. A technique was adapted that allows an accurate calculation of the asymmetry parameter even when complete information about the forward scattering peak is unknown. Results of this technique applied to the Π-Nephelometer data show little variation (less than 3%) when the technique is purposely applied erroneously.

The asymmetry parameters calculated from the Π-Nephelometer data agree reasonably with other laboratory measurements and theoretical calculations for larger particle sizes (> 50 μm). For smaller particle sizes the asymmetry parameter values were generally higher than current parameterizations. This could be due to the fact that the small particles observed were spheroidal rather than the pristine hexagonal shapes which ray tracing models are based on. Small particles observed in cirrus clouds are generally spheroidal in appearance.

For accurate calculation of the asymmetry parameter from data with poor forward scattering measurements, the asymmetry parameter should be calculated in two parts. The diffraction part of the asymmetry parameter is always 1.0 in the visible when the size parameter is large. The remaining part of the asymmetry parameter is calculated from the phase function with any diffraction peak truncated. If large areas of the forward peak are not known, a suitable theoretical phase function can be substituted without introducing much error (as long as any diffraction-like peak is truncated). The bulk of the error in

calculating the asymmetry parameter from phase functions is from the height and width of the diffraction peak. When the size parameter is greater than 20, the extinction efficiency tends towards 2.0. 50% is forward diffraction and 50% is either scattered or absorbed. In visible wavelengths where absorption is very low, half of the asymmetry parameter is from diffraction and half is from the scattering phase function.

3.3 Numerical Simulations (Milestone 8)

3.3.1 The model

The cirrus model used for this study is a Monte Carlo model. The model was developed by D. Koracin, V. Isakov and L. Mendez-Nunez (Koracin et al. 1998). The input parameters for the model include asymmetry parameter, single scattering albedo and optical depth for fifteen cloud layers. In addition sun angle and surface albedo are also input parameters. The outputs are simply radiation flux in the upwards and downwards direction at each level.

Model Computational Scheme

Optical properties of the model clouds are characterized by layer optical thickness τ, single scattering albedo ω, and asymmetry parameter g. The optical properties of the surface are determined by an albedo A (generally assumed to be 18 %).

For the purpose of this project the model was run with horizontally homogeneous cloud layers. For simplicity the photons enter the atmosphere vertically. When a photon enters the model atmosphere several processes are possible. It can be scattered, absorbed, or it can be reflected from the surface.

The photon free-path-length is determined by the optical thickness τ:

$$\tau = \int_0^L (\kappa(l) + \sigma(l))dl$$

where $\kappa(l)$ is an absorption coefficient, $\sigma(l)$ is the scattering coefficient, and L is the photon trajectory.

The probability of a photon passing through the atmosphere without scattering or absorption is $\exp(-\tau)$. Scattering is considered as a random process with a probability $\omega=\sigma/(\kappa+\sigma)$. The scattering angle is determined by

the asymmetry parameter which is used to calculate a probability density of scattering angles.

In order to calculate diffuse radiation fluxes, the Monte Carlo method is used by the model. Photons are traced from the top of the model atmosphere. Each grid point of the domain has a counter which is incremented if a photon passes its grid level in either the upward or downward direction. Large numbers of photons (10,000 to 100,000) are necessary to achieve sufficient accuracy.

The model uses the cumulative optical depth as a vertical coordinate:

$$\tau^*_{i,k} = \tau^*_{i-1,k} + \tau_{i,k} \quad \text{For } i = 2, n+1$$

$$\tau^*_{1,k} = 0$$

$$\tau^*_{n+1,k} = \tau_{0,k}$$

where i and k represent the vertical and horizontal coordinate in the model space.

For the first trajectory, the counters for all layers are set to zero and the photon free path length is determined by:

$$\alpha = e^{-\tau}$$

$$\tau = \tau - \ln(\alpha)$$

where α is a random number. Basically, a random number determines how much optical depth the photon will pass through before interacting.

The chance of the photon getting to the surface, being scattered or absorbed is then considered. If the free path length enables the photon to reach the surface, reflection from the surface is also considered.

If the photon free path length is less than the total optical depth in the simulated cloud, a photon scattering event is considered at the cloud position:

$$\tau^*_{l,k} \leq \tau \langle \tau^*_{l+1,k}$$

Absorption was not considered for this project (the single scattering albedo was set to 1.0 which is reasonable for the visible). A random number determines the scattering angle of the photon based on the local asymmetry parameter. After a photon is scattered, a new photon free path length is determined using the random number generator. Once the photon reaches

the statistical noise level (as determined by *d* discussed earlier), it is no longer considered.

Counters are incremented based on how far the photon makes it:

$$F_{n+1}^{\uparrow} = A \cdot F_{n+1,k}^{\downarrow}$$

$$F_{i,k}^{total\downarrow} = F_{i,k}^{total\downarrow} + F_{i,k}^{\downarrow}$$

$$F_{i,k}^{total\uparrow} = F_{i,k}^{total\uparrow} + F_{i,k}^{\uparrow}$$

A new photon enters the system once the first is finished and the same process is repeated. Fluxes are calculated based on the numbers counted at each layer.

Emphasis for Modeling Runs

The main difference between the Π-Nephelometer calculated asymmetry and the common parameterizations (Mitchell et al. 1996 and Fu 1996) are at the small particle end. Figure 5 shows that typical cirrus contains high number of small spheroidal particles which make up a significant portion of cirrus cloud extinction (i.e. projected area). For small particles the parameterizations show low values of asymmetry parameter (0.73 to 0.77). The Π-Nephelometer data gave values for asymmetry parameter that were much higher for 20 micron spheroidal particles (0.85). The discrepancy between the parameterizations and our calculations decreased for larger particles. Since the radiatively important small particles showed the most discrepancy, the modeling effort was concentrated there.

3.3.2 Model Results

Vogelmann and Ackerman (1995) used observed surface radiation fluxes to relate to cirrus cloud properties. Cirrus clouds were modeled and the effect of small perturbations in the cloud properties was investigated. A similar technique is used here to analyze our model results.

For the first model runs, we fixed the surface flux and varied the cloud properties based on Part I results. A cloud with five layers of optical depth 0.5 was modeled. The asymmetry parameter for each of these layers was defined to be 0.75 to represent the currently parameterized asymmetry parameter for small cirrus particles. 0.75 is about what the Fu (1996) and Mitchell et al. (1996) parameterization schemes give for small particles commonly observed in cirrus. The model was run and the flux at the surface was determined. The asymmetry parameter was then changed to 0.85 which is the value calculated from the Π-Nephelometer data. A number of model runs were then completed with different optical depths in an effort to match the surface flux. A perturbation in the optical

depth of about 2 percent was necessary to obtain equal flux at the surface. A cloud with an asymmetry parameter of 0.75 produced the same surface flux as a cloud with an asymmetry parameter of 0.85 and a 2% different optical depth. **Table 2** shows the parameters input into the model to achieve equal surface flux.

Asymmetry Parameter	0.75	0.85
Optical Depth (5 layers)	0.50	0.4905
Surface Flux W/m^2	392	392

Table 2. Input parameters for model runs to achieve equal surface fluxes. Optical depth and asymmetry parameter were varied.

The second model test used assumptions based on observed cirrus particles and the particles used for asymmetry parameter parameterizations. Naturally occurring small cirrus particles are spheroidal in appearance (fig. 4) while the particles parameterized by Fu (1996) and Mitchell et al. (1996) were hexagonal. The microphysical optical depth can be calculated using the average projected area of the particles. Projected area for a sphere and for a hexagonal particle (equal to its surface area / 4 for a randomly oriented convex particle) were used to determine microphysical optical depths for equal Ice Water Content (IWC) clouds. The microphysical optical depth is theoretically equal to the cloud bulk optical depth when the optical depths are low. Model runs were made on low optical depth clouds for equal IWC clouds with appropriate asymmetry parameters and optical depths. **Table 3** shows the cloud particle properties input into the model and the resulting surface flux. A difference of 19 $Watts/m^2$ between the clouds was determined by the model.

Particle shape	Spheroid	Hex-Crystal
Optical Depth	0.05	0.0423
Surface Area μm^2	314	371
Volume (mass)μm^3	4188	4188
Asymmetry Parameter	0.85	0.75
Surface Flux W/m^{2*}	1069	1050

Table 3. Cloud parameters for second set of model runs and the resulting surface flux calculation. *The surface flux is based on the fraction of solar irradiance that falls between 0.25 and 1.41 μm (from Fu 1996).

3.3.3 Summary and Conclusions (Milestone 8)

Model results have shown that differences in the asymmetry parameter can cause significant differences in optical depth and surface flux. A cloud

model was run in an effort to find the difference in optical depth that could be caused by using an incorrect asymmetry parameter. A cloud with an asymmetry parameter of 0.75 was modeled, then the asymmetry parameter was changed to 0.85 and the optical depth was varied in an effort to match the surface radiation flux of the first model run. The optical depth had to be changed by 2% in order to get the same surface flux in the second model run. Equal surface fluxes can be measured by clouds with two percent differences in their optical depth depending on what asymmetry parameter is used.

A second modeling effort was done to try to compare identical ice water content clouds. The cloud particles were designed in an effort to try to match observed clouds (spheroidal particles with asymmetry parameter 0.85) to those that were used for asymmetry parameter parameterization calculations (hexagonal particles with asymmetry parameter 0.75). A microphysical optical depth was calculated by estimating twice the projected area for a column number of particles. Optical depths were kept low in order to reduce the possibility of multiple scattering. A model run was done on each of the equal ice water content clouds. The surface flux difference was 19 W/m^2. This huge difference could mainly be accounted for by the different optical depths for the clouds. This result also shows that making cloud mass estimates from surface flux measurements is highly dependant on assumed particle microphysics. This 19 W/m^2 value should be thought of as an upper limit as it assumed perfect hexagonal crystals and perfect spheres as particle shapes.

References (for Sections 3.2 and 3.3)

Francis, P. N., 1995: Some aircraft observations of the scattering properties of ice crystals. *J. Atmos. Sci.*, **52,** 1142-1154.

Fu, Q., 1996: An Accurate Parameterization of the Solar Radiative Properties of Cirrus Clouds for Climate Models. *J. of Climate,* **9,** 2058-2082

Gerber, H., Y. Takano, T. J. Garrett, and P. V. Hobbs, 2000: Nephelometer Measurements of the Asymmetry Parameter, Volume Extinction Coefficient, and Backscatter Ratio in Arctic Clouds. *J. Atmos. Sci.*, **57,** 3021-3034.

Heymsfield, A. J., R. P. Lawson and G. Sachse, 1998: Growth of ice crystals in a precipitating contrail. *Geophys. Res. Ltrs.*, **25 (9),** 1335-1338.

Koracin, D., V. Isakov, L. Mendez-Nunez, 1998: A cloud-resolving model with the radiation scheme based on the Monte Carlo method. *J. Atmos. Res.*, **47-48**, 437-459.

Lawson, R. P., A. J. Heymsfield, S. M. Aulenbach and T. L. Jensen, 1998: Shapes, sizes and light scattering properties of ice crystals in cirrus and a persistent contrail during SUCCESS. *Geo. Res. Let.*, **25**, No. 9, 1331-1334.

Lawson, R.P., B.A. Baker and C.G. Schmitt, 2000: An overview of microphysical properties of Arctic clouds observed in May and July during FIRE.ACE. Accepted for publication in *J. Geophys. Res.* Special Issue on FIRE.ACE.

Mishchenko, M. I., W. B. Rossow, A. Macke, and A. A. Lacis, 1996: Sensitivity of cirrus cloud albedo, bidirectional reflectance, and optical thickness retrieval to ice-particle shape, *J. Geophys. Res.* **101,** 16,973-16,985

Mishchenko, M. I., and A. Macke, 1998: Incorporation of physical optics effects and computation of the Legendre expansion for ray-tracing phase functions involving δ-function transmission. *J. Geophys. Res.* **103,** 1799-1805.

Mishchenko, M. I., and A. Macke, 1999: Monte Carlo calculations of light scattering by large particles with multiple internal inclusions. Preprints, *Conf. On Light Scattering by Nonspherical Particles: Theory, Measurements, and applications,* New York, NY, Amer. Meteor. Soc., 143-146.

Mitchell, D. L., A. Macke, and Y. Liu, 1996: Modeling cirrus clouds. Part II: Treatment of radiative properties. *J. Atmos. Sci.,* **53,** 2968-2988.

Sassen, K., and K. N. Liou, 1979: Scattering of polarized laser light by water droplets, mixed-phase and ice crystal clouds. Part I: Angular scattering patterns. *J. Atmos. Sci.,* **36,** 838-851.

Stephens, G. L., 1989: Cirrus clouds and climate feedback: Is the sky falling and should we go tell the king? FIRE Science Meeting, Monterey, Calif. , 327-331.

Takano, Y. and K. N. Liou, 1995: Radiative Transfer in Cirrus Clouds. Part III: Light Scattering by Irregular Ice Crystals. *J. Atmos. Sci.,* **52,** 818-837.

Vogelmann, A. M., and T. P. Ackerman, 1995: Relating Cirrus Cloud Properties to Observed Fluxes: A Critical Assessment. *J. Atmos. Sci.,* **52,** 4285-4301.

Volkovitsky, O. A., L. N. Pavlova, and A. G. Petrushin, 1979: Scattering of light by ice crystals. *Atmos. Oceanic Phys.,* **16,** 90-102.

Wallace J. M., and P. V. Hobbs, 1977: *Atmospheric Science An Introductory Survey.* Academic Press, Inc. pp. 306-307.

Warren, S. G., C. J. Hahn, J. London, R. M. Chervin, and R. L. Jenne, 1986: Global distribution of total cloud cover and cloud type amounts over land. NCAR Technical Note NCAR/TN-273 + STR, (Available from NCAR, Box 3000, Boulder, CO 80307).

4. Publications Related to this Research

Baker, B.A., R.P. Lawson and C.G. Schmitt, 2000: Clumpy Cirrus. Proceedings: 13th International Conference on Clouds and Precipitation, Reno, NV, 14-18 August, Vol. I, 637-640.

Curry et al., including Lawson R.P., and T.L. Jensen, 2000: FIRE Arctic Clouds Experiment, *Bull. Amer. Meteor. Soc*, **81**, 1, 5-29.

Heymsfield, A. J., R. P. Lawson and G. Sachse, 1998: Growth of ice crystals in a precipitating contrail. *Geophys. Res. Ltrs.*, **25 (9)**, 1335-1338.

Jensen, T. L., and R. P. Lawson, 1999: Observations in various cloud systems over the SHEBA Ice Station during FIRE.ACE. Proceedings of the 5th Conference on Polar Meteorology and Oceanography, January 10-15, 1999. Dallas, TX. Paper P1.22.

Jensen, T.L., T.A. Uttal, J.M. Intrieri and R.P. Lawson, 1999: Comparisons of Depolarized Lidar and Cloud Radar with In-Situ Measurements in a Mixed Phase Cloud During FIRE.ACE. Proceedings of 5th Conference on Polar Meteorology and Oceanography, January 10-15, 1999. Dallas, TX. Paper 10.4.

Lawson, R. P., 1998: A Comparison of Ice Crystal Observations using a New Cloud Particle Imaging Probe in Arctic Cirrus and a Decaying Anvil in Texas. Presented at the Optical Society of America Cirrus Topical Meeting, 6-8 October, Baltimore, Maryland.

Lawson, R.P. and T.L. Jensen, 1998: Improved microphysical observations in mixed phase clouds. Proceedings: American Meteorological Society Conference on Cloud Physics, 17-22 August, Everett, Washington, 451-454.

Lawson, R. P., A.J. Heymsfield, S.M. Aulenbach and T.L. Jensen, 1998: Shapes, sizes and light scattering properties of ice crystals in cirrus and a persistent contrail during SUCCESS. *Geo. Res. Let.*, **25 (9)**, 1331-1334.

Lawson, R.P., B.A. Baker and C.G. Schmitt, 2000: An overview of microphysical properties of Arctic clouds observed in May and July during FIRE.ACE. Accepted for publication in *J. Geophys. Res.* Special Issue on FIRE.ACE.

Schmitt, C.G., R.P. Lawson and B.A. Baker, 2000: In Situ Measurements of Mid-Latitude and Tropical Cirrus Clouds. Proceedings: 13th International Conference on Clouds and Precipitation, Reno, NV, 14-18 August, Vol. II, 1209-1212.

APPENDIX A

Three Selected Reprints of Publications Relating to this Research

GEOPHYSICAL RESEARCH LETTERS, VOL. 25, NO. 9, PAGES 1335-1338, MAY 1, 1998

Growth of ice crystals in a precipitating contrail

Andrew J. Heymsfield[1], R. Paul Lawson[2], G. W. Sachse[3]

Abstract.
This study examines how jet aircraft contrails develop precipitation trails, using data collected on 12 May, 1996 during SUCCESS. The DC-8 sampled the pre-contrail conditions, produced a contrail largely in clear air at -52°C, and sampled the contrail and developing trails for over an hour. The environment was highly ice-supersaturated, reaching nearly water saturation in some locations. Inside the contrail core, almost all ice particles remained small ($\sim$ 1 to 10 μm) due to high crystal concentrations ($\sim 10^1$ to 10^2 cm^{-3}) which reduced the vapor density to saturation. Mixing of moist environmental air and vapor-depleted contrail air produced localized regions of supersaturation along the contrail periphery, where crystals grew to several hundred microns at about 0.1 μm s^{-1}. These particles could then fall from the contrail into the vapor-rich, undepleted, supersaturated environment below. As heavier crystals left the contrail, others moved into the regions of ice supersaturation. Precipitation trails developed as this process continued over time.

1. Introduction

Condensation trails or *contrails* are cloud-like streamers that frequently form behind aircraft flying in cold, clear, humid air. Critical environmental factors for contrail generation are the temperature, pressure, and water vapor density, *see* Schmidt (1941), Appleman (1953) or Khrgian and Mazin (1955). Persistent contrails occur when the ambient relative humidity with respect to water (RH) is at least at ice saturation (RH_i). Contrails occasionally produce precipitation trails.

There are few *in-situ* or remote measurements associated with the precipitation trails of contrails (Weickmann,1949; Knollenberg,1972; Konrad and Howard, 1974; Schumann, 1994). This paper examines the environmental factors that enable contrail particles to grow into larger precipitating particles, using data from 12 May 1996 when the NASA DC-8 research aircraft generated a contrail northwest of San Francisco, CA as part of the Subsonic aircraft: Contrail and Cloud Effects Special Study (SUCCESS) field program.

[1]National Center for Atmospheric Research, Boulder, Colorado

[2]SPEC Inc., Boulder, Colorado

[3]National Aeronautics and Space Administration, Hampton, Virginia

Paper number 98GL00189.
0994-8534/98/98GL-00189$05.00

2. Data Overview

The DC-8 made five sampling runs from $\sim$ 10.5 to 11.5 km (MSL pressure altitude), between 22:38 and 24:00 UTC. Figure 1 identifies these flight tracks as penetrations one through five (Pens. 1 - 5). A side effect of multiple sampling runs was the generation of additional contrails. Lidar data, along with the onboard observer notes, were used to differentiate ambient cirrus from the contrails, when possible.

Pen. 1 occurred at Z = 10.4 km and T = -47 °C, *see* Fig. 1A. The aircraft carried a diode laser hygrometer (DLH), *see* Vay et al. (1997), to measure the water vapor mixing ratio which was converted to RH (Fig. 1C) based on the air temperature. The RH at ice saturation, RH_i, was derived from T.

The DC-8's rear-facing video camera recorded contrail formation in the wake of the aircraft. A contrail was produced during Pen. 2, at 11.1 km where T = -52°C, *see* Fig. 1B, and RH >> RH_i, *see* Fig. 1C. This contrail persisted for more than six hours during which time it was visible in the GOES satellite imagery.

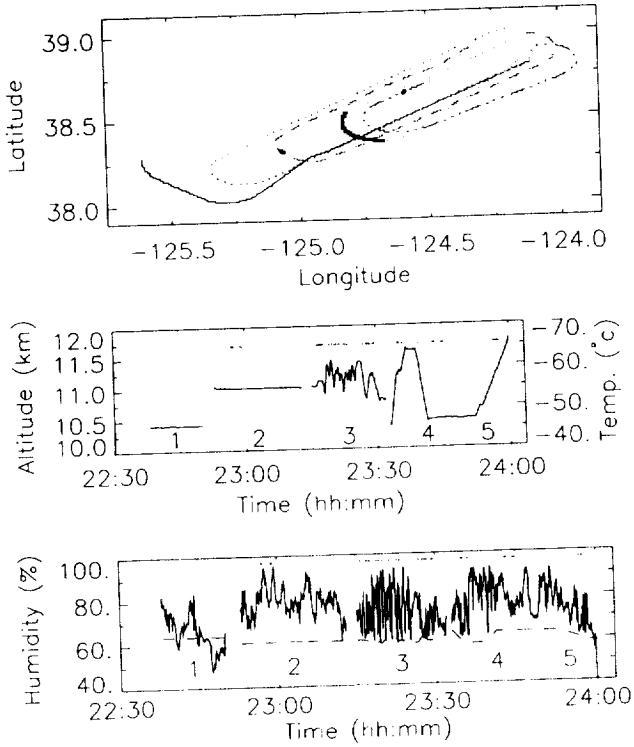

Fig. 1. DC-8 measurements on 12 May 1996. Top: DC-8 track. Pen. 1: 2238–2250 UTC (solid line); 2: 2253–2313 (dotted); 3: 2315–2332 (long dashes; 4: 2333–2349 (dark solid and small dots); 5: 2350–2400 (dash dotted). B: Time plot of B: pressure height (km) (left ordinate) and corresponding temperature (right), with penetration numbers shown, and C: Time plot of RH (solid line), RH_i (dashed), and locations where NO > 100 ppmv (dots).

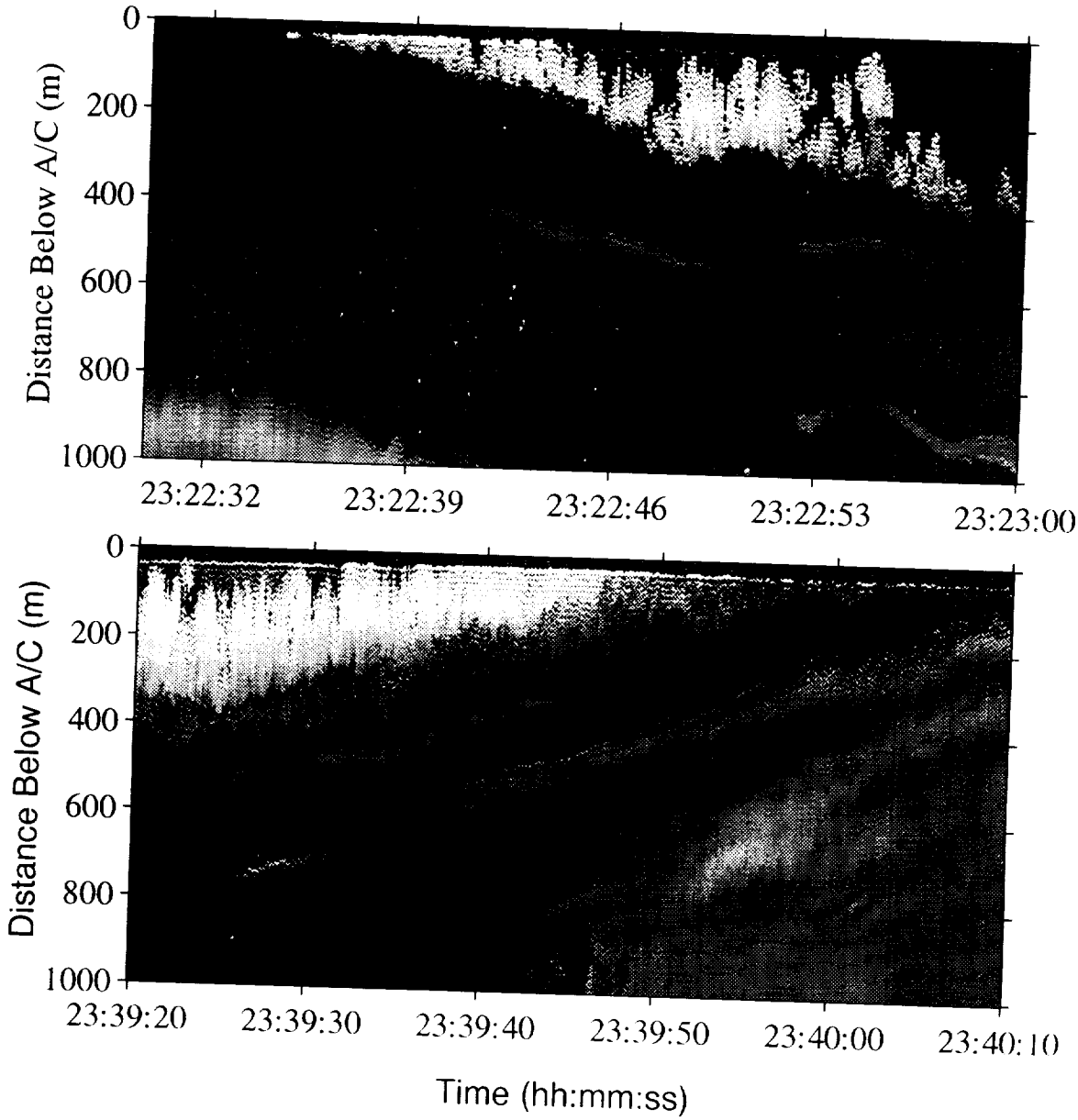

Fig. 2. Downlooking lidar data from Pen. 3 (top), when the DC-8 climbed from 11.0 to 11.4 km, and Pen. 4, when it descended from 11.5 to 11.0 km.

The DC-8's lidar, *see* Uthe et al. (1998), was nadir-pointing for the first seven min. of Pen. 2 and detected patchy cirrus extending to between 0.5 and 1.0 km below the aircraft. For the remainder of Pen. 2, visual observations indicated that the contrail was often distinct, but occasionally mixed with the ambient cirrus.

During Pen. 3, the DC-8 entered the Pen. 2 contrail at least sixteen times. Inside the contrail, NO concentrations significantly exceeded the background levels of less than about 50 pptv, *see* Weinheimer *et al.* (1997); we define periods where NO > 100 pptv as "high NO" periods to identify the contrail core. Fig. 1D shows that where NO > 100 pptv, RH $\approx$ RH_i = 62%, and where NO <100 pptv, outside the contrail, primarily RH >> RH_i.

Lidar observations from an ascent through the contrail during Pen. 3 show the contrail as an area of relatively high brightness (reflectivity) with a cellular-like structure that extends through a several hundred meter deep layer (Fig. 2A). As the aircraft climbed through the contrail layer, the lidar (downward viewing) became more visible. The lidar observations show the presence of less reflective, non-contrail cirrus below. The sharp contrast between contrail and clear air at the base of the contrail indicates that virga had not yet developed.

During Pen. 4, the DC-8 penetrated visible contrail at least six times, *see* Fig. 1B. Again, RH $\approx$ RH_i inside the contrail while RH >> RH_i outside the contrail. Virga from the contrail had begun to develop as noted near the base of the contrail. The presence of contrail

precipitation was confirmed by the visual observations of the pilots.

During the Pen. 5, the DC-8 climbed from 10.5 to 11.5 km and entered the contrail only during one period. RH >> RH_i, *see* Fig. 1C.

3. Microphysical Measurements

Here, we discuss the microphysical data from 233920 and 224010 when the DC-8 descended at a constant rate through the contrail and associated virga; microphysical data for other periods is presented in Lawson et al. (1997). Figure 2B shows the lidar data. Air parcel trajectory calculations using the DC-8 measured horizontal winds indicate that this part of the contrail was produced at approximately 230400 and had not been repenetrated in the 35 min. from the time of production.

The instruments used to characterize the contrail microphysics include the following:

(1) A Multiangle Aerosol Spectrometer Probe (MASP), *see* Baumgardner et al. 1995, measuring size spectra from 0.4 to 40 μm diameter; concentrations between > 1 and > 40 μm are used here;

(2) A particle imaging nephelometer (PI), *see* Lawson et al. 1997, providing ice particle images and size spectra for particles exceeding $\sim$ 20 μm diameter;

(3) A video ice particle sampler (VIPS), *see* Heymsfield and McFarquhar (1996) to estimate the particle size spectra for particles in this study above 30 μm diameter; and,

(4) A PMS 2D-C imaging probe with a lower detection threshold of between 50 and 100 μm.

Figure 3 shows data taken through the contrail core as a function of height during the descent along the upper abscissa and time along the lower abscissa. The aircraft descended through the contrail and precipitating region at an approximately constant rate so time and height are nearly linearly related; temperatures warmed from -56 to -52°C. The shaded region in Fig. 3 defines the contrail core (from NO). Here, RH $\approx$ RH_i = 62 to 64 %, while on either side of the core, RH >> RH_i.

The contrail core contained high concentrations of small ice crystals *see* MASP data, Fig. 3B. The adjacent, non-contrail regions contained orders of magnitude fewer crystals predominantly < 100 μm. While maximum particle dimensions were at most < 100 μm in the contrail core, *see Fig. 3C*, they extended to 250 μm in the high RH, peripheral regions *see* Fig. 3C and Lawson et al. 1997. While the particles in the contrail core were small and indistinct in shape (see images), particles in the high RH regions were typically well-defined bullet rosette crystals, typifying growth in a high RH environment.

Note that large crystals are also observed *above* the contrail core in Fig. 3. Gierens (1996) shows that the rms air vertical velocity in the contrails are on the order of the crystal terminal velocity, suggesting that vertical motions could explain transport of crystals above the contrail.

4. Discussion

The environmental and contrail conditions discussed below probably occur in most situations where precipitation trails are produced by "cold" contrails, *i.e.* those forming below -50°C, like the one studied here.

- The ice particles in the contrail core primarily develop in an environment where RH is close to but slightly greater than RH_i. As the small particles leave the contrail interior, the lack of natural cirrus is necessary to provide relatively high RH environmental air where the contrail crystals can grow.
- A sustained region of high RH air is required because the ice crystals grow slowly at temperatures lower than -50 °C, *see* Gierens 1996. The larger crystals in the contrail periphery (Fig. 3) grew to at most 250 μm from

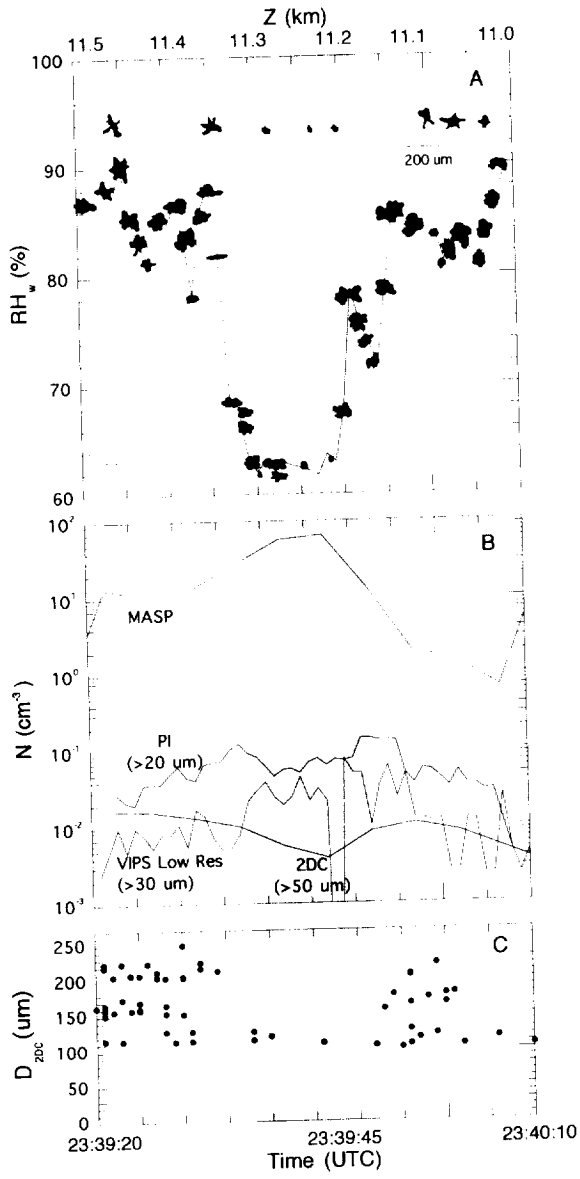

Fig. 3. Relative Humidity and microphysical properties for 23:39:20 to 23:40:10, during DC-8 descent, for same time period as in Fig. 2B. Shading: high NO region. Water vapor and microphysical properties as a function of time during descent through contrail for time period corresponding to lidar data in Fig. 2 A: RH, examples of observed ice crystals. B: Concen. from MASP (1 to 40 μm), PI nephelometer, VIPS, and 2D-C. C: Size of largest particle from 2D-C.

the time of generation approximately 2100 sec earlier, or with an average growth rate for the largest crystals of 0.12 μm s^{-1}.

• A relatively deep layer of high RH air is required for ice particles outside the contrail perimeter to prevent sublimation and promote further development following ice crystal fallout into the environment below. In effect, this deep layer of high RH air makes the precipitation trails visible. Our observations show that the environmental conditions were supersaturated with respect to ice for depths of at least 0.7 km below the initial contrail height for most of the contrail, *see* Fig. 2. These broad, sustained regions of high RH suggest the presence of large scale upward vertical motion.

Finally, high initial concentrations of ice crystals within the contrail core are required because the existence of a precipitation trail implies the continuous flux of ice crystals from the contrail to the precipitation trail over time periods exceeding 30 min. Furthermore, high initial ice crystal concentrations are also needed because the contrail spreads substantially in the horizontal, *see* Gierens 1996.

5. Conclusion

Occasionally, contrails generate precipitation trails such as those observed during the 12 May 1996 SUCCESS contrail study. The unique aspects of this study included:

(1) The generation of a distinctive-shaped contrail by a research aircraft equipped with a state-of-the-art instrument complement in a largely cirrus-free environment;

(2) Environmental conditions that were highly supersaturated with respect to ice;

(3) In-situ sampling and lidar mapping of the resultant contrail over a one hour period; and,

(4) A distinguishable contrail that persisted for over six hours.

Inside the contrail core, ice crystal concentrations were $\sim 10^1$ to 10^2 cm^{-3}, with few crystals > 100 μm in dimension. In the peripheral regions, concentrations of crystals < 100 μm were one to two orders of magnitude lower, but concentrations of crystals > 50 μm were higher, 0.01 to 0.1 cm^{-3}, comparable to those measured by Knollenberg. Significant concentrations of crystals > 100 μm were noted on the contrail periphery, and sizes up to 250 μm were detected. We suggest that turbulence allows some ice crystals to be selected for preferential growth, serving as a source of particles for the associated precipitation trails.

Particular environmental conditions are shown to be needed for contrails to produce precipitation trails, especially at the temperatures studied here as ice crystal growth rates are very low at temperatures < -50°C. In the highly ice-supersaturated growth environment studied here, linear growth rates to 250 μm averaged only 0.12 $\mu m s^{-1}$. Favorable environmental conditions include: a largely cirrus-free environment, a sustained growth period in high relative humidity conditions (implying sustained upward vertical motions), and a deep layer of high relative humidity.

Acknowledgments. We wish to thank Ed Uthe, Steve Aulenbach, Cindy Twohy, Bruce Gandrud, Andy Weinheimer, Tara Jensen and Martine Bunting. This study at NCAR was supported by NASA/SUCCESS grant A49760D; NASA/FIRE-III grant L55549D; and Air Force F49620-96-C-0024. At SPEC Inc., grants included: NASA/SBIR NAS1-19591, NASA/SUCCESS NAS2-14258, and NASA FIRE NAS1-96015.

References

Appleman, J., The formation of exhaust condensation trails by jet aircraft, Bull. Am. Meteorol. Soc., *34*, 14-20, 1953.

Gierens, K. M., Numerical simulations of persistent contrails. J. Atmos. Sci., 53, 3333-3348.

Heymsfield, A. J., and G. M. McFarquhar, On the high albedos of anvil cirrus in the tropical Pacific warm pool: Microphysical interpretations from CEPEX and from Kwajalein, Marshall Islands, *J. Atmos. Sci.*, *53*, 2424-2451, 1996.

Khrgian, A.Kh., and I.P. Mazin, Condensation trails in the atmosphere, *Trudi CAO* (in Russian) *017*, 3-19, 1955.

Knollenberg, R. G., Measurements of the growth of the ice budget in persisting contrail, *J. Atmos. Sci.*, *29*, 1367-1374, 1972.

Konrad, T. G., and J. C. Howard, Multiple contrail streamers observed by radar, *J. Appl. Meteor.*, *13*, 563-572, 1974.

Lawson, R. P., A. J. Heymsfield, T. L. Jensen, and S. M. Aulenbach, Shapes, sizes and light scattering properties of ice crystals in cirrus and a persistent contrail during SUCCESS. *Geophys. Res. Letter*, in press.

Schmidt, E., Die Entstehung von Eisnebel aus den Auspuffgasen von Flugmotoren, in *Schriften der Deutschen Akademie der Luftfahrtforschung*, no. 44, pp. 1-22, R. Oldenbourg, München, 1941.

Schumann, U., On the effect of emissions from aircraft engines on the state of the atmosphere, *Ann. Geophs.*, *12*, 365-384, 1994.

Twohy, C.H. and Gandrud, B., Ice-Forming Particles in Aircraft Exhaust. Submitted to *Geophys. Res. Let.*, 1997.

Uthe, E. E., N. B. Nielsen, and T. E. Osberg, DC-8 scanning lidar applications during SUCCESS. Submitted to *Geophys. Res. Let.*, 1997.

Vay, S. A., B. E. Anderson, G. W. Sachse, J. E. Collins, J. R. Podolske, C. H. Twohy, B. W. Gandrud, B. L. Gary, K. R. Chan, S. L. Baughcum, and H. A. Wallio, DC-8-based Observations of Aircraft CO, CH4, N2O, and H2O(g) Emission Indices during SUCCESS. Submitted to *Geophys. Res. Let.*, 1997.

Weickmann, H., 1947: Die Eisphäse in der Atmosphäre. *Library Trans. 273*, **Royal Aircraft Establishment**, Farnborough England, 96 pp.

Weinheimer, A. J., T. L. Campos, J. G. Walega, F. E. Grahek, B. A. Ridley, D. Baumgardner, C. H. Twohy, B. Gandrud, and E. J. Jensen, 1997: Uptake of NOy on Wave-Cloud Ice Particles. Submitted to *Geophys. Res Let.*.

Andrew J. Heymsfield, National Center for Atmospheric Research, P.O. Box 3000, Boulder, Colorado 80307.

R. Paul Lawson, SPEC, Inc., 5401 Western Ave., Boulder, Colorado 80301.

G. W. Sachse, National Aeronautics and Space Administration, Langley Research Center, 5 North Dryden Street, Hampton, Virginia 23681.

(Received August 22, 1997; revised November 25, 1997; accepted December 23, 1997.)

GEOPHYSICAL RESEARCH LETTERS, VOL. 25, NO. 9, PAGES 1331-1334, MAY 1, 1998

Shapes, sizes and light scattering properties of ice crystals in cirrus and a persistent contrail during SUCCESS

R. Paul Lawson
SPEC, Inc., Boulder, Colorado 80301

Andrew J. Heymsfield and Steven M. Aulenbach
National Center for Atmospheric Research, Boulder, Colorado 80307

Tara L. Jensen
SPEC, Inc., Boulder, Colorado 80301

Abstract. A persistent contrail in the shape of a racetrack was generated by the NASA DC-8 research aircraft during the SUCCESS project. The contrail was visible on GOES imagery for six hours. Microphysical measurements collected by the DC-8 show that after 40 min the core of the contrail contained mostly small (1 to 20 μm) ice particles in concentrations >1000 L^{-1}, with larger (>300 μm) ice crystals in concentrations < 10^{-4} L^{-1}. In contrast to the core, the contrail periphery contained about an order of magnitude less ice particles in the 1 → 20 μm range and about three orders of magnitude more ice particles >300 μm. The larger ice crystals in the periphery were mostly columns and bullet rosettes, similar to habits of larger ice crystals found in ambient cirrus in the area. Measurements suggest that the shape of phase functions of randomly-oriented columns and rosettes are mostly featureless. The measured phase functions are closest in shape to those predicted by ray-tracing theory for random-fractal and spatial-dendrite ice crystals.

1. Introduction

A persistent contrail was formed by the NASA DC-8 research aircraft at about 11 km (-55°C) offshore of San Francisco on 12 May 1996 during the Subsonic Aircraft: Contrail and Cloud Effects Special Study (SUCCESS) project. Heymsfield et al. (1997) (in this issue) show the racetrack-shaped flight track of the DC-8 and the resulting contrail, along with measurements of lidar backscatter, relative humidity, particle concentration and size. The persistent contrail, with its distinctive racetrack pattern, was visible on GOES satellite imagery for about six hours while it moved eastward over the California mainland and dissipated in the lee of the Sierra Nevada mountains. Precipitation streamers, visible from the bottom of the contrail, were occasionally noted by the pilots on the DC-8.

In situ measurements from Heymsfield et al. (1997) show that, in the ambient environment and at the periphery of the contrail, the vapor content of the air was typically 20 - 40% supersaturated with respect to ice. On the other hand, the core of the contrail was at vapor saturation, the excess vapor being depleted by small (< ~20 μm) particles in concentrations of about 1 to10 cm^{-3}. The measurements suggest that a turbulent process results in a small percentage of the particles being mixed from the core into the vapor-rich environment at the periphery of the contrail, where they grow to sizes > 300 μm and may form virga (i.e., precipitation streamers). The in situ measurements are in general agreement with earlier work by Knollenberg (1972) and Heymsfield (1973).

Persistent contrails have been observed to coalesce into clouds which take on the appearance of cirrus and can act to measurably reduce the incoming solar radiation in heavily trafficked flight corridors of Europe and elsewhere (Bakan et al. 1994). The light-scattering properties of ice crystals and radiative characteristics of cirrus clouds are strongly dependent on particle shape (Mishchenko et al. 1996a). A new in situ sensor, which was installed for the first time on the DC-8, provided high-resolution (5 μm) digital images of the ice particles. The instrument, called a particle imaging nephelometer, or Π-Nephelometer, simultaneously records the particle image and measures the scattering phase function of the imaged particle. The shapes of ice particles with images >~50 μm are readily discernible and provide information of typical particle shapes in the periphery of the contrail and in cirrus which occurred naturally in the vicinity of the contrail. Measurements collected in the Colorado State University (CSU) dynamic cloud chamber (DeMott et al. 1990) after the SUCCESS project were used to correlate the imaged particles with the scattering phase function.

The measurements on 12 May 1996 show that the size distributions of particles within the core of the contrail differ from those on the periphery, in the precipitation streamers and in the ambient cirrus. Consequently, the light-scattering properties of these regions can be expected to differ, which in turn influences their optical and radiative characteristics.

2. Instrumentation

The NASA DC-8 was extensively instrumented for microphysical research. In addition to the Π-Nephelometer, microphysical measurements from instruments discussed in this paper include:

(1) A multi-angle aerosol spectrometer probe (MASP), described by Baumgardner et al. (1996), measures particle size distribution in the range from 0.3 - 40 μm;

(2) a video ice particle sampler (VIPS), as described by Heymsfield and McFarquhar (1996), uses 30 Hz video images to estimate the particle size spectra for particles of at least 5 μm diameter. During this flight, there was a focusing problem which limited the minimum detectable size to 30 μm; and

(3) a PMS 2D-C probe (Knollenberg 1981) with a lower detection threshold of between 50 and 100 μm.

The Π-Nephelometer casts an image of a particle on a 400,000 pixel solid-state camera by freezing the motion of the particle using a 25 ns pulsed, high-power (60 W) laser diode. Unique op-

Paper number 98GL00241.
0094-8534/98/98GL-00241$05.00

tical imaging and particle detection systems (PDS) precisely detect particles and define the depth-of-field (DOF) so that at least one particle in the image is almost *always in focus*. This eliminates out-of-focus sizing errors that have plagued the conventional 2D imaging probes (Korolev et al. 1991, 1998).

The Π-Nephelometer was designed to record up to 25 frames s^{-1}, although a software bug prevented the instrument from recording more than 5 frames s^{-1}. This severely limited the imaging sample volume.[1] However, the particle detection system was always active and recorded the number of particles > ~ 20 μm which traversed the 3 mm by 4 mm particle detection area. At 225 m s^{-1}, the sample volume of the PDS is 2.8 L s^{-1}. Particle size distributions were computed by averaging several seconds of image data and scaling the concentration using measurements from the PDS.

The scattered light system (SLS) consists of twenty-eight 1-mm optical fibers connected to microlenses bonded on the surface of avalanche photo diodes (APDs). The fibers are placed at discrete angles of 11, 20, 28, 37, 45, 53, 61, 70, 110, 118, 127, 135, 143, 152 and 160°. The field of view of each fiber is about ± 2°, except for the 11° fiber which integrates forward scattered light from about 3.5 → 18°.

3. Size distributions and shapes of ice crystals

Heymsfield et al. (1998) show five DC-8 racetrack-shaped flight patterns on 12 May 1996 which often overlap and sometimes intersect ambient cirrus clouds which were scattered over the area. The ambient cirrus and overlapping contrails confounded unique determination of the origin of the ice particles. The central cores of the contrails were often detectable from distinctly elevated NO_x concentrations (Weinheimer et al. 1997). The peripheries of the contrails were delineated on either side of the central core. The contrails and precipitation streamers were occasionally visible from the cockpit of the DC-8, and intercom voice notes were used to determine the position of the aircraft relative to the visible contrail. Lidar observations, shown in Heymsfield et al. (1998), were also used to identify cirrus that was above or below the aircraft. These composite observations were used to select representative regions of the contrail core, periphery and ambient cirrus.

Ambient cirrus. The cirrus clouds in the area near the contrail were mostly thin, patchy and contained occasional particles up to 1 mm in maximum dimension. Fig. 1 shows a combined particle size distribution using the MASP, VIPS, Π-Nephelometer and 2D-C probes along with examples of images of particles observed by the Π-Nephelometer from 225230 - 225630 GMT. There is good general agreement in the shapes of the particle size distributions measured by the VIPS, Π-Nephelometer and 2D-C probes for particles from about 75 – 500 μm. In Fig. 1, the columns extend to about 200 μm in length and the maximum dimensions of bullet rosettes are up to 600 μm. The shape of the smallest (< 50 μm) particles often cannot be determined. They usually appear to be mostly spheroidal in shape, however, this may be due to the Π-Nephelometer 5 μm pixel resolution, which is not always adequate to resolve the edges of plates < 50 μm. As a result, in this paper we have elected to classify small particles that appear spherical in shape as "unresolved spherical". The shape of particles from 50 to 200 μm are mostly columnar and/or rosettes, and particles > ~200 μm are usually bullet rosettes.

[1] Upgrades after completion of the SUCCESS project included a 1 million pixel CCD camera, 2.3 μm pixel resolution, increased optical contrast and 40 frames s^{-1} data recording rate (see Lawson et al. 1998).

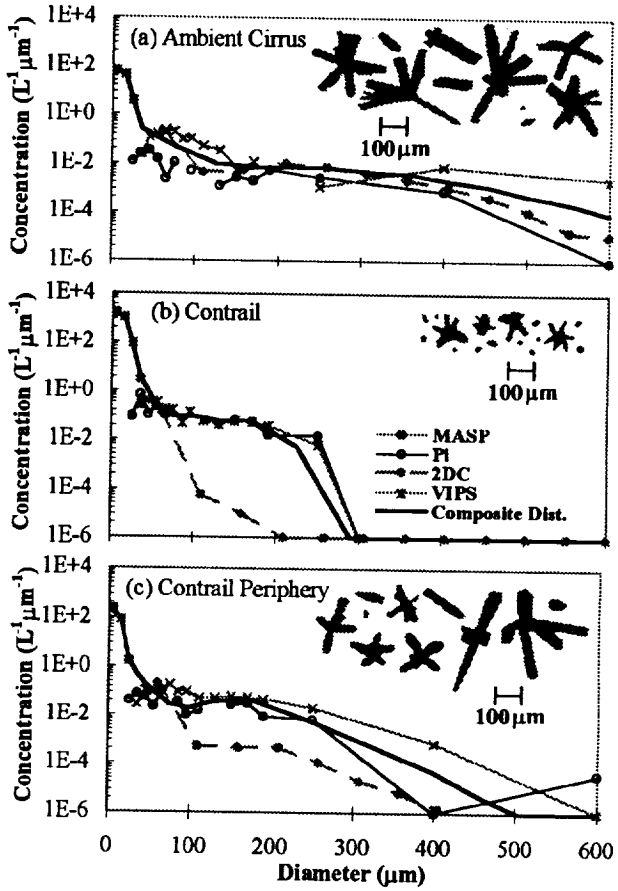

Figure 1. Particle size distributions from the MASP, VIPS, Π-Nephelometer (Pi), 2D-C measurements and composite distribution in (a) ambient cirrus, (b) contrail core and (c) contrail periphery. Examples of images from the Π-Nephelometer are shown next to each case.

Contrail cores. The central cores of contrails typically contain high concentrations of small ice particles (Knollenberg 1972; Heymsfield et al. 1998). A contrail core, identified by NO_x > 100 ppt was sampled from 233938 to 233952 (Heymsfield et al. 1998). The composite size distribution shown in Fig. 1 is dominated by the small particles seen by the MASP. Images of the small particles recorded by the Π-Nephelometer were classified as "unresolved spherical". High-resolution replicas seen on the Desert Research Institute (DRI) home page (http://www.dri.edu) suggest that particles < 20 μm in contrails are often plates and columns, combined with irregular and spheroidal shapes. However, the crystals seen on the DRI home page were all observed in an environment with low (< ice saturation) relative humidity and may not be representative of the 12 May contrail, which was typified by very high relative humidity. More than 99% of the ice particles in the core of the 12 May contrail were < 20 μm and the low concentration of 100 to 250 μm rosettes may have mixed in from the contrail periphery (Heymsfield et al. 1998).

Contrail periphery and precipitation streamers. Heymsfield et al. (1998) show data from a penetration of a contrail that was about 40 min old. The DC-8 penetrated the contrail downward from above. Data from the lidar suggested that the contrail itself was not contaminated from cirrus aloft and that there were some regions that contained precipitation streamers. Heymsfield et al. (1998) show MASP measurements of total concentration of particles from about 1 to 10 μm in the contrail

periphery that are 1 to 2 orders of magnitude lower than in the core. The composite particle size distribution and Π-Nephelometer images shown in Fig. 1 suggest that the contrail periphery contains particle types that are very similar to ambient cirrus, with the exceptions that there are additional small particles and fewer particles in the 300 – 600 μm range. Heymsfield et al. (1998) suggest that a turbulent process occurs whereby some particles in the core are mixed into the vapor-rich region of the periphery and grow to larger sizes.

As the DC-8 continued its descent, it may have also penetrated precipitation streamers below the contrail; however, some of the regions also contained ambient cirrus and separating the two was unambiguous. Basically, the data suggest that the particles continued to grow in the vapor-rich environment as they precipitated from the contrail, sometimes reaching sizes up to about 1 mm. The habits of particles in the precipitation streamers appeared to be dominated by bullet rosettes.

4. Light scattering properties of the ice crystals

Calculations shown in Mishchenko et al. (1996a) suggest that using the wrong scattering phase function in retrieving cloud optical thickness can result in an overestimation or underestimation of optical thickness by more than a factor of three. The Π-Nephelometer was used to measure the phase functions of ice crystals in the CSU cloud chamber. Before the data collection, extensive laboratory tests were conducted with water drops and glass beads. Comparisons with Mie scattering theory for 20 to 200 μm *water drops* and Π-Nephelometer measurements were in good relative agreement. However, measurements of 50 and 100 μm *glass beads* scattered nearly an order of magnitude more light in the region from 80° to 120° than predicted by Mie theory for a spherical glass bead. Gayet (1997 - personal communication) observed a nearly identical departure from Mie theory in the 80° to 120° region when measuring phase functions from glass beads with a polar nephelometer (Gayet et al. 1997). Mishchenko et al. (1996b) found very similar results when comparing micron-size spheres with equivalent area spheroids and soil particles. This suggests that even minute degrees of non-sphericity can lead to large differences in phase functions.

Fig. 2 shows phase functions for 20 μm water drops generated in the laboratory and ice particles observed in the CSU cloud chamber along with examples of Π-Nephelometer images. All of the phase functions shown in Fig. 2 are normalized to the light intensity measured at the 20° scattering angle for a 20 μm water drop. The dynamic chamber was operated in a way such that a cloud was formed by an adiabatic expansion at about -20°C (540 mb), seeded at -28°C and ice crystals grew as the expansion continued to about -42°C (380 mb). The Π-Nephelometer images were sorted by size and the particle shapes observed in the 12 May contrail and ambient cirrus. Figure 2 shows that the relative intensities of the phase functions for small (20 to 50 μm) particles are strongly a function of particle shape. The data show that in the 20 to 50 μm (Sm.) size range, progressively more light is scattered (from about 40° → 160°) as the particle shape becomes more complex, from water drops → unresolved spheroids → irregulars → columns and rosettes. In Fig. 2, for the 50 to 90 μm (Med.) and 90 to 210 μm (Lg.) size ranges, it appears that the influence of particle shape on phase function decreases. For particles > 50 μm, the data suggest that size is the significant factor influencing the amount of light scattered.

Figure 2 also shows phase functions derived from ray-tracing for a dendrite (Takano and Liou 1995), a column and a fractal (Mishchenko et al. 1996a). The prominent 22° halo seen for the

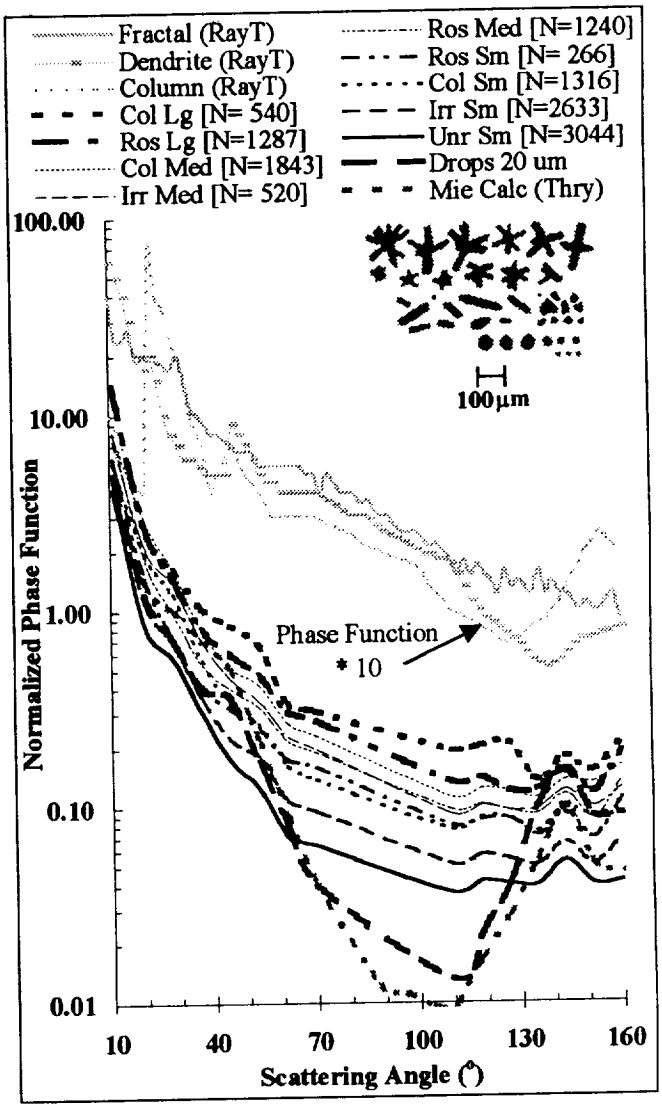

Figure 2. Normalized phase functions derived from measurements of ice crystals in the CSU cloud chamber compared with theory. Lighter lines offset by one decade toward the top of the figure are phase functions derived from ray-tracing for random-fractal and columnar crystals (Mishchenko et al. 1996) and a spatial dendrite (Takano and Liou 1995). Shown in lower part of figure (top to bottom) measurements from columns (Col), bullet rosettes (Ros), irregular shaped crystals (Irr), and unresolved spherical (Unr), 20 μm drops, and Mie Theory (Thry) for 20 μm drop, Size bins indicated in legend for measured crystals include 20-50 μm (Sm.), 50-90 μm (Med.), and 90-210 μm (Lg.). Number (N) of measurements for each crystal type is included in legend. Also, examples of Pi-Nephelometer images of bullet rosettes (top row), columns and irregular shapes (middle row), and unresolved spherical crystals (bottom row) are shown in the middle right of the figure.

column is not observed in the measurements. Mostly, the measured phase functions are featureless with some suggestion of a peak near 145°. The best agreement between the measurements and ray-tracing theory appears to be with the fractal and dendritic crystals. Nikiforova et al. (1978) and Volkovitskiy et al. (1980) also made measurements in a cloud chamber. They used a "Rassvet" device (Nikiforova et al. 1978), which averaged meas-

urements over a range of discrete angles and a time period of 10 s. The phase functions shown by Nikiforova et al. (1978) do not display the 22° halo for the small ice crystals and the authors comment that the 22° halo was only observed in clouds with low optical density. Interestingly, Nikiforova et al. (1978) do show a slight bump at 145° for both ice and water clouds. Volkovitskiy et al. (1980) show a 22° halo in their measurements, although they comment that it is not nearly as prominent as predicted from ray-tracing. The principal difference between the measurements using the Rassvet device and the Π-Nephelometer, is that crystals are sucked through a 25 mm sample tube in a *random* orientation in the Π-Nephelometer, and they are allowed to fall undisturbed through the Rassvet device. Apparently, under conditions where the optical density is low and hexagonal crystals are allowed to fall naturally with the c-axis oriented vertically, the 22° halo is observed in the cloud chamber with the Rassvet device.

5. Discussion and summary

Measurements in the 12 May SUCCESS contrail show that the ice particles observed in the core were small, mostly 1 → 20 μm, and while they appeared spheroidal in shape, instrument resolution prevented determination of plates and similar shapes that may appear to be nearly spherical. On the contrail periphery, where the relative humidity exceeded ice saturation by 20-40%, ice particles as large as 300-500 μm were observed. Particle shapes in the periphery included unresolved spherical, irregular, columnar and bullet rosette. Ice crystals larger than about 200 μm were typically bullet rosettes. It is postulated (Heymsfield et al. 1998) that the larger crystals fall out of the contrail periphery and become precipitation streamers. The shapes of ice particles in the contrail periphery were typical of those sampled in patches of cirrus observed in the area; however, the cirrus contained fewer small particles and more larger ice crystals, extending to sizes of 600 μm and occasionally 1 mm.

The shapes and sizes of ice particles generated in the CSU cloud chamber were remarkably similar to those observed in the contrail and ambient cirrus. Measurements of phase functions in the cloud chamber suggest that for small randomly-oriented (< 50 μm) ice particles, as the crystal departs more from a spherical shape, relatively more light is scattered in the 40° → 160° region. Volkovitskiy et al. (1980) also found that more light is scattered from ice particles than cloud drops in this range of angles, and they suggest that this is due to relatively weaker scattering for ice particles in the 2 → 40° range. Our measurements suggest that light scattered in the 40° → 160° range from randomly-oriented ice crystals > 50 μm has a weaker dependence on crystal type and that crystal size is the dominant factor. Of course, these conclusions are based on a limited data set, about 12,000 individual ice crystals generated in a cloud chamber, and more data are needed for additional verification.

Acknowledgments. The authors wish to thank Dr. Greg McFarquhar for his help with VIPS and 2D-C data and Dr. Darrel Baumgardner for providing MASP data. We would also like to thank Dr. Tim Quakenbush and Dr. Paul DeMott for their assistance in obtaining the Π-Nephelometer data. We are grateful for suggestions made by two anonymous reviewers. Finally, Cheryl Hilliard is thanked for her help in the preparation of this manuscript. The SPEC, Inc. part of this study was supported by the following programs: NASA/SBIR NAS1-19591, NASA/SUCCESS NAS2-14258 and NASA FIRE NAS1-96015. Grants to NCAR include: NASA/SUCCESS grant A49760D; NASA/FIRE-III grant L55549D and Air Force Office of Scientific Research grant F49620-96-C-0024.

References

Bakan, S., M. Betancor, V. Gayler and H. Grassl, 1994: Contrail frequency over Europe from NOAA-satellite images. *Annal. Geophys: Atmos., Hydro. and Space Sci., 12*, 962.

Baumgardner, D., J. E. Dye, B. Gandrud, K. Barr, K. Kelly and R. K. Chan, 1996: Refractive indices of aerosols in the upper troposphere and lower stratosphere. *Geophys. Res. Let., 23*, 749-752.

DeMott, P. J., D. C. Rogers and R. P. Lawson, 1990: Improvements to the CSU controlled-expansion cloud chamber. Preprints: ICCP Conference on Cloud Physics, San Francisco, 126-129.

Gayet, J-F, O. Crépel, J-F Fournol and S. Oshchepkov, 1997: A new airborne Polar Nephelometer for the measurements of optical and microphysical cloud properties. Part I: Theoretical design. *Annales Geophysicae, 15*, 451-459.

Heymsfield, A. J., 1973: Laboratory and field observations of the growth of columnar and plate crystals from frozen droplets. *J. Atmos. Sci., 30*, 1650-1656.

Heymsfield, A. J. and G. M. McFarquhar, 1996: On the high albedos of anvil cirrus in the tropical Pacific warm pool: Microphysical interpretations from CEPEX and from Kwajalein, Marshall Islands, *J. Atmos. Sci., 53*, 2424-2451.

Heymsfield, A. J., R. P. Lawson and G. Sachse, 1998: Development of ice particles precipitating from a contrail during SUCCESS. In this issue of *Geophys. Res. Letter.*

Knollenberg, R. G., 1972: Measurements of the growth of the ice budget in persisting contrail. *J. Atmos. Sci., 29*, 1367-1374.

Knollenberg, R.G., 1981: Techniques for probing cloud microstructure. *Clouds Their Formation, Optical Properties, and Effects*, P.V. Hobbs and A. Deepak, Eds., Academic Press, 15-91.

Korolev, A. V., S. V. Kuznetsov, Y. E. Makarov, and V. S. Novikov, 1991: Evaluation of measurements of particle size and sample area from optical array probes. *J. Atmos. Oceanic Technol., 8*, 514-522.

Korolev, A. V., J. W. Strapp, and G. A. Isaac, 1998: On the accuracy of PMS optical array probes. To Appear: *J. Atmos. Oceanic Technol.*

Lawson, R. P, A. V. Korolev, S. G. Cober, T. Huang, J. W. Strapp and G.A. Isaac, 1998: Improved Measurements of the Drop Size Distribution of a Freezing Drizzle Event. To Appear: *Atmos. Res.*

Mishchenko, M. I., W. B. Rossow, A. Macke and A. A. Lacis, 1996a: Sensitivity of cirrus cloud albedo, bidirectional reflectance and optical thickness retrieval accuracy to ice particle shape. *J. Geophys. Res., 101*, 973-985.

Mishchenko, M. I., L. D. Travis and A. Macke, 1996b: Light scattering by nonspherical particles in the atmosphere: An overview. *IRS'96: Current Problems in Atmospheric Radiation*, W. L. Smith and K. Stamnes, eds., Deepak Publ.

Nikiforova, N. K., L. N. Pavolova and V. P. Snykov, 1978: The "Rassvet" high-speed scattering phase function measuring system. *Trudy. IEM, 83*, 28-32.

Takano, Y. and K. N. Liou, 1995: Radiative transfer in cirrus clouds; Part III: Light scattering by irregular ice crystals. *J. Atmos. Sci., 52*, 818-837.

Volkovitskiy, O. A., L. N. Pavlova and A. G. Petrushin, 1980: Scattering of light by ice crystals. *Izvestiya, Atmos. Oceanic Phys., 16*, 98-102.

Weinheimer, A. J., D. Baumgardner, T. L. Campos, F. E. Grahek, B. Gandrud, E. J. Jensen, B. A. Ridley, C. H. Twohy and J. G. Walega, 1997: Uptake of NOy on wave-cloud ice particles. In this issue of *Geophys. Res. Let.*

T. Jensen and R. P. Lawson, SPEC, Inc., 5401 Western Avenue, Suite B, Boulder, Colorado 80301. (email: plawson@specinc.com; jensen@specinc.com)

S. Aulenbach and A. Heymsfield, National Center for Atmospheric Research, P.O. Box 3000, Boulder, Colorado 80307.

(Received August 22, 1997; revised January 16, 1998; accepted January 20, 1998.)

An Overview of Microphysical Properties of Arctic Clouds Observed in May and July 1998 During FIRE.ACE

R. Paul Lawson, Brad A. Baker and Carl G. Schmitt
SPEC Incorporated
Boulder, Colorado

1. Introduction

Cloud-radiative processes in the Arctic have a strong impact on the stability of the Arctic Ocean ice pack (Curry et al. 1993) and also have ramifications on the global energy budget (e.g., IPCC 1990). Clouds in the boundary layer are persistent during May through September and strongly influence the melting rate of the pack ice (Curry et al. 1996). The cloudy boundary layer in the Arctic is low, optically thin, and increases the summertime melt rate of sea ice, since the longwave exceeds the shortwave cloud-radiative forcing at the surface. A positive feedback scenario occurs as melt ponds and leads form and the surface albedo decreases.

Prior to the 1997-1998 Surface HEat Budget of the Arctic (SHEBA) project (Perovich et al. 1999), and the First ISCCP (International Satellite Cloud Climatology Project) Regional Experiment Arctic Clouds Experiment (FIRE.ACE) (Curry et al. 2000), there were relatively few aircraft studies of Arctic clouds. While many types of Arctic stratus clouds were investigated during SHEBA, including clouds with multiple layers that extended to above 500 mb and cirrus, thin stratus clouds within 1 km of the surface occurred most frequently and were the clouds most often investigated by the in situ research aircraft. We focus our analysis in this paper on these clouds, and refer to them as "cloudy layers" (after the terminology used by Curry et al. 1988; 1996), or "boundary layer clouds" (which was the terminology used by scientists at the FIRE.ACE field project and used in Curry et al. 2000). While Arctic boundary layer clouds may not always be thermodynamically or mechanically linked to the underlying surface, as is conventionally assumed in the classic definition, the term has been adopted here to represent low stratus cloud layers in the Arctic.

In addition to investigations of boundary layer clouds, microphysical measurements from a deep stratus cloud that extended from 2 Km to 6 Km are presented, as well as data from a cirrus cloud. These data are included in order to provide a better representation of the variability that exists in the many types of clouds observed in the Arctic. Also, the microphysical properties revealed in these investigations could be used to validate remote measurements and process models.

Curry et al. (1996) summarize findings from previous investigations of summertime Arctic cloudy boundary layers. The salient features from their study that relate to this research are summarized here.

- Three types of summertime cloud boundary layers are identified: *i*) a stable boundary layer with thin, patchy stable clouds that may be found in multiple layers, *ii*) a stable boundary layer, often with fog at the surface, that is topped by a cloud-topped mixed layer, and *iii*) a cloud-topped, well-mixed boundary layer that extends to the surface.

- Warm, moist air flows from continental regions over the pack ice and condensation is induced initially by radiative and diffusional cooling to the colder surface and longwave radiation to space.

- Clouds in the boundary layer are often well-mixed, with the mixing assumed to proceed downward from cloud top due to radiational cooling and overturning. The well-mixed layer may extend to the surface, in which case, surface effects may have also contributed to cloud formation.

- The microphysical properties of clouds associated with the Arctic boundary layer are varied and definitive trends are difficult to establish. This may be due to the relatively small microphysical data set due to a lack of measurements. Significant ice concentrations are generally observed at temperatures colder than -15° to -20° C (Jayaweera and Ohtake 1973; Curry et al. 1990). However, exceptions to this generality have been reported. Some ice has been observed in clouds at temperatures as warm as -4° C. A predominantly water cloud was observed (in wintertime) at a temperature of -32° C (Witte 1968), and Curry et al. (1997) report an all-ice cloud at -14° C. Mixed-phase clouds are often observed and the types of ice particles have not been well documented, except for surface-based observations. Curry (1986) found a significant amount of drizzle associated with a large dispersion in the droplet spectra.

The microphysical properties of FIRE.ACE clouds are investigated here using data collected by the National Center for Atmospheric Research (NCAR) C-130 research aircraft during May and July 1998. The study includes, for the first time in the Arctic, a new particle imaging probe that provides high-definition digital images of cloud particles. Data from the cloud particle imager (CPI) are analyzed to separate water drops from ice particles and identify crystal habits, compute water and ice particle size distributions. The CPI is described in more detail, along with other microphysical instrumentation used in this study, in Section 3.

The data presented in this paper are organized in the following way. A table gives an overview of the major physical features of clouds observed during the

16 C-130 missions in FIRE.ACE, focusing on clouds associated with the boundary layer. An example of a boundary layer cloud that is mostly adiabatic and homogeneous with a monomodal drop size distribution is discussed. Measurements of cloud liquid water content (LWC) are compared with the theoretical adiabatic values in the boundary layer clouds that are identified as being adiabatic. An example of a boundary layer cloud that is non-adiabatic, actively mixing at cloud top and inhomogeneous with bimodal drop size distribution is presented. Time series measurements of cloud LWC, droplet concentration, temperature and vertical velocity at different levels in six boundary layer clouds are discussed. An example of a boundary layer cloud with highly variable hydrometeor fields is discussed in some detail. Images of particles and ice/water particle size distributions in a deep stratus cloud extending from 2 km to 6 km are presented. Lastly, an example of the inhomogeneous ("clumpy") distribution of particles in a cirrus cloud is discussed.

2. FIRE.ACE Field Project

Curry et al. (2000) describe the SHEBA/FIRE.ACE project in detail. Some salient features of the project that are pertinent to the C-130 flights are excerpted here. The main goal of the experiment was to examine the effects of clouds on radiation exchange between the surface, atmosphere and space, and to study how the surface influences the evolution of the cloudy boundary layer. Data collected during the field phase of the project are being used to evaluate and improve climate model parameterizations of Arctic cloud and radiation processes, satellite remote sensing of cloud and surface characteristics, and understanding of cloud-radiation feedbacks in the Arctic.

The location and timing of the FIRE Arctic Clouds Experiment were determined by the scheduled operations of the SHEBA experimental site in the Beaufort Sea during October 1997 through October 1998. The Canadian Coastguard icebreaker *Des Groseilliers* was deployed in a multi-year ice floe on October 1, 1997, at 75°16.3' N, 142°41.2' W. The C-130 flights were planned to coincide with the current location of the ship as it drifted with the ice floe. Horizontal traverses of 20-200 km were made by the NCAR C-130 at various levels above, below and within cloud, in the boundary layer, and at various altitudes to map the surface using aircraft remote sensing instruments. Additionally, slow ascents and descents were made to obtain high-resolution slant profiles using *in situ* instruments. The ferry flight from Fairbanks to the location of the *Des Groseilliers* generally took about two hours in each direction during May, and nearly three hours in June, leaving 2 - 4 hours of on-station data collection.

3. Instrumentation

The capabilities of the NCAR C-130 and instrumentation on the research aircraft are described by Curry et al. (2000). Of particular interest to this study

are microphysical instruments used to measure cloud particle characteristics and cloud liquid water content (LWC), including

- Two King hot-wire LWC devices (King et al. 1978) manufactured by PMS with modifications to the electronics by NCAR,
- a Gerber Scientific particulate volume monitor (PVM-100A) described by Gerber et al. (1994),
- a Particle Measuring Systems (PMS) Forward Scattering Spectrometer Probe (FSSP-100), described by Knollenberg (1981),
- a PMS 260X one-dimensional optical array probe with 64 photo diodes at 10 μm pixel resolution, (Knollenberg 1981),
- very limited use of the shadow-or concentration from the PMS 2D-C two-dimensional optical array probe (Knollenberg 1981), and
- a CPI described briefly by Lawson et al. (1998), Korolev et al. (1999) and in more detail by Lawson (1997) and Lawson and Jensen (1998).

The King probe is a hot-wire device with airflow characteristics that are theoretically predictable. The response of the probe has been shown to roll-off for drops larger than about 50 μm (Biter et al. 1987). The King probes are mounted near each wing tip and close to the leading edge of the wing itself. Studies of the airflow around the probe installation on the C-130 have not been conducted. Laursen (1998) points out that the location close to the wing leading edge was a matter for concern, and one King probe was re-located and extended from the wing for one mission. However, she reports that this appeared to make no discernable difference in the measurements. The King dry-air term is a function of the (local) true airspeed, and the dry-air term is subtracted from the in-cloud reading to obtain LWC. It is therefore important to know the correct true airspeed at the probe location, or to subtract the dry air term measured outside of cloud at the same airspeed and air density. In this study, the King probe data were used as supplied by NCAR; the dry-air term is computed assuming the airspeed at the probe location is the same as that measured by the aircraft data system. Magnitudes of the errors that may be induced as a result of neglecting airflow considerations are undetermined.

The PVM-100A is an optical device that measures LWC, drop surface area and effective radius at a sample rate of 1 KHz. The light scattered in the forward direction by an ensemble of drops is optically weighted and summed on a photodetector. The measurements presented here were averaged to 1 Hz by the NCAR data processing routine. The probe was initially supplied with an improper calibration, which was modified after the field experiment by Gerber Scientific Incorporated. The re-calibrated data have been used in this paper.

Icing tunnel tests were conducted after the field experiment to calibrate the LWC devices. The King probes performed well in the tunnel after the gain of one of the probes was adjusted in software to compensate for an improper hardware

setting. When the drop median volume diameter (MVD) was <~25 μm, both King probes generally measured LWC to within 10% of the tunnel value (Strapp, personal communication). The Gerber PVM probe on the C-130 was not functioning for the icing tunnel tests. The University of Washington (UW) operated an identical PVM probe during FIRE.ACE and its performance in the icing tunnel tests is discussed by Garrett and Hobbs (1999). They report that during the small droplet tests the PVM underestimated LWC by 12% in the 0 to 0.75 g m^{-3} range. An analysis of the response of the UW PVM-100A to large droplet sizes showed that it had diminished response to droplets with diameter larger than 20 μm. At an MVD of 32 μm the PVM underestimated spray LWC by ~40% (compared to the 18% underestimation at a MVD of 30 μm reported by Gerber et al. (1994)).

The FSSP has been under considerable scrutiny since its introduction into the field. Processing of FSSP data by NCAR for this project included partial recovery of losses due to coincidences and probe dead time (Baumgardner et al. 1985), and adjustment of channel widths to account for airspeed corrections to the electronics (Cerni 1983; Dye and Baumgardner 1984; Baumgardner 1987). Corrections have not been made for problems in the droplet spectrum due to coincidences, as discussed by Cooper (1988) and Brenguier (1989), or due to laser beam inhomogeneities (Baumgardner and Spowart 1990; Wendisch 1998). The principle measurement of the FSSP is drop size and signals were sorted into 15 equal drop-size bins in the 3-45 μm range. The measurements were summed and recorded every 0.1s. The dynamic accuracy of the FSSP in measuring LWC and drop size is difficult to quantify. Baumgardner (1983) suggests that FSSP measurements of drop size are accurate to 17% and LWC is accurate to within 34%. However, subsequent evaluations of the FSSP have shown additional potential error terms due to coincidences (e.g., Cooper 1988), inhomogeneities in the laser beam and effects of airspeed (e.g., Wendisch et al. 1996). In addition, the accuracy of the FSSP appears to depend on factors that are not always quantifiable, such as field calibrations, optical contamination, airflow effects due to position on the aircraft, etc.

The PMS 260X probe sizes particles in 64 channels from 10 μm to 640 μm. According to Laursen (1998), 260X data processed by NCAR were filtered to eliminate the first three channels, due to changes in alignment caused by temperature variations. Thus, the first usable size channel started at 40 μm. Also, the end element photo diode voltages were monitored for indications that the probe was out of optical alignment and data were erroneous.

Laursen (1998) also reported that concentrations from the (25 μm) 2D-C and (200 μm) 2D-P image data were suspect and could be in error by a factor of two. Consequently, only the 2D-C and 2D-P shadow-or counts were output to the data

archives. The shadow-or particle concentrations reported in this paper were obtained by dividing the total counts by the true airspeed. Because there is no image information in the shadow-or measurements, conventional image processing routines that remove "artifacts" (i.e., water streaking on the mirrors and particles that break on the probe tips) can not be employed and sample volume corrections for small particles cannot be applied. Additional information describing the C-130 data contained in the FIRE.ACE can be found in Laursen (1998).

The CPI is a relatively new instrument that utilizes innovative technology to record high-definition digital images of cloud particles, and measure particle size, shape and concentration. The high quality of CPI images supports the generation of individual size distributions for (spherical) water drops and (non-spherical) ice particles. The CPI casts an image of a particle on a solid-state, one million pixel CCD camera by freezing the motion of the particle using a 25 ns pulsed, high-power laser diode. As shown in the conceptual drawing in Figure 1, a particle detection system (PDS) with upstream lasers precisely defines the focal plane so that at least one particle in the image is almost *always in focus.* Processing of CPI images significantly reduces out-of-focus sizing errors that have plagued the conventional 2D imaging probes (Korolev et al. 1998). Each pixel in the array is 2.3 μm, so particles from about 10 μm to 2mm are imaged. A video-processing engine identifies and sizes particles within the one million pixel array, saving only the regions around each image. The CCD camera can run at rates up to 40 Hz, and since more than a hundred particles per frame can be processed, data rates in excess of 1000 imaged particles s^{-1} are obtainable.

CPI particle concentration can be computed using a number of methods. Here we describe two nearly independent methodologies and an additional method that uses the 150 – 500 μm region of the PMS 260X particle size distribution to scale the CPI measurements.

When the CCD camera is being read, the PDS continues to count particles, providing a continuous measurement of total particle concentration (called the 'total strobes' measurement of concentration). The total strobes concentration is a function of the threshold level of the PDS, which is user selectable. A check on the effectiveness of the PDS can be obtained by monitoring the number of ('valid') camera frames that actually contain particles. Typically, the PDS threshold is set so that the percentage of valid frames is between 60 – 100%. Since larger particles will more reliably trigger the PDS, there is a roll-off in the particle detection efficiency that starts at about 25 μm and depends on the PDS threshold setting. Thus, the small end of particle distributions that are narrow, such as a typical distribution of cloud drops, will be undercounted.

In addition to the in-focus particle that triggers the PDS, high concentrations of small particles in the viewing area may produce additional images that are in

various degree of focus. In this case, the viewing area contains a snapshot of a known volume of particles, and an independent calculation of particle concentration, called the local concentration in this manuscript, can be determined by counting the number of imaged particles, and dividing by the viewing volume. However, the optical depth of field (DOF), and consequently the image size and sample volume of the CPI, are a function of particle size (see Lawson and Cormack 1995; Korolev et al. 1998). The CPI particle size distributions shown in this paper have been made using size and sample volume corrections that are done on a particle-by-particle basis. These corrections to the particle size distribution have a major effect on the concentration of small (< ~100 μm) particles. This is possible because CPI images, which contain 256 grey levels, can be used to accurately determine the focus of the image and the distance from the object plane (see Lawson and Cormack 1995).

Due to varying DOF, the imaging sample volume of the CPI varies from about from 0.002 to 0.2 cm^3. Local particle concentrations are a true measure within the small volume that is imaged, but they need to be averaged over several tens or hundreds of snapshots to avoid large errors due to sampling statistics. This local concentration is still biased towards the small volumes where the concentration is highest, because the likelihood of triggering is higher where there are more particles. In regions with low particle concentrations, or highly inhomogeneous cloud, the local concentration can be many orders of magnitude greater than the average concentration. Thus, the CPI size distributions must be scaled to the average concentration. In this study, the 260X size distribution, where it overlaps the CPI size distribution, was used as the first choice for this scaling (since the PMS 2D-C particle size distributions were not available from the data archives). Where the 260X data were unreliable, the FSSP size distribution was used. This method attempts to make use of the best measurement characteristics of each instrument. As a stand-alone instrument, the CPI total strobes average concentration may be used for this scaling. This is most applicable when particle concentrations are relatively low (< ~1000 L^{-1}) and uniform, and the CPI PDS threshold settings are relatively low and unchanging.

Due to the high resolution of CPI images and the 256 gray levels, it is possible to distinguish spherical from non-spherical particles, depending on the level of focus and size of the particle. Generally, particles that are in good focus and > 50 μm can be distinguished as spherical or non-spherical. This is useful for separating water drops and ice particles in mixed-phase clouds, since ice particles will generally grow to recognizable non-spherical shapes in less than a minute in a mixed-phase cloud. In this study, we used a focus algorithm to automatically reject images that were not in sharp focus and then they were classified by another software algorithm that measures the roundless of the image. We also classified several hundreds of particles by eye to verify the accuracy of the automated algorithm. The agreement between the automated and manual techniques was very good for images >~40 μm. In regions where classification of images < ~40 μm was essential, such as in regions with ice

multiplication, a manual classification of particles was implemented. If particles smaller than about 20 μm could not be confidently classified, they were classified as water drops.

4. Arctic Boundary Layer Clouds

4.1 Overview

Sixteen research missions were conducted during FIRE.ACE by the C-130. Half of the 16 missions were flown in May 1998 and the remainder were flown in July 1998. Of the 16 missions, we identified 11 cases when there were boundary layer clouds. Here we classify a boundary layer cloud as one that is well-mixed from the surface to cloud base, or if it has a cloud base that is <300 m. Table 1 shows the flight number, date, temperature, cloud base, cloud top, cloud classification, mixing depth and some general microphysical characteristics of each of the 16 missions. Upper air soundings were taken from the SHEBA ship approximately every six hours. The mixing depth was determined by analysis of the sounding that was closest in time to the flight profile, so some of the fine atmospheric structure may be missed in this analysis. Even so, there appears to be a definitive difference in the subcloud properties in May and July. In May, six out of eight cases had boundary layer clouds and all six clouds were mixed from the surface to cloud base. The depths of the mixing layers in May ranged from 150 to 1200 m. In July, five of the eight cases had boundary layer clouds, but none of these were mixed from the surface to cloud base.

4.2 Mostly Adiabatic, Homogeneous Water Clouds

The C-130 flew a total of 21 slant profiles on 15, 18, 27 May and 29 July through boundary layer clouds that consisted almost entirely of liquid water. In cloud physics literature, adiabatic generally implies both adiabatic and closed in classical thermodynamics terms. That is, when a parcel of air undergoes an adiabatic ascent from cloud base, it does not exchange mass or heat with its environment. Under these conditions the LWC and temperature can be predicted theoretically from the cloud base temperature and pressure (see Lawson and Blyth 1998). In addition, the cloud drop size distribution can be estimated using the droplet growth equation (see Pruppacher and Klett 1978). Basically, during adiabatic ascent the mean drop size will grow monotonically and the drop size distribution will remain monomodal. Bimodal droplet size distributions, (not observed in these homogeneous clouds) often result from mixing with environmental air (above cloud top), followed by ascent and activation of new CCN (Jiang et al. 2000, present modeling results on the effects of CCN entrainment). In a well-mixed boundary layer the vertical profile of temperature and liquid water content are adiabatic regardless of whether parcels exchange mass with their environment. This is because the parcel and environment are identical.

Figure 2 shows an example of temperature, LWC and drop size distribution measurements from a boundary layer cloud observed on 18 May 1998 that is mostly adiabatic and homogeneous. In the example shown in Figure 2, the temperature profile is nearly adiabatic, the profile of LWC measurements from the King probes and PVM are within 20% of adiabatic. (The FSSP LWC is about twice the adiabatic value and is believed to be in error, as discussed in the next section.) The FSSP drop size distribution is monomodal, the profile of mean droplet size increases monotonically with height and the dispersion of the droplet spectrum is constant with height. There was no drizzle detected. All of these factors support the conclusion that this boundary layer cloud observed from 2208 – 2210 UTC by the C-130 on 18 May 1998 was mostly adiabatic.

CPI images provide another method of investigating cloud homogeneity. As seen in Figure 1, when a particle is detected by the PDS and the CPI imaging laser is fired, the imaged volume may contain more than one particle, particularly if the particle concentration is relatively high. In a homogeneous cloud, the effect of sampling random volumes of equal size would result in a Poisson distribution for the number of particles per sample. Figure 3a shows the Poisson distribution for the number of particles per sample with the same mean as that observed by the CPI from 221010 – 221030 UTC during the slant profile shown in Figure 2. Also shown in Figure 3a is the distribution of the number of particles per image frame actually measured by the CPI. The comparison in Figure 3a shows that the CPI measurements closely follow the theoretical Poisson distribution.

A more sensitive test for inhomogeneity can be made by conditional examination of the particle size distributions for the cloud region shown in Figures 3a. One conditional distribution was made of the sizes of particles imaged in CPI image frames with three or less particles, while the other was made from the sizes of particles imaged in frames with five or more particles. If the cloud were homogeneous, the conditional size distributions should be identical. The data in Figure 3b show that the conditional spectra are nearly identical, suggesting that this region of cloud was quite homogeneous.

The measurements shown in Figures 2 and 3 are representative of FIRE.ACE boundary layer clouds with adiabatic LWC profiles. However, even in these cases, there is evidence that some entrainment and mixing is occurring in some regions of the cloud. In Figure 2, clear air holes are seen that extend to at least 100 m below cloud top. The CPI also confirms the lack of cloud in these spots. Presumably, these are entrainment events that bring clear air from above the cloud into the cloud layer. Curry (1986) also observed that cloud top air penetrated downward into the cloud to a depth of at least 50 m.

4.3 Evaluation of LWC Instrumentation in Adiabatic Clouds

In addition to providing an excellent natural outdoor laboratory for studying mixing and evolution of the droplet spectra, these Arctic clouds provide a reliable test bed for assessing the performance of some of the microphysical instrumentation. The LWC profile and temperature are predictable in regions of cloud that have ascended adiabatically from cloud base to the observation level (e.g., Jensen et al. 1985; Lawson and Blyth 1998). The cloud base temperature and pressure were measured at the point where the FSSP droplet concentration exceeded zero on ascents, and when the concentration dropped to zero on descents. A zero FSSP concentration threshold was used because, unlike some environments where there are relatively high concentrations of large aerosols that produce occasional counts, the FSSP almost always read zero in clear air. This method of computing adiabatic LWC is not only the simplest to implement, but arguably the most accurate, because the subsequent analysis depends primarily on relative changes in temperature and pressure. Static pressure measurements on research aircraft are generally felt to be accurate to < 1 mb. In dry air, an absolute uncertainty of about 0.3° C is expected in the Rosemount temperature measurements (Lawson and Cooper 1990). Lawson and Cooper (1990) show that an additional error from sensor wetting of < ~0.5° C is expected when the LWC is < ~0.5 g m^{-3}, as was the case in these clouds. No evidence of temperature spikes, typically found when the Rosemount temperature probe element gets wet (Lawson and Cooper 1990), was observed on cloud exit. For a 1 ° C error in measurement of temperature and a 1 mb error in pressure at cloud base, there is only a 0.025 g m^{-3} maximum error in adiabatic LWC for conditions typical of FIRE.ACE boundary layer clouds. Thus, instrumentation measurement errors in pressure and temperature at cloud base can be expected to have an insignificant contribution to the determination of adiabatic LWC.

Figure 4 shows scatterplots of LWC measurements versus adiabatic LWC for all of the (nine) ascents and descents through clouds that were determined to be close to adiabatic, although as shown in Figure 2, 'holes' were occasionally observed in these clouds. Since there is no reason to expect superadiabatic LWC in these clouds, and since there is evidence of some mixing almost everywhere, the calculated adiabatic value is the maximum that the measurements should reach (except for the contribution from measurement errors). The data in the scatterplots show that both King probes generally did not exceed the adiabatic value and were within 75% of adiabatic LWC (except in regions with obvious 'holes'). The PVM scattered around the adiabatic value and sometimes exceeded it by up to about 35%. The FSSP generally exceeded the adiabatic LWC value by up to a factor of two.

While instrumentation errors were shown to have a negligibly small effect in determination of adiabatic LWC, fluctuations in the actual cloud base level could potentially introduce significant errors in adiabatic LWC. For example, during a

slant ascent or descent through a stratus cloud, the aircraft may enter cloud base at one point, and when it reaches cloud top, the air parcel it samples may have originated at a different cloud base elevation. Significant errors in adiabatic LWC are more likely when there are noticeable undulations in cloud base elevation. Figure 5 shows LWC measurements from one of the nine adiabatic profiles and the effect on LWC for different cloud base elevations. It can be seen that a deviation from the measured value of 1001 mb to about 1013 mb (a difference of about 120 m) would be required to produce an adiabatic LWC that agrees with the peaks in the FSSP measurements. It is very unlikely that variations of this magnitude existed in the actual cloud base elevations in this case, as evidenced by the measurements of FSSP and PVM LWC also shown in Figure 5, when the C-130 exited cloud and flew level just underneath cloud base for about 15 s. If a lower cloud base existed, it would likely have been detected during this horizontal leg. In addition, after exiting cloud, the C-130 flew for about two min just below the cloud base elevation before climbing for another cloud penetration. During this time, there was no indication of lower cloud base, and the cloud base measured upon ascent was within two mb of the previous measurement. The nine slant profiles used to generate the data in Figure 4 where carefully selected, so that errors in determination of cloud base were minimized.

Thus we can conclude that *for C-130 measurements from this field project*: 1) the King probes rarely exceeded the adiabatic value and were usually accurate to within 20%.[1]. 2) The PVM measurements scattered around the adiabatic value, with an occasional apparent tendency to overestimate the adiabatic LWC. 3) The FSSP measurements are heavily biased toward values that exceeded the adiabatic LWC. It is highly unlikely that the FSSP measurements could be the result of underestimates in the adiabatic LWC, since this would mean that the aircraft consistently measured a cloud base that was about 10 mb too high, and that the King and PVM probes consistently underestimated LWC.

The FSSP counts and sizes droplets. Errors in sizing are raised to the third power and can result in significant errors in LWC. The NCAR FSSP was calibrated with glass beads in the field, but even so, sizing errors can occur (Baumgardner et al. 1990). Errors from undercounting in high (> 600 cm^{-3}) drop concentrations are due to coincidence, which also artificially broaden the drop size spectra (Cooper 1988, Brenguier 1989). Coincidence artificially increases LWC because two small drops are erroneously recorded as one larger drop, and since LWC is proportional to the third moment, the undercounting is outweighed by the increase in drop size. However, drop concentrations rarely exceeded 250 cm^{-3}, except perhaps downwind of the effluent plume from the SHEBA ship (For

[1] Shortly after this manuscript was accepted, measurements of the dimensions of the King probe sensor wires used in the FIRE.ACE project showed that the area of the sensor was overstated by about 20%. In the calculation of LWC, sensor area is inversely proportional to LWC, so the FIRE.ACE measurements would increase by about 20%. The NCAR Research Aviation Facility (RAF) plans to publish a correction that can be applied to the archived FIRE.ACE data (K. Laursen 2000 – Personal Communication). The end result will be that the King LWC measurements will be increased by about 20% and be in closer agreement with the PVM values.

information on aerosols during SHEBA see Yum and Hudson 2000 and Pinto et al. 2000), so coincidence errors should not be problematical. Thus, there is currently no explanation for the apparent overestimation of LWC observed in the FSSP measurements.

Regardless of the apparent error in FSSP measurement of LWC, the primary function of the FSSP is to measure drop size distribution. There is currently no determination of how much of the apparent error in FSSP LWC is due to error(s) in sizing and/or concentration. However, FSSP measurements that show comparisons of relative FSSP drop size distributions are still very useful and are included frequently in this paper.

The FSSP displayed the most stable baseline outside of cloud and was the best probe to use to identify cloud boundaries. The baseline of the King probes often varied erratically by up to $\pm$ 0.05 g m^{-3}. The PVM baseline also drifted occasionally, although the drift was slower and did not fluctuate rapidly. Care must be taken to subtract the clear-air offset from both the King and PVM probes. All four probes were inoperative during some flights and/or portions of flights; however, there were two King probes and one or the other probe was operational on every flight.

A qualitative investigation of the effects of ice on measurements of LWC was undertaken by comparing probe responses in a cirrus cloud with all ice particles. Figure 6 shows the responses of the King, PVM and FSSP probes to an all-ice cirrus cloud, along with ice particle concentration and IWC measurements derived from CPI measurements. There are undefined uncertainties in the CPI IWC measurements, however, using the relative responses of the LWC instruments, it can be seen that the FSSP and PVM (optical) probes respond much more to ice than the King (hot-wire) probes. The CPI IWC was dominated in this cirrus cloud by the larger (200 to 400 μm) bullet rosette crystals (shown later in Figure 20). Conversely, the small (< 50 μm) ice particles made up the majority of the CPI concentration measurements. The relative phasing of the PVM and FSSP LWC measurements agree better with the CPI concentration (small particles) than the CPI IWC (larger particles), suggesting that the false LWC signals of the FSSP and PVM probes in an all-ice cloud are affected more by the small particles.

4.3 Non-Adiabatic, Inhomogeneous Clouds

As previously discussed, nine of the 21 slant profiles flown through the nearly all-water boundary layer clouds were found to be mostly adiabatic and homogeneous. Here we discuss microphysical properties of typical examples from the remaining set of 12 clouds, which were non-adiabatic, inhomogeneous and actively mixing.

Figure 7 shows a C-130 slant profile through a boundary layer cloud on 29 July 1998. Both LWC and temperature display a systematic trend to deviate increasing more from adiabatic values with increasing distance above cloud base, which strongly suggests an active mixing process at cloud top (Zhang et al. 2000 present modeling results on cloud top mixing). At cloud top, the temperature fluctuates strongly and is often warmer than adiabatic, due to entrainment of relatively warm air from the temperature inversion above cloud top. The droplet spectra are bimodal at cloud top and drizzle was encountered lower in the cloud. This is in contrast to boundary layer clouds where the LWC and temperature profiles were adiabatic and the drop spectra were monomodal (i.e. Figure 2), where drizzle was not observed anywhere along the profile.

When the LWC and temperature profiles were significantly sub-adiabatic in FIRE.ACE boundary layer clouds, the droplet spectra near cloud top were often bimodal and drizzle was observed lower in the cloud. It was not a necessary condition for the drop spectra to be bimodal to observe drizzle, since in some subadiabatic clouds that were actively mixing, drizzle was occasionally observed at cloud base without concurrent measurements of bimodal drop spectra in the cloud. However, it should be remembered that the aircraft samples a relatively small volume of cloud, and bimodal drop spectra could be present at locations in the cloud not sampled by the aircraft.

Figure 8 shows another profile flown about 7 minutes earlier than the slant profile in the same boundary layer cloud shown in Figure 7. Basically, the same large-scale observation seen in Figure 7, which is that the boundary layer cloud is actively mixing at cloud top, is seen in Figure 8. The profile shown in Figure 8, however, has regions where the C-130 flew several-minutes-long constant altitude legs, providing an opportunity to examine cloud inhomogeneity using the conditional spectra technique introduced in Section 4.2 and shown for a relatively homogeneous cloud region in Figure 3. The presentations of theoretical Poisson and CPI measured number of particles per image frame and the conditional drop size distributions, analogous to those shown in Figure 3, are shown above the time series measurements in Figure 8. The measured number of particles per image frame follow the Poisson distribution and the conditional drop size distributions are nearly identical for the cloud regions at 180 and 270 m msl. This implies that these regions are well-mixed and there is not a large degree of inhomogeneity in the lower and middle levels of this boundary layer cloud. On the other hand, near cloud top at 450 m msl, a larger degree on inhomogeneity can be seen in the temperature and LWC measurements, and this is reflected in the conditional drop size distribution measurements, which are noticeably different. It is interesting to note that the trend in the conditional spectra is for the smaller droplets to be found in locally higher concentrations than the larger droplets. Just the opposite might be expected in an actively mixing cloud.

It is also interesting to note that the drop size distribution is distinctly bimodal in the mid-level region, yet the conditional spectra revealed no inhomogeneity.

This suggests a process whereby the mixtures formed at cloud top (cooled by evaporation) descended toward mid-cloud and continued mixing while descending, which resulted in a relatively well mixed region.

Perhaps the most striking aspect of boundary layer clouds observed during FIRE.ACE, as revealed by this analysis, is how a group of clouds that are fairly similar in visual appearance can exhibit such variability in microphysical properties. In order to investigate further aspects of the FIRE.ACE boundary layer clouds, we generated time series measurements of key microphysical, thermodynamic and dynamic parameters for six cases.

Figures 9 and 10 show time series measurements of LWC, temperature, vertical velocity, FSSP concentration, altitude and the standard deviation for all of these quantities, except for altitude. The data in these figures are organized to show examples of the microphysical variability between these boundary layer clouds. The regions selected for display in Figures 9 and 10 were chosen when the C-130 flew level for several seconds, and at different altitudes in the boundary layer clouds (the only exception being 15 May in Figure 9 when there were no representative level regions). The purpose of selecting these regions was to see if there were any consistently recognizable features that varied as a function of altitude in the boundary layer clouds. Figure 9 shows examples of cloud regions (also shown in Figures 2 and 4) that were mostly adiabatic with relatively constant FSSP drop concentration and temperature measurements. These clouds displayed monomodal droplet spectra and there were no observations of drizzle at the time of the in situ measurements. Figure 10, on the other hand, shows cloud regions where mixing produced sub-adiabatic LWC, variations in the FSSP drop concentration and temperature, and often bimodal droplet spectra and drizzle.

The data in Figure 9 show that there is very little change with altitude in the thermodynamic (i.e., temperature), dynamical (i.e., vertical velocity) and microphysical parameters (i.e., LWC and FSSP concentration) in these all-water clouds. As shown in Figure 3, the droplet spectra were monomodal and no drizzle was observed by the C-130. As previously stated, this is typical of the "mostly adiabatic" boundary layer clouds. The values of standard deviation (σ) in Figure 9 are mostly constant, except for the bumps in drop concentration and LWC (resulting from the 20 s over which σ is computed) around the region where the 'holes' are observed in the 18 May cloud.

Figure 10 shows four examples of profiles in boundary layer clouds that were actively mixing. The data in this figure show that fluctuations in temperature, LWC and FSSP drop concentration tend to increase as the C-130 gets closer to cloud top. This is consistent with the hypothesis put forth previously that these boundary layer clouds are mixing from the cloud top downward. The

measurements in Figure 10 show that there is not an increase in the standard deviation of vertical velocity with height in these boundary layer clouds. The air motion system in the C-130 contains a residual offset that is on the order of 0.5 m s^{-1}, so the small offset in vertical velocity in Figures 9 and 10 should be ignored. However, the small-scale fluctuations are considered to be accurate to within a few tenths m s^{-1}, so the consistent lack of increase in the fluctuation of vertical velocity with height is significant. The boundary layer clouds depicted by the measurements in Figure 10 all had bimodal drop distributions at cloud top and drizzle was observed below cloud.

Generally, in Figures 9 and 10 there was a lack of correlation in vertical velocity with FSSP drop concentration, and there is a correlation between LWC and drop concentration. An exception to the above generalizations is seen in Figure 9 on 18 May, where the drop concentration increases from the nominal level of about 80 cm^{-3} to 140 cm^{-3} in three regions, and the LWC remains fairly steady. In these regions the vertical velocity shows a significant increase. The FSSP mean drop size (not shown) was anti-correlated with drop concentration, which accounts for the lack of increase in LWC, and also agrees with the observation that a localized updraft could have activated more CCN.

The test for inhomogeneity using CPI images, described in Section 4.2 and shown in Figures 3 and 8, was applied to the region in Figure 9 on 18 May where there is a subtle, but noticeable variation in drop concentration. Figure 11 shows the results in the same format as Figure 3. which is from the same cloud profile as shown in Figure 11, but about 50 s later when there was no obvious variation in droplet concentration. The conditional spectra in Figure 11 are slightly separate, suggesting that the region has a detectable inhomogeneity. The results of the inhomogeneity test using CPI image data shown in Figures 3 and 11 demonstrate the sensitivity of this type of test, but do not provide information on the scale of the inhomogeneity. However, in this case, the large scale structure that can be seen in the time series measurements of Figure 9, likely caused the separation seen in Figure 11. The tendency for smaller droplets to be observed in higher concentration regions is consistent with the time-series measurements.

4.4 Mixed Phase Cloud

Figure 12 shows an example of time-series measurements from a boundary layer cloud that is fairly unique in the C-130 FIRE.ACE data set. This was a case where cloud base was higher (640 m MSL) than the clouds previously discussed and the entire sub-cloud layer was well-mixed to the surface (see Figure 12). This was the first C-130 mission (4 May), the atmosphere was still transitioning from the winter regime, and with the higher cloud base, this boundary layer cloud was colder than the other cases discussed. The trends in the measurements in Figure 12 differ from Figures 9 and 10 in that the standard

deviation in vertical velocity is noticeably larger lower in the cloud, and LWC is less near cloud top than near cloud base. Even though the LWC measurements are significantly less than adiabatic everywhere in this cloud, there is no evidence of active mixing near cloud top and the drop spectrum (not shown) at cloud top is monomodal.

The most striking feature of the boundary layer cloud observed on 4 May is the inhomogeneity in the hydrometeor fields. Figure 13 shows a portion of the flight track when the C-130 was descending and making passes over the SHEBA ship, from cloud top (1025 m) down to cloud base (690 m) and examples of CPI images, water drop and ice particle size distributions during this time period. The data in the figure show that the hydrometeor fields varied considerably over spatial distances of 10 Km horizontally and a few hundred meters vertically. When the C-130 skimmed cloud top and then turned and made a pass 30 m below top, it encountered mostly supercooled (-25.5 to –22° C) cloud droplets with a mono-modal size distribution and only a few 100 – 500 μm ice particles. The larger ice particles may have fallen from a higher cloud. The ratio of water drop to ice particle concentration is > 1000:1, so the region near cloud top was predominately composed of supercooled cloud droplets with a monomodal size distribution.

On the next pass 75 m below cloud top, Figure 13 shows that the CPI water drop concentration had decreased by about a factor of six, and the size distribution still had a mode of about 30 μm, but had also broadened slightly. Some ice particles were observed, mostly unrimed with sizes to about 300 μm, and an occasional rimed particle as large as 600 μm. However, just west of this position and 30 m lower (920 mb), while the C-130 was turning to reverse course, a section of drizzle about 10 km in horizontal dimension was observed with supercooled (-25° C) drops with sizes up to 180 μm. After the pocket of drizzle was transected, the C-130 made another pass over the ship while descending to 900 m and encountered supercooled drops with a mode of about 30 μm and ice particles that were mostly < 500 μm, with a few larger rimed particles. But then, when the C-130 reversed course and two minutes later flew only 30 m lower (870 m) over the same flight track, significantly higher concentrations of rimed ice particles from 400 – 800 μm and occasional graupel particles up to 1 mm were observed.

The degree of inhomogeneity in cloud microphysics could possibly be due to mixing downward from cloud top or from the effects of seeding from higher clouds. Even though significant concentrations of ice particles were not observed during the passes over cloud top, the potential for temporal and spatial variability of this type of seeding precludes eliminating this possibility. The presence of the small pocket of drizzle at -25° C, however, cannot be directly explained by either surface or elevated effects. Curry (1986) reported drizzle when there was a relatively large dispersion in the drop spectra. In this case the FSSP drop spectra at cloud top were relatively narrow and mono-modal, in

contrast to the example shown in Figure 7, where the drop spectra were bimodal and drizzle was observed at -1° C. However, the C-130 could not completely investigate cloud top, so that bimodal drop spectra may have existed somewhere at cloud top. The cloud on 4 May existed for a long time and seeding from above was sporadic. The curious pocket of drizzle that was produced by coalescence may have been an older region that was not seeded from above.

5.0 Deep Stratus Cloud with Very High Ice Particle Concentrations

Next, we examine inhomogeneity in microphysical measurements collected in a deep Arctic stratus cloud. This is not a boundary layer cloud according to the definition used in this paper. The cloud extended from about 2 Km to 6 Km msl (+2 to –23 ° C) on 18 July 1998 and contained a myriad of microphysical characteristics. Figure 14 shows a vertical profile of King LWC, FSSP, 260X and 2D-C (shadow-or) particle concentration measurements, along with water and ice particle size distributions. Representative examples of CPI images of the particles are also shown.

The data from the microphysical measurements shown in Figure 14 will be discussed from cloud top down to cloud base. In the upper portion of cloud, from cloud top at -23° C to –13 ° C, the FSSP droplet concentration varies from about 50 to 250 cm^{-3}, averaging about 125 cm^{-3}, and the LWC ranges from zero to 0.18 g m^{-3}, averaging about 0.1 g m^{-3}. The FSSP drop size distributions shown in Figure 14 are relatively constant in this region, but not especially broad, with 20 μm drops found in concentrations >1 cm^{-3} only in the regions with LWC > ~0.1 g m^{-3}. However, CPI images show a relatively low concentration of drizzle drops up to 125 μm in diameter near –19 ° C. The 260X measured a maximum of ~40 L^{-1} and the 2D-C shadow-or registered a maximum of 1 L^{-1}. This appears to be an example of "non-classical freezing drizzle" formation (Cober et al. 1996; Lawson et al. 1998), where drizzle is formed through coalescence of supercooled drops, usually near the tops of stratus layers. However, in the Cober et al. and Lawson et al. measurements, the FSSP drop spectra were generally broader and the 2D-C concentrations were significantly higher, in excess of 500 L^{-1}.

The CPI images show that ice particles were very rare in the region from -23° C to –13 ° C, and were mostly large (750 μm) heavily rimed particles. The average 2D-C and 2D-P shadow-or particle concentrations are < 0.1 L^{-1} and support the observation that there was negligible ice in the layer. The lack of ice in the region from -23° C to –13 ° C is a curious aspect of this deep stratus cloud, because as will be shown, ice concentrations in the warmer regions below were much higher.

Near –12 ° C there is a noticeable drop in LWC to about <~0.01 g m^{-3}, a reduction in FSSP total particle concentration to about 5 cm^{-3} and a corresponding peak in 260X and 2D-C concentrations. Figure 14 shows CPI images of some examples of the crystals and Table 3 gives a breakdown of a

visual classification of the particles. Figure 14 and Table 3 show that there is a mixture of irregular crystals with abundant sideplane growth, heavily rimed crystals/graupel and small (< 50 μm) spheroidal[2] ice particles. The CPI particle size distributions in Figure 14 show that ice existed in concentrations of about 2500 L^{-1} in the region around –12 ° C. Figure 15 shows the FSSP/CPI/260X combined particle size distribution in the 'central' region with high ice concentrations, and at the 'edges' of this region (i.e., immediately above and below as viewed in the C-130 slant ascent) where the ice concentration is reduced to about 750 L^{-1} and the FSSP concentration increases to about 100 cm^{-3}.

The microphysical data in Figures 14, 15 and Table 3 indicates that the region of high ice concentration is composed of ice particles whose population is dominated by small (< 50 μm) ice spheroids that are not round, but can also not be identified as vapor-grown crystals. They could be frozen drops, or drops that were once frozen to larger ice particles, or even fragments of larger ice particles. The larger ice particles are mostly irregular in shape and often contain side plane growth. In the 'adjacent' regions immediately outside of the area with high ice particle concentrations, the FSSP water drop concentration is much higher (up to 100 cm^{-3} compared with 5 cm^{-3}). The most striking feature in the 'adjacent' regions is that there are more large, heavily rimed crystals, much more of the overall population of crystals is rimed and there are fewer small spheroids compared to the 'central' region.

In the region from about –11 ° C to – 7 ° C the LWC fluctuates between zero and 0.05 g m^{-3} and the FSSP droplet concentration ranges from 50 to 100 cm^{-3}. CPI images show low concentrations of rimed ice particles up to 500 μm and occasional drizzle drops in excess of 100 μm. The activity on the 260X and 2D-C are also relatively low, indicating few particles larger than 40 to 50 μm.

Very high concentrations (~4,000 L^{-1}) of ice particles were also observed In the region from about –3.3° C to –5.5° C. This is a region that is often associated with the Hallett-Mossop (H-M) rime-splintering ice multiplication process. The conditions for H-M ice multiplication are (Hallett and Mossop 1974; Mossop and Hallet (1974); Mossop 1985):

i.) cloud temperatures between -2.5 and -8° C,
ii.) droplets ≥ 23 μm in concentrations > 1 cm^{-3},
iii.) relatively fast-falling (>0.2 to 5 m s^{-1}) ice particles,

The FSSP total particle concentration ranges from 2 to 20 cm^{-3} and averages about 5 cm^{-3} in the region with high ice concentration near –4.5 ° C. Figure 16 shows particle size distributions and CPI images in a format similar to that shown

[2] Here, spheroidal refers to image shapes that are not spherical (i.e., perfectly round), but instead, have a slight but noticeable departure from a perfectly spherical shape.

in Figure 15 and Table 4 shows a classification of ice particles in a format like Table 3. The conditions for H-M ice multiplication are met in the central region if one assumes that the FSSP is only responding to water drops. However, as shown from the CPI data in Table 4 and Figure 16, the large majority of particles with sizes greater than about 25 μm are actually ice, so that the H-M criteria for drops > 23 μm in concentrations exceeding 1 cm^{-3} is not actually satisfied in the central region.

The Rosemount icing detector did not register any supercooled water in the regions with high ice particle concentrations at -12 ° C and – 4.5 ° C, which strongly suggests that these regions were nearly glaciated. Mazin et al. (2000) have show that the theoretical sensitivity of the Rosemount icing detector is about 0.005 g m^{-3} under these thermodynamic conditions, so supercooled liquid water in excess of this threshold would be observed by the probe. The King probe (Figure 14) does indicate a small amount (0.02 to 0.05 g m^{-3}) of liquid water. This is explained as a "false LWC signal" due to ice particles striking and melting on the wire. Cober et al. (2000) have shown that under these thermodynamic conditions, hot-wire probes will register a false LWC signal that is about 15 to 20% of the equivalent ice mass content.

The H-M conditions *do* appear to be satisfied in the regions adjacent to the central region with high concentrations near – 4.5 ° C. The ice concentrations in these regions are still above those expected from primary nucleation, but are about 25% of the ice concentration in the central region.

The mechanism(s) that is producing the very high ice particle concentrations in the regions near –12 ° C and – 4 ° C is not obvious. Rangno and Hobbs (2000) (hereafter R-H) also report ice concentrations in a FIRE.ACE stratus cloud that exceed those expected from primary nucleation, such as the ice nuclei concentrations collected in FIRE.ACE by Rogers et al. (2000). However, R-H did not use CPI data to separate the contributions of water drops and ice, and then measure the total ice particle concentration. Instead, they used 2D-C measurements to determine the total ice particle concentration, which from Figure 14, can be seen to be a conservative (i.e., underestimate) of the actual concentration of ice. R-H did use CPI data to visually classify the types of ice particles in a format similar to Tables 3 and 4. While this type of manual classification is somewhat subjective, it is interesting to note that both analyzes reveal a very high concentration of small ice spheroids (that R-H labeled frozen drops) and particles that were fragments or irregular shapes. The percentage of frozen drops, fragments and irregulars from the R-H analysis totaled 57% of the total ice particle population, and in this study they totaled 97% and 85% in the regions near –12 ° C and – 4 ° C, respectively. R-H point out that if the high ice concentrations were due to the H-M ice multiplication mechanism, the H-M small splinters would grow by vapor diffusion into crystals with identifiable habits, and in their case and here, this does not appear to be the dominate process. R-H also discuss in detail other possible ice multiplication mechanisms involving

shattering of isolated drops during freezing and fragmentation of ice crystals by collisions. They conclude that either mechanism may have been operating, but seemed to slightly favor the fragmentation process, since it appeared to better fit the observations.

Nearly all of the larger ice particles in the 'adjacent' regions are heavily rimed. The individual drops frozen onto these large particles (Figures 15 and 16) that could be susceptible to breaking off. It is also interesting to note that the small spheroids in the 'central' regions look as if they could be fragments that have broken from the large rimed crystals. There is no established physical mechanism to support this hypothesis, however, a similar process of rime breakup has been suggested by Vali (1980).

There is a thin layer of supercooled cloud from –2 ° C to about 0° C that has the highest (0.22 g m^{-3}) LWC and the highest (280 cm^{-3}) FSSP droplet concentration observed anywhere in the cloud. Also, the CPI detected no ice particles in this region and the 260X and 2D-C concentrations were near zero, suggesting that this was a cloud composed of small water drops. It is difficult to explain why the large particles observed above in the cloud are not seen falling through this region of supercooled cloud. This is especially difficult to explain because drizzle was observed below the freezing level, presumably the result of melting of the larger ice particles. However, since the C-130 is climbing at a shallow angle, so that the data shown in Figure 14 do not actually comprise a vertical profile, it is possible that extreme variability in horizontal structure in the cloud (such as seen in Figure 13) can explain this observation.

6. Cirrus Cloud with Highly Inhomogeneous Particle Distribution

Here we focus on the extreme spatial variability ("clumpiness") seen in a cirrus cloud. Figure 17 shows a combined particle size distribution using FSSP, CPI and 260X data as the aircraft flew through cirrus cloud at 5400 m (-25 ° C) for approximately 25 minutes on 29 July 1998. The Rosemount icing detector showed that there was no supercooled liquid water present in this cloud, so all of the particles are assumed to be of ice. The CPI particle size distribution was scaled to the 260X data in the 150 to 500 μm size region, where the 260X measurements are felt to be most reliable. The three particle size distributions show relatively good agreement in the regions where they overlap. A time series of average concentrations measured by the FSSP, CPI and 260X are shown in Figure 18. In Figure 18, the CPI 'scaled total strobes' particle concentration measurements have been scaled to the CPI total particle concentration computed from the composite size distribution in Figure 17. The time-series measurements show that there is considerable spatial structure to the cloud on scales greater than the 120 m resolution of the instruments.

The FSSP is considered here to be a reliable measurement of the average concentration of small particles in cirrus clouds. Previous reports in the literature

(e.g., Gardiner and Hallett 1985) suggest that the FSSP is unreliable in the presence of ice. However, these measurements were in mixed-phase clouds where contributions from ice particles and water drops were difficult to separate. More recently, the literature contains FSSP measurements that are felt to be mostly reliable when the probe is measuring small ice particles in cirrus (e.g., Gayet et al. 1996; Poellot et al. 1999; Arnott et al. 2000). The reasoning for using the FSSP data as a measure of average ice particle concentration cirrus follows:

i.) CPI imagery shows that small (< 40 μm) particles in cirrus are largely spheroidal in shape, so even though the probe may not size these particles as accurately as it does water drops, it will still record a signal from the forward diffraction peak that will be registered as a count.

ii.) The FSSP-100 has a 6 μs dead time, so particles traveling at the (~120 m s^{-1}) airspeed of the C-130 in cirrus must be > ~750 μm to produce a double count. In addition, Figure 17 shows that the number of particles larger than 750 μm is four orders of magnitude less than the contribution of the smaller particles, so even if there were double counts from the large particles, they would have a negligible contribution.

The time-series measurements from the FSSP, CPI and 260X agree very well in phase (i.e., the peaks and valleys line up well). The concentrations measured by the FSSP are about 30% greater than those measured by the CPI, and both the FSSP and CPI are more than an order of magnitude greater than the 260X concentrations. This is largely because, as shown in Figure 17, both the FSSP and CPI data show large numbers of small particles, and high concentrations of small particles are more effectively counted by the FSSP and CPI. The first useable channel in the 260X started at 40 μm, compared with 3 μm for the FSSP, while the smallest resolvable CPI image is about 10 μm.

We now return to the discussion of the highly inhomogeneous particle distribution, or "clumpiness", in this cirrus cloud, which is independent of the absolute magnitudes of the average particle concentrations shown in Figure 18. Figure 19a shows the distribution of the number of particles per CPI image frame and the Poisson distribution with the same mean. As explained in the text describing Figure 3, the Poisson distribution would be the result of random sampling in a homogeneous cloud; the comparison in Figure 19a shows that the cloud is inhomogeneous.

We now show that small particles are found in clumps with very high local concentrations that are interspersed with regions of larger particles in low concentrations. The conditional size distributions (analogous to Figure 3b and 11) are shown in 17b. One conditional distribution was made of the sizes of particles imaged in frames with only one particle, while the other was made from the sizes of particles imaged in frames with seven or more particles. If the cloud were homogeneous, the conditional size distributions would be identical.

However, as seen in Figure 19b, the high concentration frames contain only small particles. That is, the large particles are most often found in concentrations so low that to capture more than one particle in a frame is rare. When there are more than five particles in an image frame, the local concentration is on the order of 100,000 L^{-1} and higher. The small particles can be found at low concentration and at extremely high concentration. The conditional size distributions shown in Figure 19b could result from the aircraft flying first through a region of large particles in low concentration, followed by a region of small particles in high concentrations, similar to the large scale structure that caused the conditional spectra to separate in Figure 11. However inspection of the CPI image frames themselves, shown in Figure 20, reveals that the regions of high concentrations of small particles are interspersed with regions of low concentrations of large particles, mostly bullet rosettes, on scales down to tens of meters and perhaps smaller. Baker et al. (2000) also observed regions with clumps of small particles separated by regions with single rosettes and aggregates of rosettes in a mid-latitude cirrus cloud.

6. Summary

This research investigated microphysical data collected by the NCAR C-130 during the FIRE.ACE field experiment conducted over the Beaufort Sea in May and July, 1998. The standard microphysical measurements in the NCAR C-130 were supplemented, for the first time, with data collected by the cloud particle imager (CPI). CPI data were used to separate spherical images (i.e., water drops) from non-spherical images (ice particles) in mixed-phase clouds. The CPI images also provide a method for determining inhomogeneity in the cloud drop field. CPI data were combined with conventional PMS FSSP, 260X and 2D-C data to determine total particle concentration, and the phase discriminating capability of the CPI was used to determine the water and ice particle size distributions.

A major focus of this investigation concentrated on the microphysical properties of Arctic boundary layer clouds, which were observed on 11 of the total of 16 missions flown by the C-130. Here, we define boundary layer clouds in the sense previously described by Curry et al. (1988), where the clouds are essentially low-lying stratus clouds that may or may not be thermodynamically connected with the surface. These boundary layer clouds were found to vary considerably, both from day to day and within the clouds themselves. The main microphysical features of the boundary layer clouds, based on data collected by the C-130, can summarized as follows:

- From data collected during the 16 aircraft missions and the definition used here to define the presence of boundary layer cloud (i.e., thermally mixed to the surface and/or within 300 m of the surface), 11 of the 16 days had boundary layer clouds. In May, six out of eight cases had boundary layer clouds and all six clouds were mixed from the surface to

cloud base. The depths of the mixing layers in May ranged from 150 to 1200 m. In July, five of the eight cases had boundary layer clouds, but none of these were mixed from the surface to cloud base. Thus, based on these (limited) data, low-lying clouds in the Arctic, which have been shown to strongly influence the melt of the Arctic Ocean ice pack (Curry et al. 1993), were prevalent and displayed significantly different subcloud mixing characteristics in May and July.

- Based on analysis of data from 21 vertical (slant) profiles flown on four days in essentially all-water clouds, nine of the profiles revealed mostly homogeneous, adiabatic conditions with monomodal drop size distributions and no drizzle drops. Data from the remaining 12 profiles indicate that these clouds were either too thin to have adequate LWC to determine whether they were adiabatic, or that they were actively mixing from cloud top downward. In the latter cases, the LWC and temperature in the upper portion of cloud were generally non-adiabatic and the clouds were inhomogeneous. The drop size distributions were often bimodal near cloud top and drizzle was sometimes observed.

- The adiabatic regions of clouds were used to evaluate the performance of the LWC probes, although the adiabatic LWC never exceeded 0.4 g m^{-3} in these thin clouds, so the instruments were only evaluated within a relatively low range of LWC. The two King probes generally did not exceed the adiabatic value and were within 75% of adiabatic. The Gerber PVM probe scattered around the adiabatic value and sometimes exceeded it by up to about 35%. The FSSP systematically exceeded the adiabatic LWC value by up to a factor of two.

- A mixed-phase boundary layer cloud investigated on 4 May 1998 that was 360 m thick and ranged in temperature from –22 to –25 ° C displayed considerable variation in hydrometeor fields. Based on CPI measurements, regions about 10 Km across and separated by only 100 m in the vertical contained either small cloud drops and few ice particles, drizzle, or graupel particles. Seeding from cirrus clouds aloft likely influenced the microphysical processes in this cloud.

In addition to the study of boundary layer clouds, a deep stratus cloud with cloud base at 2 Km (+2 ° C) and cloud top at 6 Km (-23 ° C) was studied. Examination of the microphysics in this deep stratus cloud revealed extreme variability in cloud particles and two layers with exceptionally high (2,500 to 4,000 $L^{-1)}$ concentrations of small ice particles.

Starting the description of the stratus cloud from the top down, a region of supercooled drizzle (at –19 ° C) was observed near cloud top, and supercooled cloud drops with very low (~0.1 L^{-1}) ice concentrations were observed from cloud top to the –13 ° C level. In a thin layer around –12 ° C, very high (~ 2500 L^{-1}) ice

concentrations were observed, with about 97% of the ice identified as small (< ~ 50 μm) spheroidal (but not perfectly round) particles, fragments and irregular shapes. Only 2% of the ice appeared to be vapor grown. Relatively low ice concentrations and small amounts of supercooled liquid water were observed between –11 ° C and –7 ° C. From –5.5 ° C to –3.3 ° C, another layer with very high (4000 L^{-1}) ice particle concentrations was observed. Although this layer was within the temperature regime where the Hallett-Mossop ice multiplication process is often observed, there were insufficient drops > 23 μm to meet the Hallett-Mossop criteria. Instead, the FSSP appeared to be responding to the small ice spheroids observed by the CPI, since the Rosemount icing detector did not measure any supercooled liquid water. The ice particles in this region were similar to those observed at –12 ° C, with the main difference being more columns and fewer crystals with side-plane growth. Small, spheroidal (but not perfectly round) ice particles, fragments and other irregular ice particles accounted for 85% of the total ice particle concentration. This is in general agreement with observations by Rangno and Hobbs (2000) in another FIRE.ACE stratus cloud, where they analyzed CPI images and found that 57% of the ice particles were "frozen drops" (presumably similar to our small spheroids), fragments and particles with irregular shapes. Rime breakup, fragmentation from crystal collision, and drop shattering are discussed as possible ice multiplication mechanisms, but there is no physical way to adequately verify any of these processes. Drizzle was observed precipitating through cloud base of this deep stratus cloud.

An Arctic cirrus cloud was also investigated and shown to be highly inhomogeneous on scales down to tens of meters or less. Regions with high concentrations of small ice particles are interspersed with regions of low concentrations of large particles, mostly bullet rosettes. The CPI images showed that the regions with small ice particles were in very high (~100,000 L^{-1}) local concentrations, although the average concentration in the cirrus measured by the CPI and FSSP probes was on the order of several hundreds per liter.

The variability in the microphysical properties of Arctic stratus (boundary layer, deep stratus and cirrus) clouds, both within a cloud and from cloud to cloud, presents a challenge for Arctic column and process modelers alike. The variability of hydrometeor types and concentrations within Arctic stratus clouds also presents a challenge to investigators retrieving microphysical properties from remote measurements. While presenting these challenges, Arctic stratus clouds also offer the benefit of being relatively easy to study with large turboprop and jet aircraft in the summer months, in that they are persistent and cover extensive areas.

Acknowledgments: We would like to thank Dr. Judith Curry for her insightful comments. We are also indebted to the NCAR Research Aviation Staff for their scientific and instrumentation support, and to the crew of the C-130 for their

skillful piloting and maintenance of the aircraft. This work has been funded under the NASA FIRE program, Contract No. NAS1-96015.

References

Arnott, P. A., D. Mitchell, C. G. Schmitt, D. Kingsmill, and D. Ivanova, Analysis of the FSSP performance for measurements of small crystal spectra in cirrus. Proceedings: 13th International Conference on Clouds and Precipitation, Reno, NV., 14 - 18 August, 2000, 191 – 193, 2000.

Baker, B. A., R. P. Lawson, and C. G. Schmitt, Clumpy Cirrus. Proceedings: 13th International Conference on Clouds and Precipitation, Reno, NV., 14 - 18 August, 2000, 637 – 640, 2000.

Baumgardner, D., An analysis and comparison of five water droplet measuring instruments, *J. Appl. Meteor.*, 22, 891-910, 1983.

Baumgardner, D., W. Strapp, and J. E. Dye, Evaluation of the forward scattering spectrometer probe: Part II. Corrections for coincidence and dead-time losses, *J. Atmos. Oceanic Technol.*, 2, 626-632, 1985.

Baumgardner, D., Corrections for the response times of particle measuring probes, *Sixth Symp. Meterol. Obs. and Instruments*, New Orleans, *Am. Meteorol. Soc.*, pp. 148-151, 1987.

Baumgardner, D., and M. Spowart, Evaluation of the forward scattering spectrometer probe. Part III: Time response and laser inhomogeneity limitations, *J. Atmos. Oceanic Tech.*, 7, 666-672, 1990.

Baumgardner, D., W. A. Cooper, and J. E. Dye, Optical and electronic limitations of the forward-scattering spectrometer probe, *Limited Particle Size Measurements Techniques: 2nd Volume ASTM STP 1083,* 115-127, 1990.

Biter, C. J., J. E. Dye, D. Huffman and W.D. King, The drop-size response of the CSIRO liquid water content probe. *J. Atmos. Oceanic Technol., 4*, 359-367, 1987.

Brenguier, J-L., Coincidence and dead-time corrections for particle counters. Part II: High concentration measurements with an FSSP, *J. Atmos. Oceanic Technol., 6*, 585-598, 1989.

Cerni, T. A., Determination of the size and concentration of cloud drops with an FSSP, *J. Clim. & Appl. Meteorol.*, 22, 1346-1355, 1983.

Cober, S.G., J.W. Strapp and G.A. Isaac, An example of supercooled drizzle drops formed through a collision-coalescence process. *J. Appl. Meteor.*, **35**, 2250-2260. 1996.

Cober, S.G., G.A. Isaac, Korolev, A. V., and J. W. Strapp, Assessing the relative contributions of liquid and ice phases in winter clouds. Proceedings: 13th International Conference on Clouds and Precipitation, Reno, NV., 14 - 18 August, 2000, 689 – 692, 2000.

Cooper, W. A., Effects of coincidence on measurements with a forward scattering spectrometer probe, *J. Oceanic Atmos. Tech., 5*, 823-832, 1988.

Curry, J.A., Interactions among turbulence, Radiation and microphysics in Arctic stratus clouds, *J. Atmos. Sci., 43*, 90-106, 1986.

Curry, J. A., E. E. Ebert and G. F. Herman, Mean and turbulence structure of the summertime Arctic cloudy boundary layer. *Q. J. R. Meteorol. Soc.* 114, 715-746, 1988.

Curry, J.A., F.G. Meyer, L.F. Radke, C.A. Brock and E.E. Ebert, Occurrence and characteristics of lower tropospheric ice crystal in the Arctic, *Int. J. Climatol.*, 10, 749-764, 1990.

Curry, J.A., E.E. Ebert and J.L. Schramm, Impact of clouds on the surface radiation balance of the Arctic Ocean, *Meteor. Atmos. Phys., 51*, 197-217, 1993.

Curry, J.A., W.B. Rossow, D.A. Randall and J.L. Schramm, Overview of Arctic Cloud and Radiation Characteristics, *J. of Climate*, *9*, 1731-1764, 1996.

Curry, J.A., J.O. Pinto, T. Benner and M. Tschudi, Evolution of the cloud boundary layer during the autumnal freezing of the Beaufort Sea, *J. Geophys. Res., 102,* 13851 - 13860, 1997.

Curry, J.A., P. Hobbs, M. King, D. Randall, P. Minnis, et al., FIRE Arctic Clouds Experiment, *Bull. Amer. Meteorol. Soc.*, **81**, 5-29, 2000.

Dye, J.E. and D. Baumgardner, Evaluation of the forward scattering spectrometer probe: Part I. Electronic and optical studies, *J. Atmos. Oceanic Technol. 1*, 329-344, 1984.

Gardiner, B.A. and J. Hallett, Degradation of in-cloud forward scattering spectrometer probe measurements in the presence of ice crystals. *J. Atmos. Ocean. Tech.*, 171-180, 1985.

Garrett, T. and P.V. Hobbs, Calibration of liquid water probes from the University of Washington's CV-580 aircraft at the Canadian NRC wind tunnel, *Rep. Cloud and Aerosol Research Group*, 20pp., Dept. of Atmospheric Sciences, Univ. of Washington, Seattle, WA, 1999.

Gayet, J., G. Febvre and H. Larsen, The reliability of the PMS FSSP in the presence of small ice crystals. *J. Atmos. Oceanic Technol.*, **13**, 1300-1310, 1996.

Gerber, H., B.G. Arends, and A.S. Ackerman, New microphysics sensor for aircraft use, *Atmos. Res.*, *31*, 235-252, 1994.

Hallett, J., and S.C. Mossop, Production of secondary ice particles during the riming process. Nature, 249, 26-28. 1974.

IPCC, *Climate Change: The IPCC Scientific Assessment*, edited by J.T. Houghton, G.J. Jenkins and J.J. Ephramus, 365 pp., Cambridge University Press, 1990.

Jayaweera, K.O.L.F. and T. Ohtake, Concentration of ice crystals in Arctic stratus clouds, *J. Rech. Atmos.*, 7, 199-207, 1973.

Jensen, J. B., P. H. Austin, M. B. Baker and A. M. Blyth, Turbulent mixing, spectral evolution and dynamics in a warm cumulus cloud, *J. Atmos. Sci., 42*, 173-192, 1985

Jiang, H., G. Feingold, W. R. Cotton and P. G. Duynkerke, Large-Eddy Simulations of Entrainment of Cloud Condensation Nuclei into the Arctic Boundary Layer: 18 May 1998 FIRE/SHEBA Case Study, 2000 (This issue).

King, W. D., D. A. Parkin and R. J. Handsworth, A hot wire liquid water device having fully calculable response characteristics, *J. Appl. Meteor., 17*, 1809-1813, 1978.

Knollenberg, R.G., Techniques for probing cloud microstructure, *Clouds Their Formation, Optical Properties, and Effects,* edited by P.V. Hobbs and A. Deepak, Academic Press, New York, NY. 15-91, 1981.

Korolev, A.V., J.W. Strapp and G.A. Isaac, Evaluation of the Accuracy of PMS Optical Array Probes. *J. Atmos. Oceanic Technol.*, **15**, 708-720, 1998.

Korolev, A.V., G.A. Isaac and J. Hallett, Ice particle habits in Arctic clouds, *Geophys. Res. Letters*, *26*, 9, 1299-1302, 1999.

Laursen, K., Project documentation summary, Surface Heat Budget of the Arctic Ocean, NCAR RAF Project No. 8-101, 1998

Lawson, R. P. and W. A. Cooper, Performance of some airborne thermometers in clouds, *J. Atmos. Oceanic Technol., 7*, 480-494, 1990.

Lawson, R. P. and R. H. Cormack, Theoretical design and preliminary tests of two new particle spectrometers for cloud microphysics research. Atmos. Res., 35, 315-348. 1995.

Lawson, R. P., Improved particle measurements in mixed phase clouds and implications on climate modeling, *Proceedings: WMO Workshop on Measurement of Cloud Properties for Forecasts of Weather, Air Quality and Climate*, 23-27 June, Mexico City, pp. 139-158, 1997.

Lawson, R. P. and A. M. Blyth, A comparison of optical measurements of liquid water content and drop size distribution in adiabatic regions of Florida cumuli, *Atmos. Res., 47-48*, 671-690, 1998.

Lawson, R.P. and T.L. Jensen, Improved microphysical observations in mixed phase clouds, *Presented at the American Meteorological Society Conference on Cloud Physics*, 17-22 August, Everett, Washington, pp. 451-454, 1998.

Lawson, R. P, A. V. Korolev, S. G. Cober, T. Huang, J. W. Strapp and G.A. Isaac, Improved Measurements of the Drop Size Distribution of a Freezing Drizzle Event, *Atmos. Res., 47-48*, 181-191, 1998.

Mazin, I. P, A. V. Korolev, A. Heymsfield, G. A. Isaac, and S. G. Cober, Thermodynamics of icing cylinder for measurements of liquid water content in supercooled clouds. *J. Atmos. Oceanic. Technol.*, 2000 (in press).

Mossop, S. C., Secondary ice particle production during rime growth: The effect of drop size distribution and rimer velocity, *Q. J. R. Meteorol. Soc., **111***, 1113-1124, 1985.

Mossop, S. C., and J. Hallett, J., Ice crystal concentration in cumulus clouds: Influence of the drop spectrum, *Science, **186**,* 632-633, 1974.

Perovich, D.K., E.L. Andreas, J.A. Curry, H. Eiken, C.W. Fairall, T.C. Grenfell, P.S. Guest, J. Intrieri, D. Kadko, R.W. Lindsay, M.G. McPhee, J. Morrison, R.E. Moritz, C.A. Paulson, W.S. Pegau, P.O.G. Persson, R. Pinkel, J.A. Richter-Menge, T. Stanton, H. Stern, M. Sturm, W.B. Tucker III and T. Uttal, Year in ice gives climate insights, *EOS, 80 (41)*, 484-486, 1999.

Pinto, J. O., J. A. Curry, and J. M. Intrieri, Cloud-aerosol interactions during autumn over the Beaufort Sea, 2000 (This Issue).

Poellot, M.R., W.P. Arnott and J. Hallett, In Situ Observations of Contrail Microphysics and Implications for Their Radiative Impact. *J. Geophys. Res.*, **104**, (D10), 12,077-12,084, 1999.

Pruppacher, H. R. and J. D. Klett, *Microphysics of Clouds and Precipitation,* 707pp., D. Reidel Publishing Company, 1978.

Rangno, A. L. and P. V. Hobbs, Ice particles in stratiform clouds in the Arctic and possible mechanisms for the production of high ice concentrations, 2000 (This issue).

Rogers, D. C., P. J. DeMott and S. M. Kreidenweis, Measurements of Ice Nucleating Aerosol Particles in the Arctic, 2000 (This issue).

Vali, G., Ice multiplication by rime breakup. Communications a la VIIIeme conference internationale sur la physique des nuages. Clermont-Ferrand, France, Volume I, 227-228, 1980.

Wendisch, M., A. Keil, and A.V. Korolev, FSSP characterization with monodisperse water droplets, *J. Atmos. Oceanic Technol.*, *13*, *6*, 1152-1165, 1996.

Wendisch, M. A, quantitative comparison of ground-based FSSP and PVM measurements. *J. Atmos. Oceanic Technol., 15*, 887 – 900, 1998.

Witte, H.J., Airborne observations of cloud particles and infrared flux density in the Arctic, MS Thesis, Dept. of Atmospheric Sciences, 102 pp., Univ. of Washington, Seattle, 1968.

Yum, Seong Soo, and James G. Hudson, Vertical distributions of cloud condensation nuclei spectra over the springtime Arctic Ocean, 2000 (This Issue).

Zhang, Q., S. Krueger, Qiang Fu and Qing Wang, Large-Eddy Simulation of An Arctic Stable Cloudy Boundary Layer, 2000 (This issue).

Figure Captions

FIGURE 1: Diagram showing the fundamental design of the CPI. See text for explanation of operation.

FIGURE 2: The temperature and altitude recorded by the C-130 on 18 May 1998 as it sampled a boundary layer cloud as well as the calculated adiabatic temperature are shown in the top panel. FSSP size distributions for different time periods are shown in the middle. A time series of LWC recorded by several different probes is compared to the calculated adiabatic value in the bottom panel. The FSSP Mean Droplet Diameter and Dispersion are plotted versus altitude on the right.

FIGURE 3: Histograms of the number of particles per frame for all the CPI imaged frames during the time period 22:09:45 – 22:09:85 shown in Figure 2 along with the Poisson distribution with the same mean, and (bottom) conditional particle size distributions produced by using only those particles in frames with 5 or more particles (black) and by using those particles in frames with 3 or less particles per frame (gray).

FIGURE 4: A scatter plot of measured Liquid Water Contents (for four instruments) taken during nine different slant profiles plotted against the calculated adiabatic values.

FIGURE 5: The top panel shows the Liquid Water Content versus time and pressure as the C-130 entered the adiabatic cloud from below. The bottom graph shows the measured Liquid Water Content versus time compared with the calculated adiabatic LWC profile assuming different cloud bases.

FIGURE 6: The CPI IWC and Concentration are shown along with the false LWC signal observed by the FSSP, PVM, and King probes.

FIGURE 7: Time series of the temperature and altitude recorded by the C-130 on 29 July 1998 as it sampled a boundary layer cloud as well as the calculated adiabatic temperature are shown in the top panel. FSSP size distributions for different time periods are shown in the middle. A time series of LWC recorded by several different probes is compared to the calculated adiabatic value in the bottom panel.

FIGURE 8: Time series of measurements from a boundary layer cloud on 29 July 1998. Conditional size spectra (as shown in figure 3) for each region are shown above.

FIGURE 9: Time series of measurements and their standard deviations made by the C-130 as it passed through two boundary layer adiabatic clouds.

FIGURE 10: Time series of measurements and their standard deviations made by the C-130 as it flew different level passes through boundary layer clouds on four different occasions.

FIGURE 11: Histograms of the number of particles per frame for all the CPI imaged frames during the time period 22:09:00 – 22:09:40 shown in Figures 2 and 9 along with the Poisson distribution with the same mean, and (bottom) conditional particle size distributions produced by using only those particles in frames with 5 or more particles (black) and by using those particles in frames with 3 or less particles per frame (gray).

FIGURE 12: Time series of measurements and their standard deviations made by the C-130 as it flew different level passes through a boundary layer cloud on 4 May 1998.

FIGURE 13: Example of a Boundary Layer Cloud with extremely variable hydrometeor fields that exist over relatively small (10 Km) spatial distances. The 3-D flight track is for the NCAR C-130 as it descended over the SHEBA ship. The times shown on the track correspond to the CPI derived particle size distributions of ice and the FSSP size distributions of water in the mixed phase clouds. Sample CPI images are shown for each particle size distribution.

FIGURE 14: Concentrations measured by the FSSP, 1DC, and 2DC, are plotted with the King LWC versus altitude for a thick stratus cloud observed on 18 July 1998. CPI particle size distributions for Ice and water as well as example images are shown to the right.

FIGURE 15: Total particle size distributions measured by the FSSP (*), CPI (solid line) and 2D-C (Δ) in the 'central' region with high ice concentrations near –12 ° C and the 'adjacent' regions immediately above and below the central region. Water and ice particle size distributions are derived from CPI image data; examples of CPI images are also shown.

FIGURE 16: As in Figure 15, except for the 'central' and 'adjacent' regions near –4.5 ° C.

FIGURE 17: Particle size distributions measured by the FSSP (*), CPI (solid line) and the 2D-C (Δ) for an arctic cirrus cloud observed on 29 July 1998.

FIGURE 18: Time series of particle concentrations measured by various instruments while passing through an arctic cirrus cloud on 29 July 1998 (the time shown is actually on 30 July 1998 starting at 00:07 UTC).

FIGURE 19: Histograms of the number of particles per frame for all the CPI imaged frames during the time period shown in Figure 18 along with the Poisson

distribution with the same mean, and (bottom) conditional particle size distributions produced by using only those particles in frames with 9 or more particles (black) and by using only particles that were imaged alone in a frame (gray).

FIGURE 20: Images of arctic cirrus ice particles sampled on 29 July 1998 during FIRE.ACE. Each box with a large crystal and each group of small boxes represents one CPI image frame. The image frames reflect the relative positions of the particles along the flight track. A significant point here is that the spatial variation between low concentrations of large particles and high concentrations of small particles

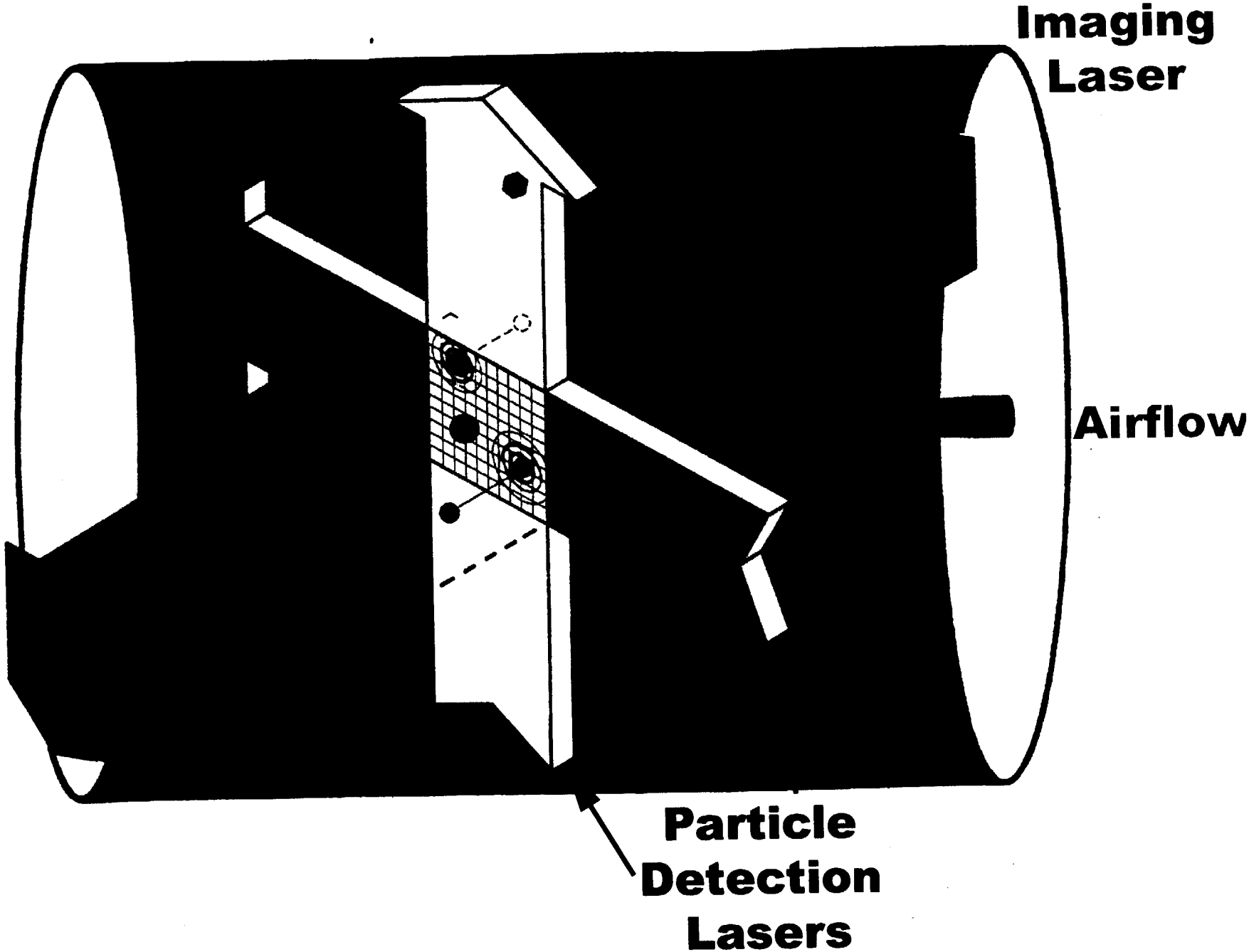

Figure 1

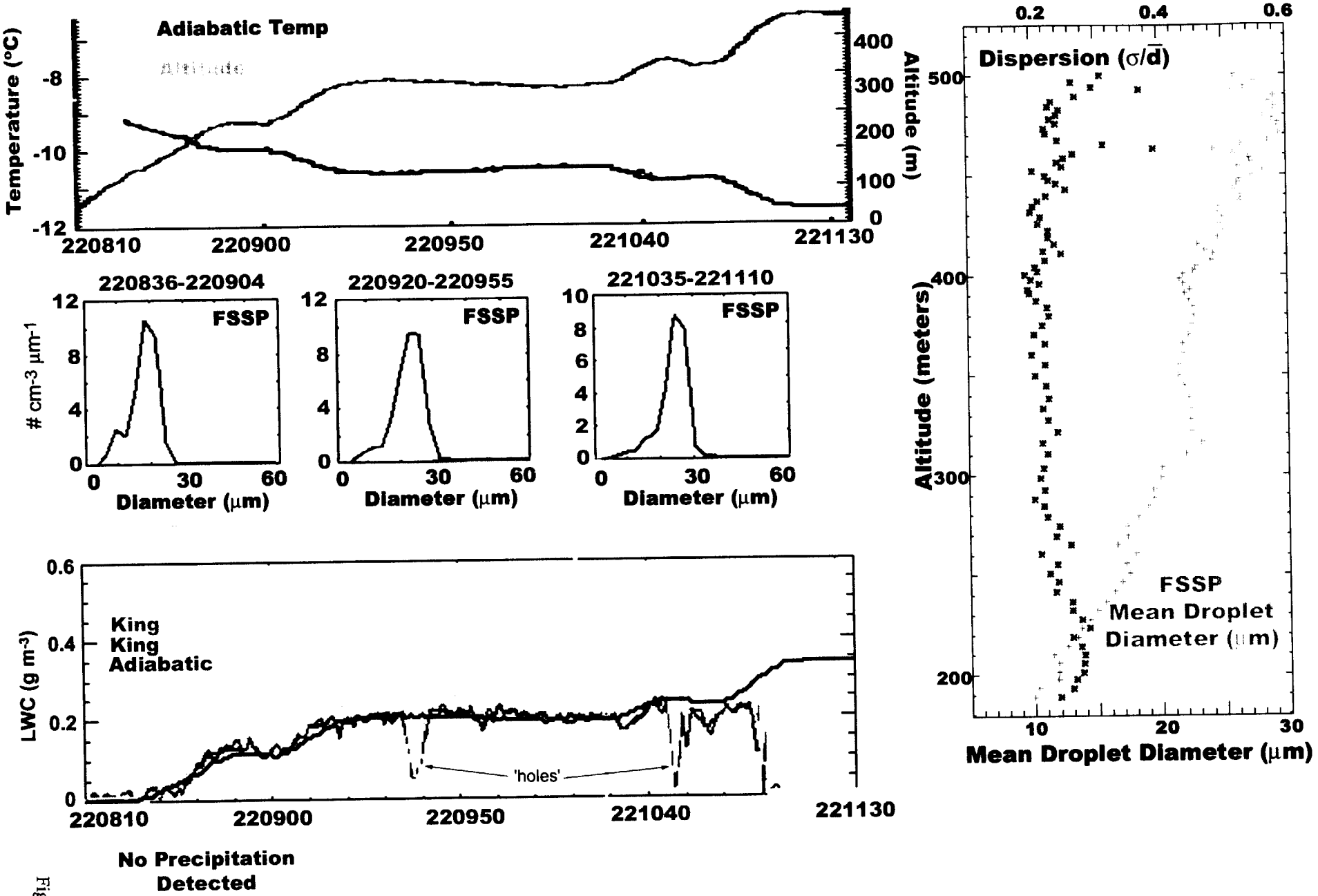
Adiabatic Temp
Temperature (°C)
-8
-10
-12
400
300
200
100
0
220810
220900
220950
221040
221130
220836-220904
220920-220955
221035-221110
FSSP
cm-3 μm-1
Diameter (μm)
King
King
Adiabatic
LWC (g m-3)
'holes'
No Precipitation
Detected
Dispersion (σ/d̄)
Altitude (meters)
FSSP
Mean Droplet
Diameter (μm)
Mean Droplet Diameter (μm)

Figure 2

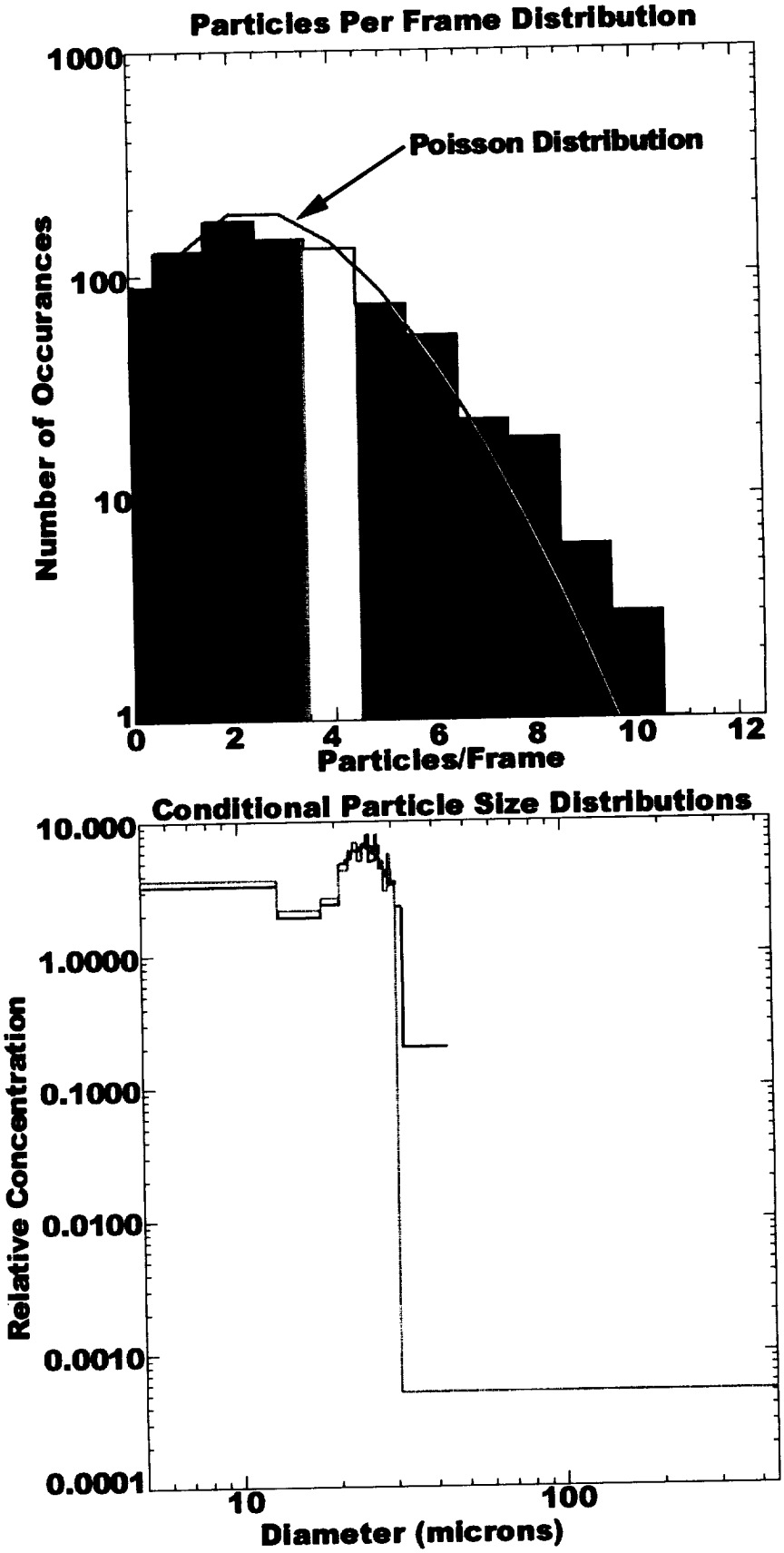
Particles Per Frame Distribution
Poisson Distribution
Number of Occurances
1000
100
10
1
0
2
4
6
8
10
12
Particles/Frame
Conditional Particle Size Distributions
Relative Concentration
10.000
1.0000
0.1000
0.0100
0.0010
0.0001
10
100
Diameter (microns)

Figure 3

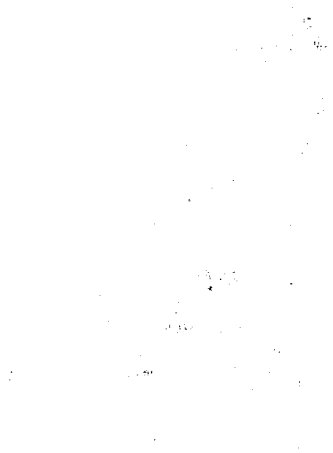

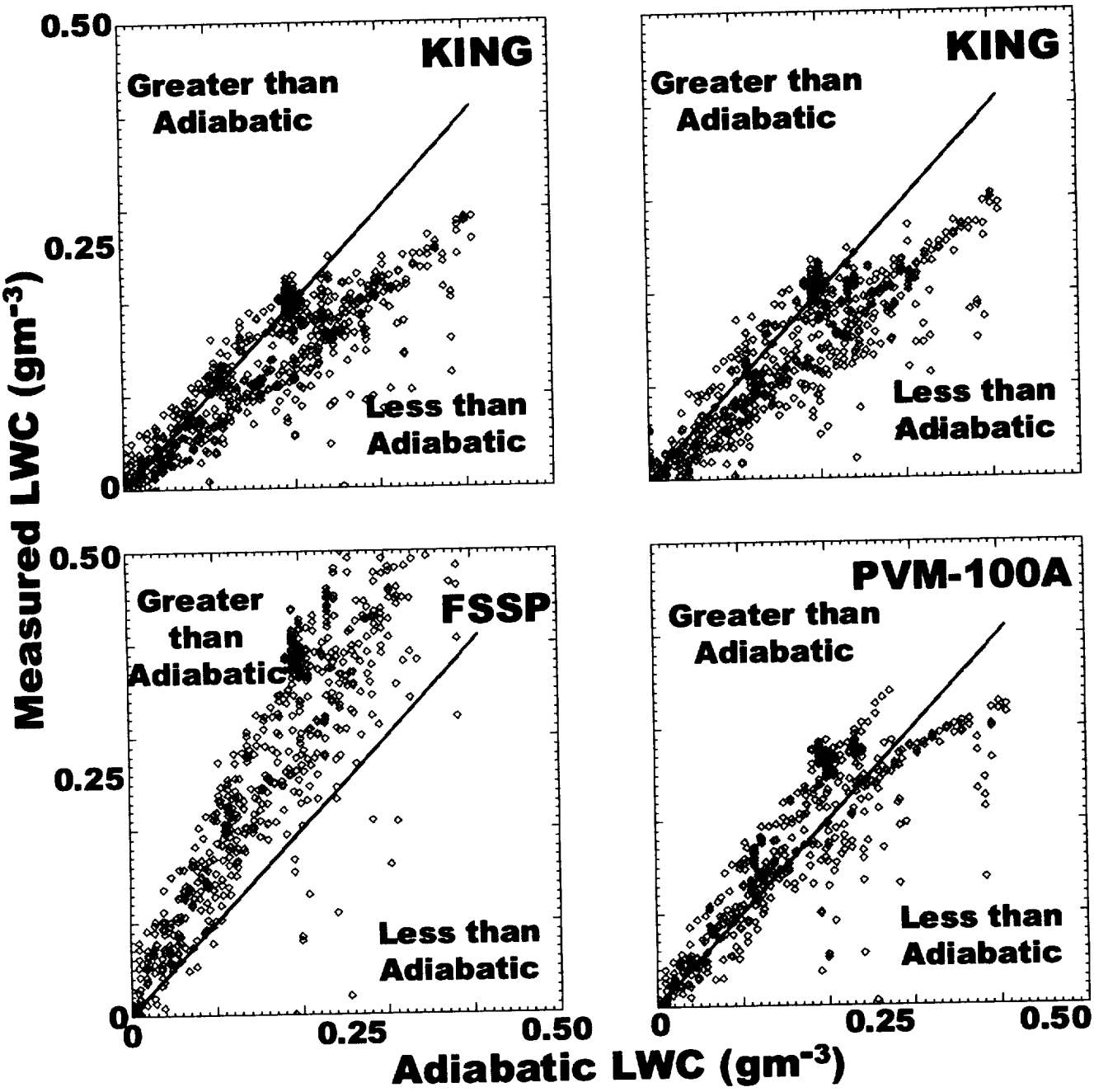
KING
Greater than Adiabatic
Less than Adiabatic
KING
Greater than Adiabatic
Less than Adiabatic
FSSP
Greater than Adiabatic
Less than Adiabatic
PVM-100A
Greater than Adiabatic
Less than Adiabatic
Measured LWC (gm-3)
Adiabatic LWC (gm-3)
0
0.25
0.50

Figure 4

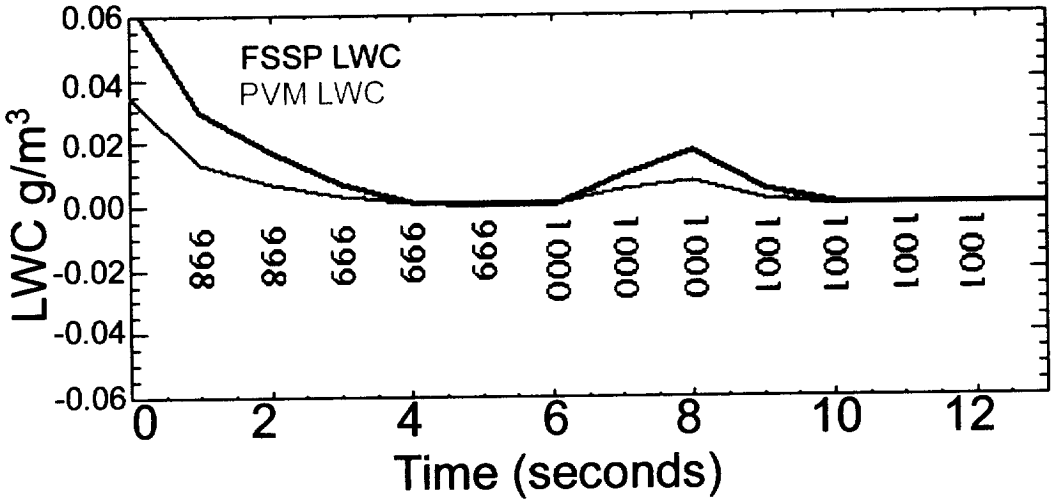
FSSP LWC
PVM LWC
LWC g/m3
Time (seconds)
866
866
666
666
666
1000
1000
1000
1001
1001
1001
1001

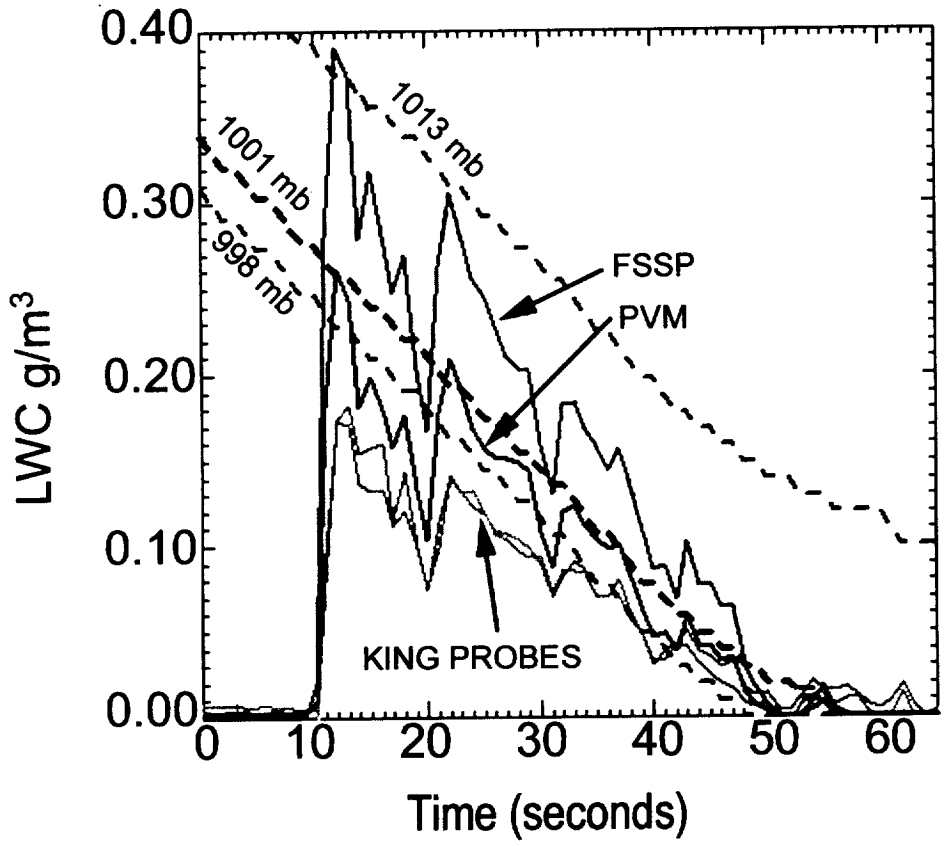
1013 mb
1001 mb
998 mb
FSSP
PVM
KING PROBES
LWC g/m3
Time (seconds)

Figure 5

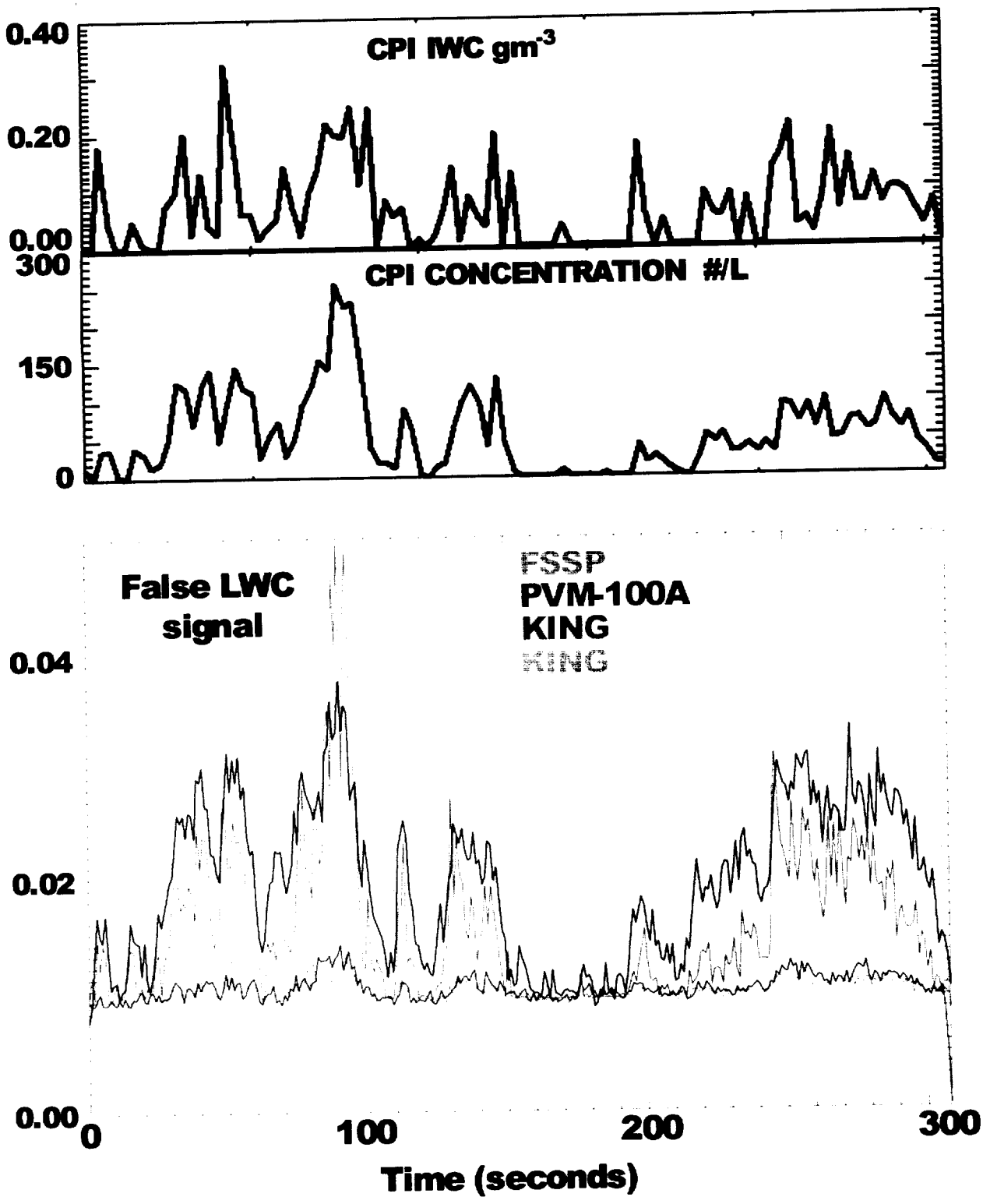
0.40
0.20
0.00
CPI IWC gm-3
300
150
0
CPI CONCENTRATION #/L
False LWC signal
FSSP
PVM-100A
KING
KING
0.04
0.02
0.00
0
100
200
300
Time (seconds)

Figure 6

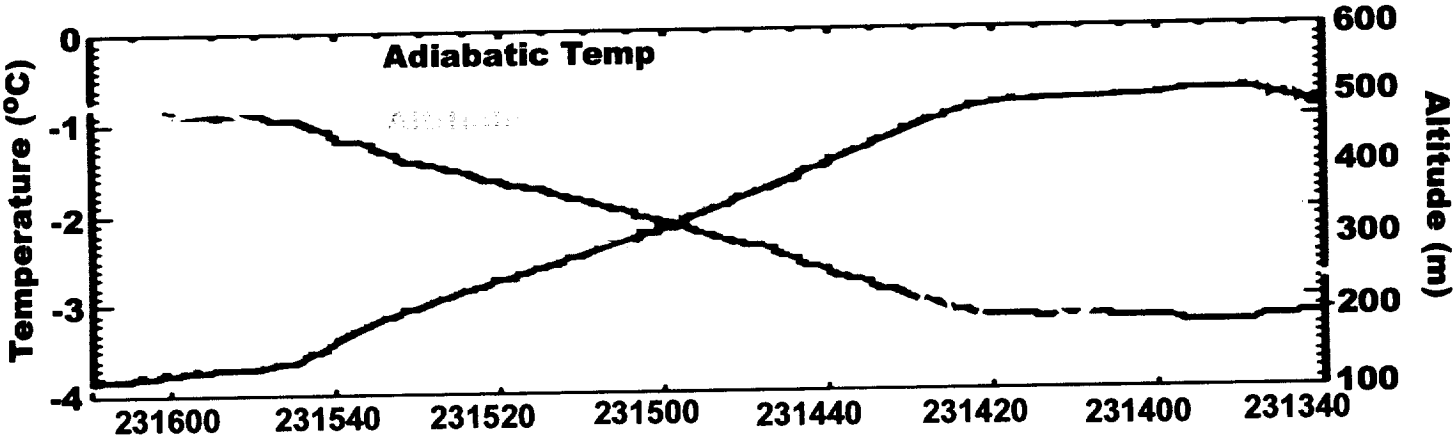

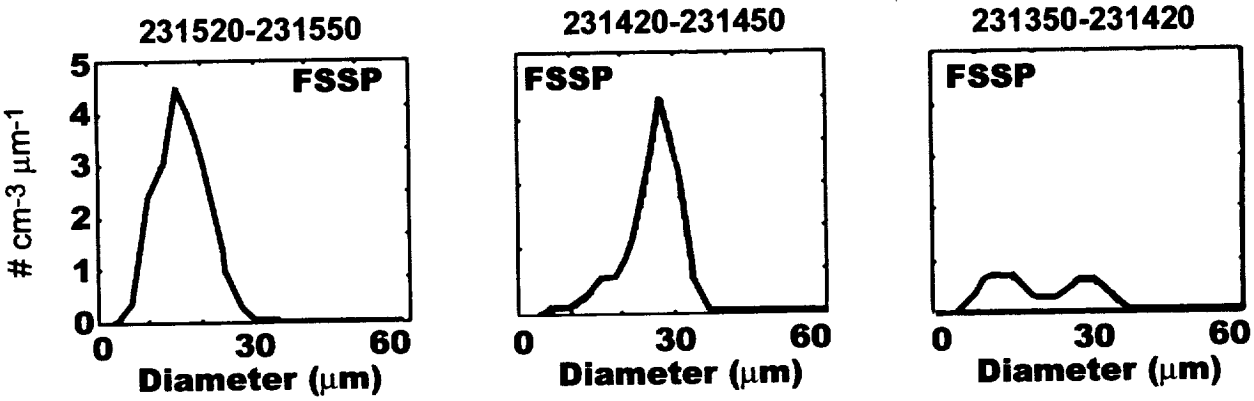

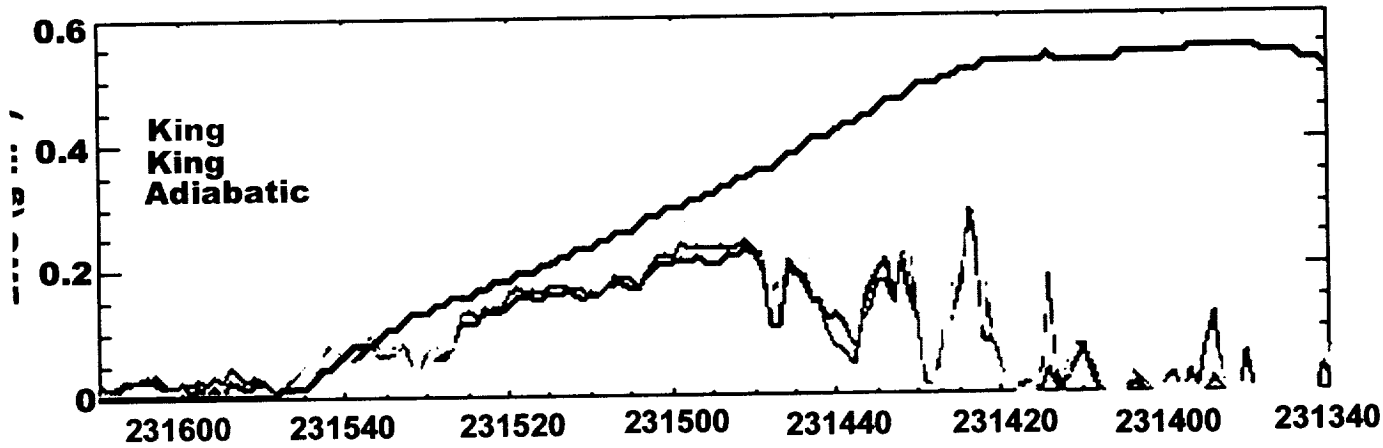

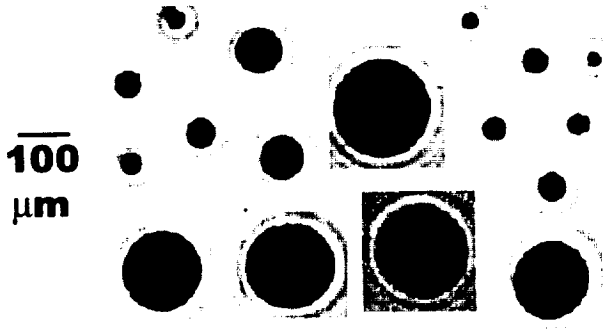

Drizzle Precipitating from cloud base.

Figure 7

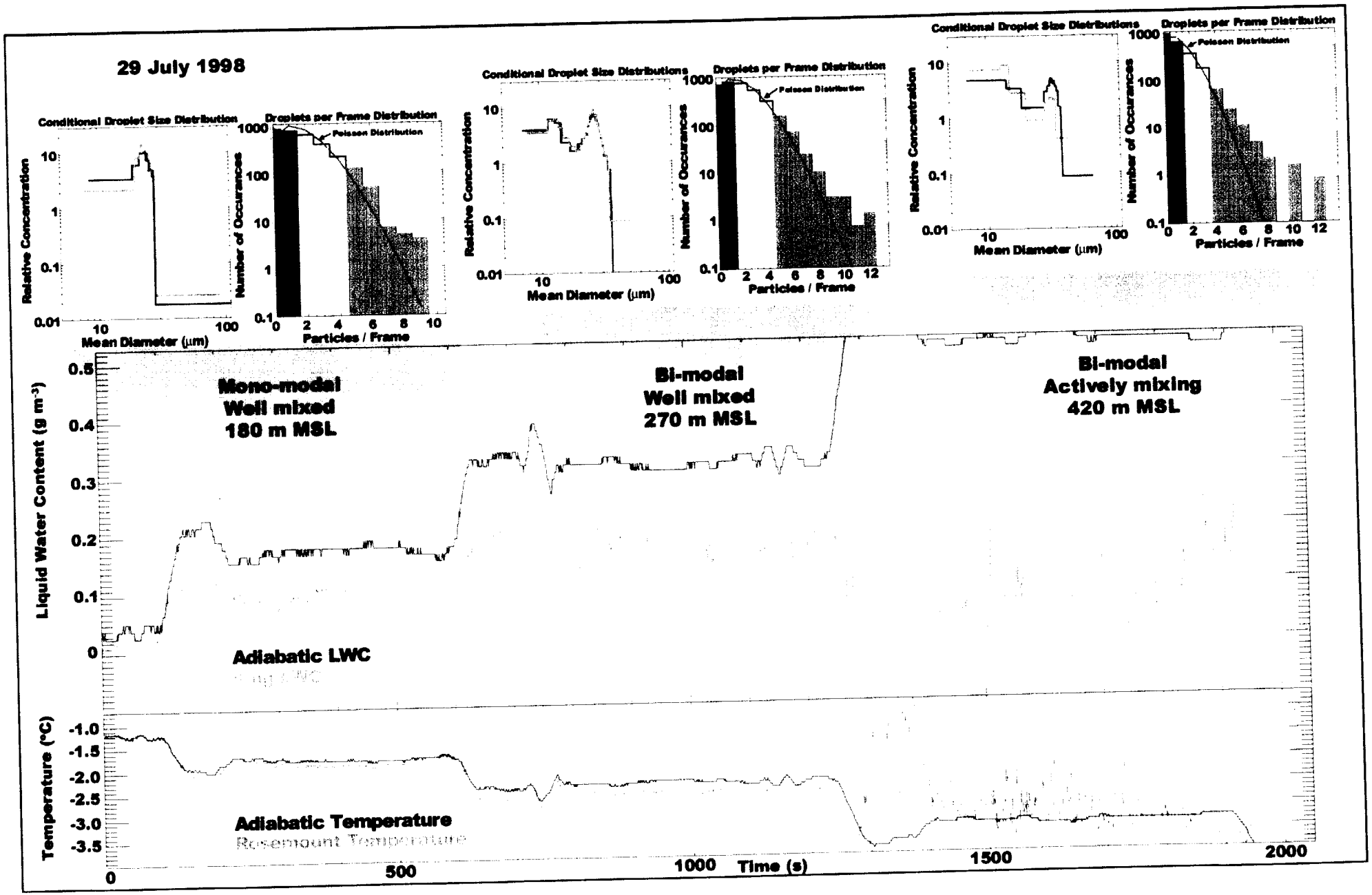
29 July 1998
Conditional Droplet Size Distribution
Relative Concentration
Mean Diameter (μm)
Droplets per Frame Distribution
Number of Occurances
Particles / Frame
Poisson Distribution
Mono-modal
Well mixed
180 m MSL
Bi-modal
Well mixed
270 m MSL
Bi-modal
Actively mixing
420 m MSL
Liquid Water Content (g m-3)
Adiabatic LWC
Temperature (°C)
Adiabatic Temperature
Rosemount Temperature
Time (s)

Figure 8

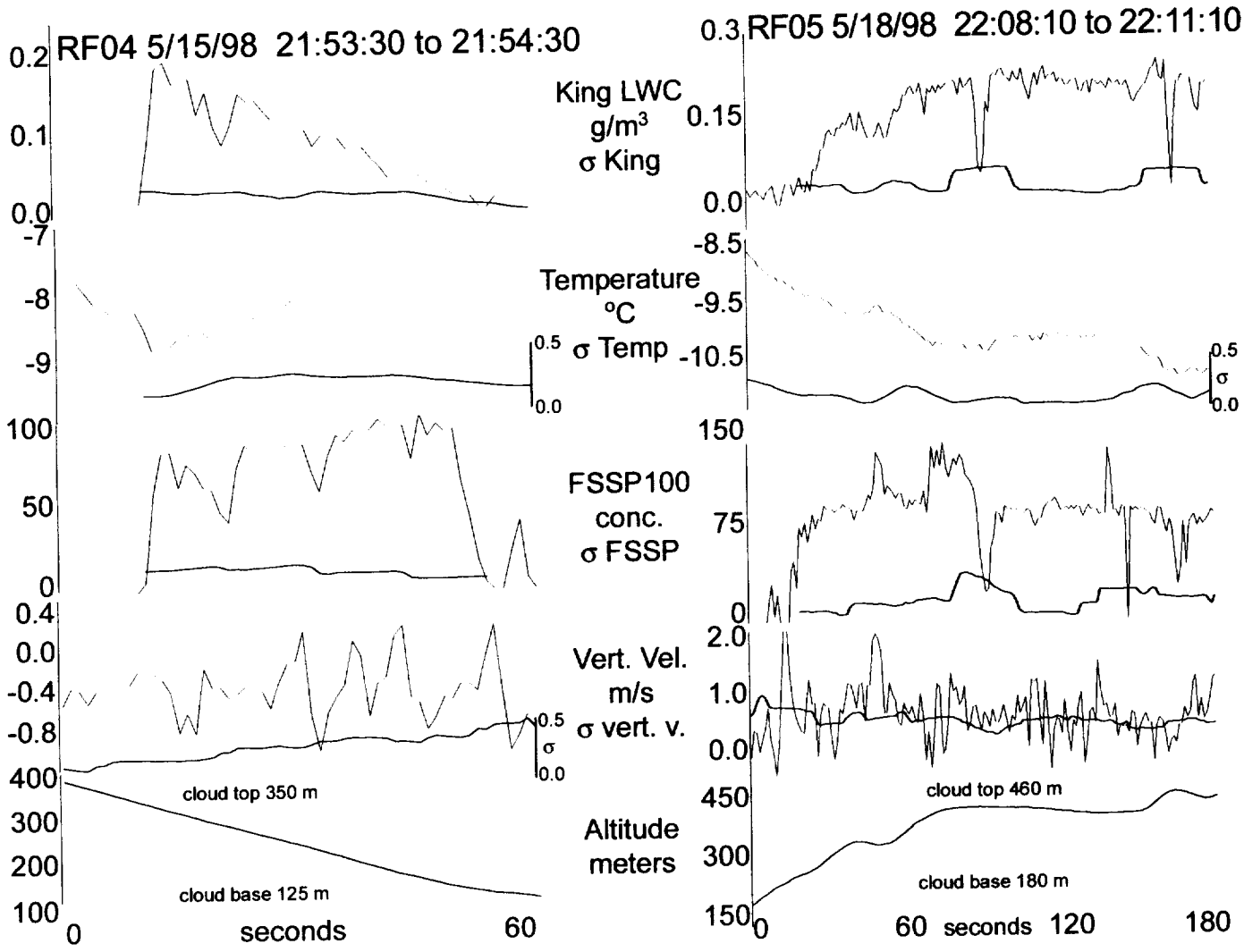
RF04 5/15/98 21:53:30 to 21:54:30
RF05 5/18/98 22:08:10 to 22:11:10
King LWC
g/m3
σ King
Temperature
°C
σ Temp
FSSP100
conc.
σ FSSP
Vert. Vel.
m/s
σ vert. v.
Altitude
meters
cloud top 350 m
cloud base 125 m
cloud top 460 m
cloud base 180 m
seconds
seconds

Figure 9

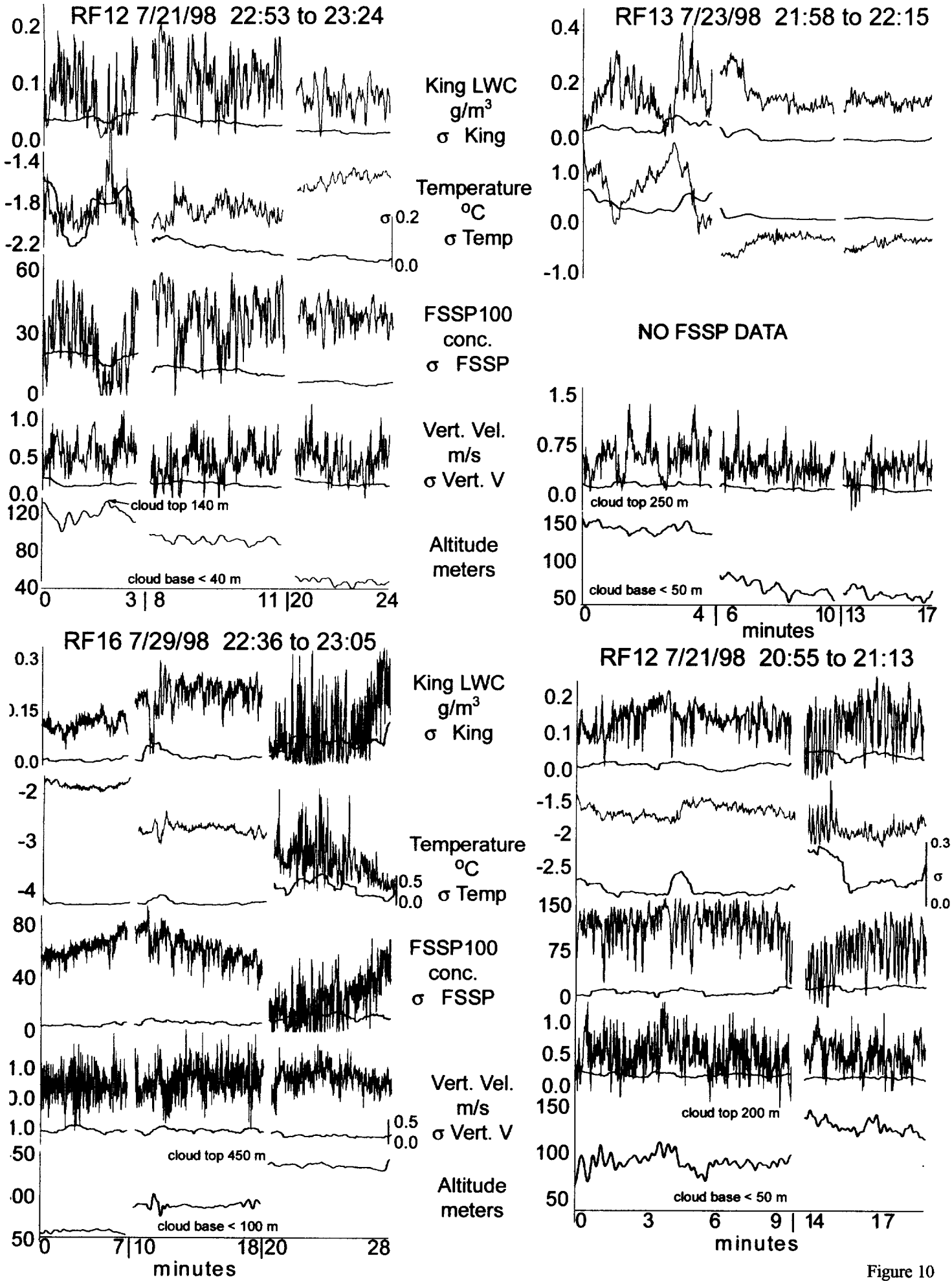
RF12 7/21/98 22:53 to 23:24
King LWC g/m3
σ King
Temperature °C
σ Temp
FSSP100 conc.
σ FSSP
Vert. Vel. m/s
σ Vert. V
cloud top 140 m
cloud base < 40 m
Altitude meters
minutes
RF13 7/23/98 21:58 to 22:15
NO FSSP DATA
cloud top 250 m
cloud base < 50 m
minutes
RF16 7/29/98 22:36 to 23:05
King LWC g/m3
σ King
Temperature °C
σ Temp
FSSP100 conc.
σ FSSP
Vert. Vel. m/s
σ Vert. V
cloud top 450 m
cloud base < 100 m
Altitude meters
minutes
RF12 7/21/98 20:55 to 21:13
cloud top 200 m
cloud base < 50 m
minutes

Figure 10

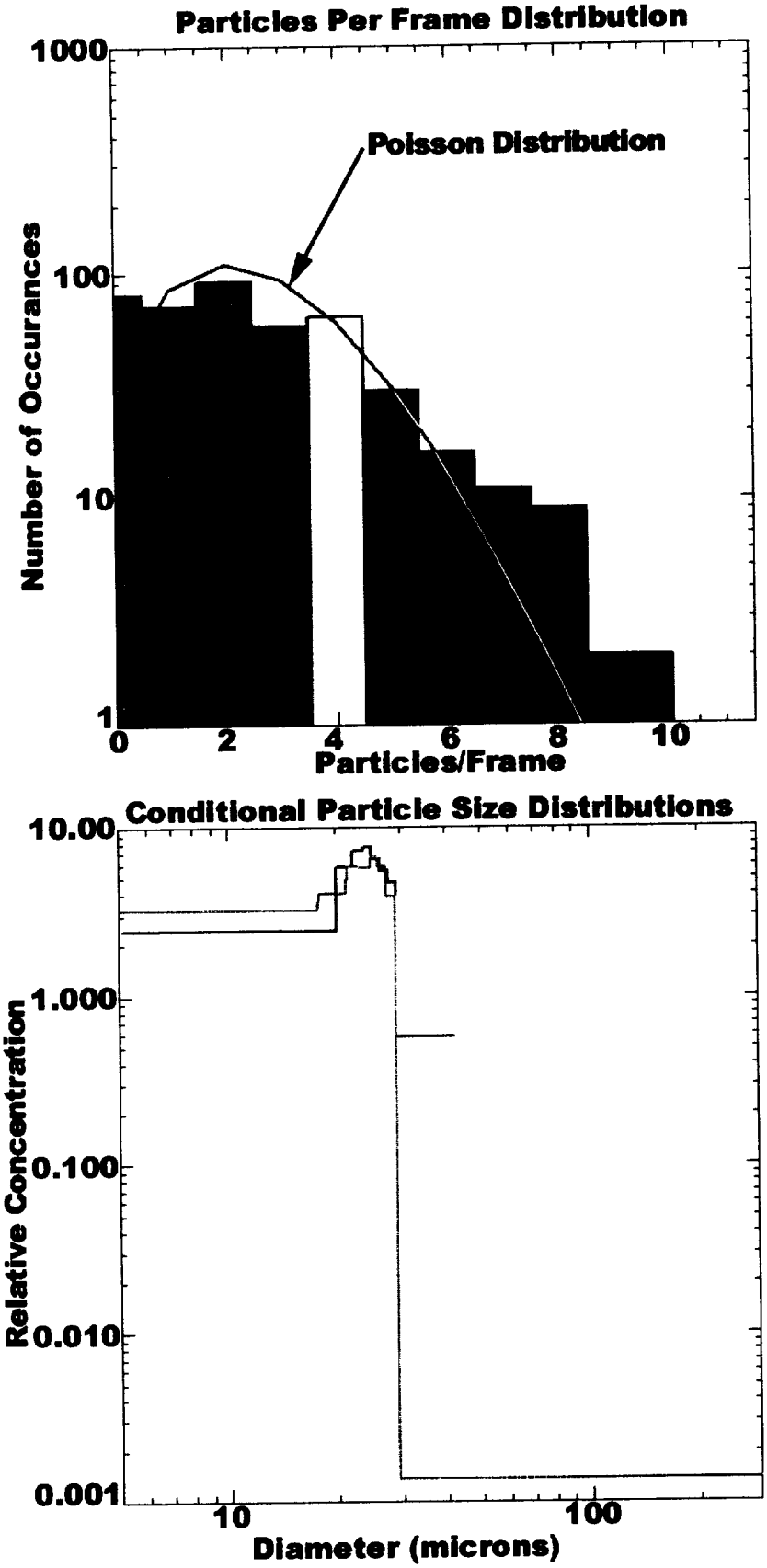
Particles Per Frame Distribution
1000
100
10
1
Number of Occurances
Poisson Distribution
0
2
4
6
8
10
Particles/Frame
Conditional Particle Size Distributions
10.00
1.000
0.100
0.010
0.001
Relative Concentration
10
100
Diameter (microns)

Figure 11

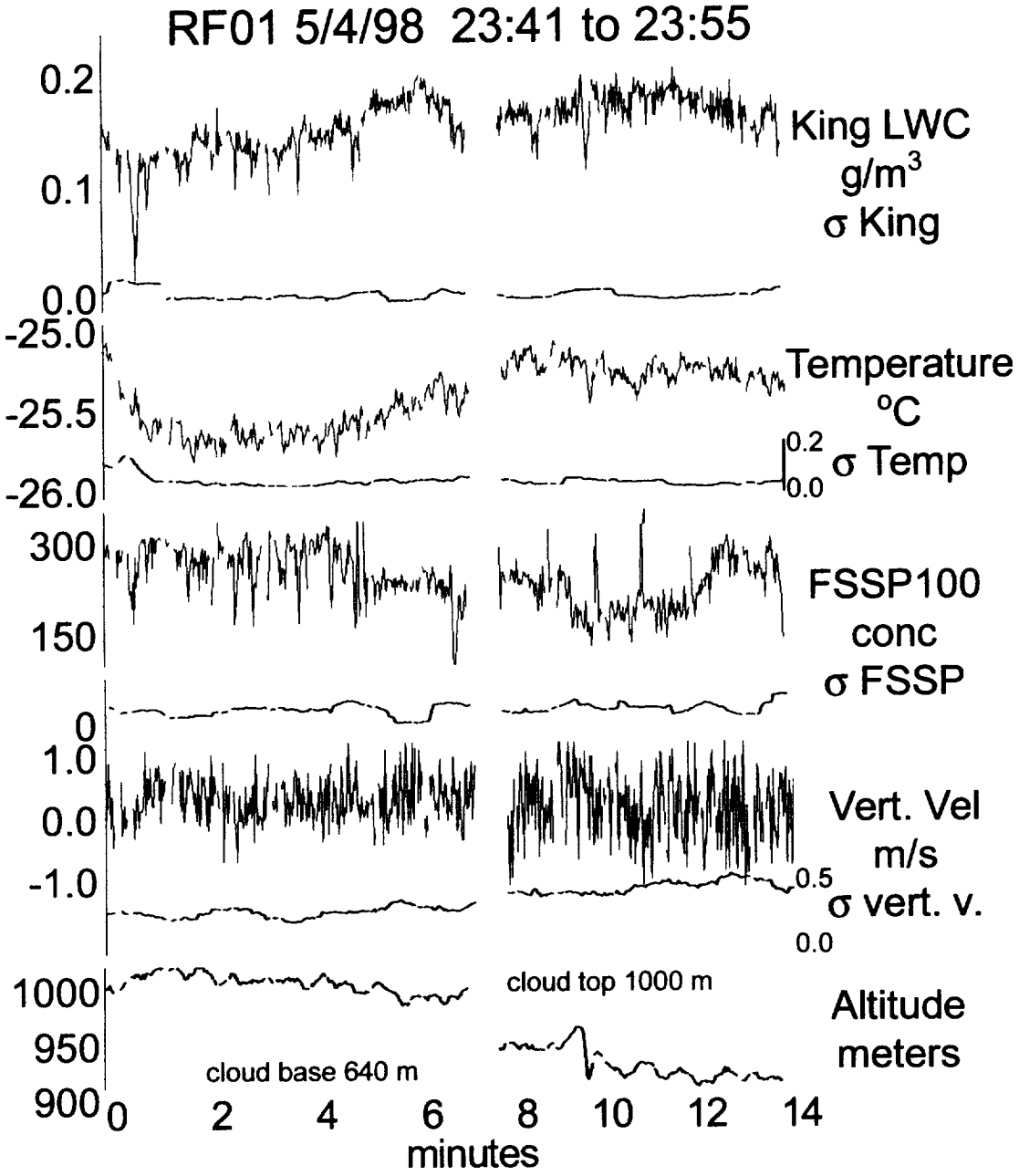
RF01 5/4/98 23:41 to 23:55
0.2
0.1
0.0
King LWC
g/m3
σ King
-25.0
-25.5
-26.0
Temperature
°C
0.2
0.0
σ Temp
300
150
0
FSSP100
conc
σ FSSP
1.0
0.0
-1.0
Vert. Vel
m/s
0.5
0.0
σ vert. v.
1000
950
900
cloud base 640 m
cloud top 1000 m
Altitude
meters
0
2
4
6
8
10
12
14
minutes

Figure 12

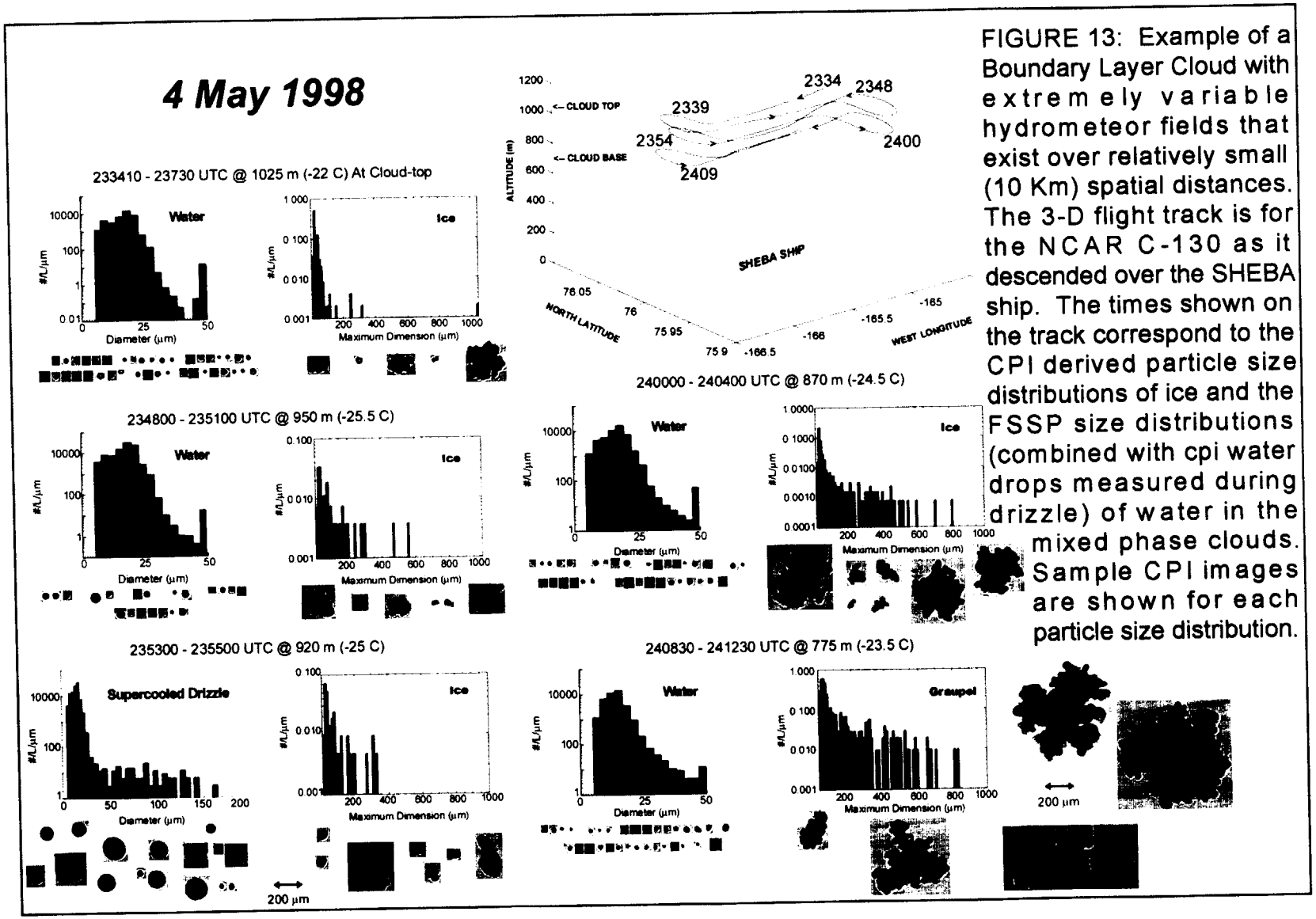

FIGURE 13: Example of a Boundary Layer Cloud with extremely variable hydrometeor fields that exist over relatively small (10 Km) spatial distances. The 3-D flight track is for the NCAR C-130 as it descended over the SHEBA ship. The times shown on the track correspond to the CPI derived particle size distributions of ice and the FSSP size distributions (combined with cpi water drops measured during drizzle) of water in the mixed phase clouds. Sample CPI images are shown for each particle size distribution.

Figure 13

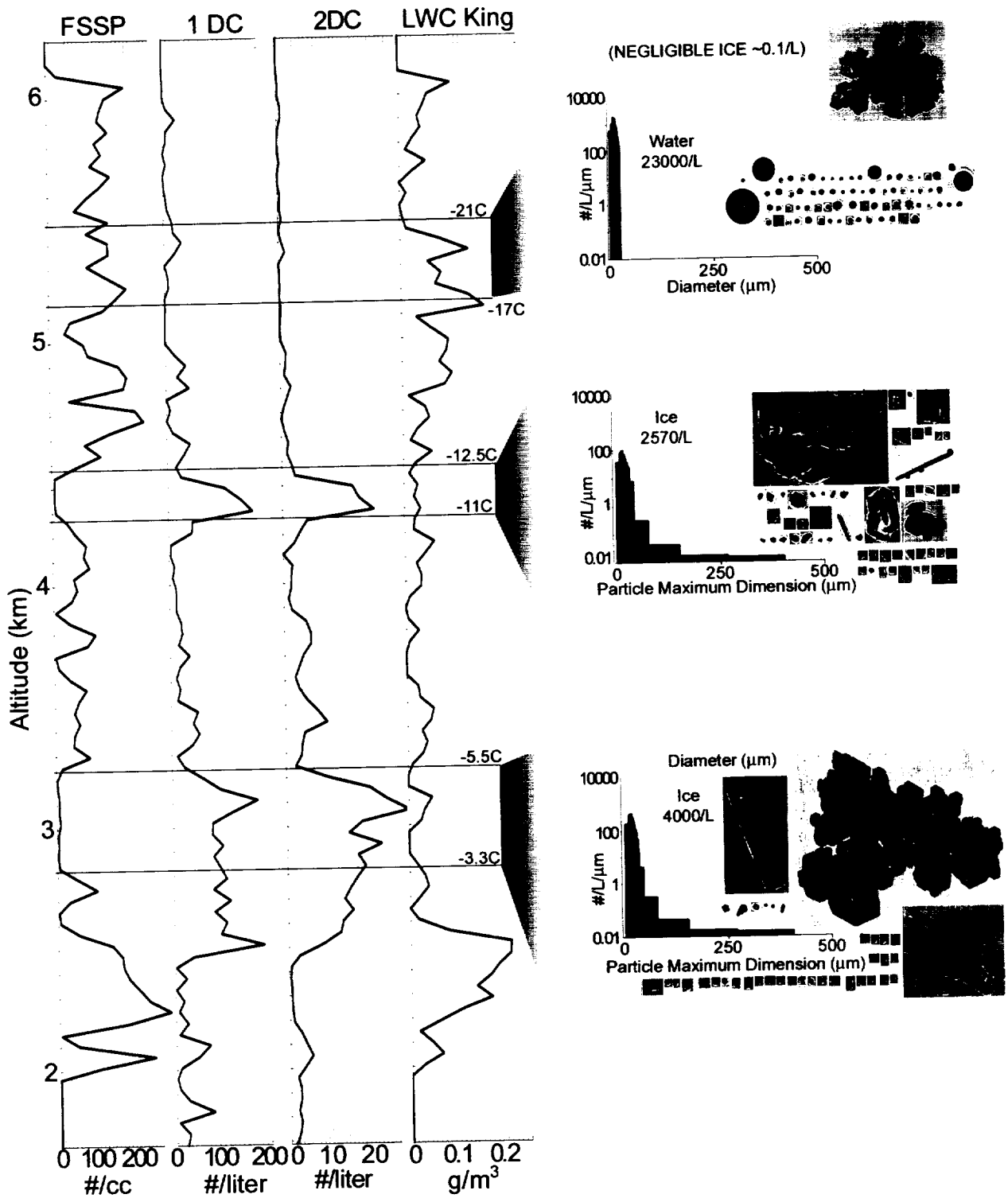
FSSP
1 DC
2DC
LWC King
Altitude (km)
6
5
4
3
2
-21C
-17C
-12.5C
-11C
-5.5C
-3.3C
0 100 200
#/cc
0 100 200
#/liter
0 10 20
#/liter
0 0.1 0.2
g/m3
(NEGLIGIBLE ICE ~0.1/L)
10000
100
1
0.01
#/L/µm
Water
23000/L
0
250
500
Diameter (µm)
Ice
2570/L
Particle Maximum Dimension (µm)
Diameter (µm)
Ice
4000/L
Particle Maximum Dimension (µm)

Figure 14

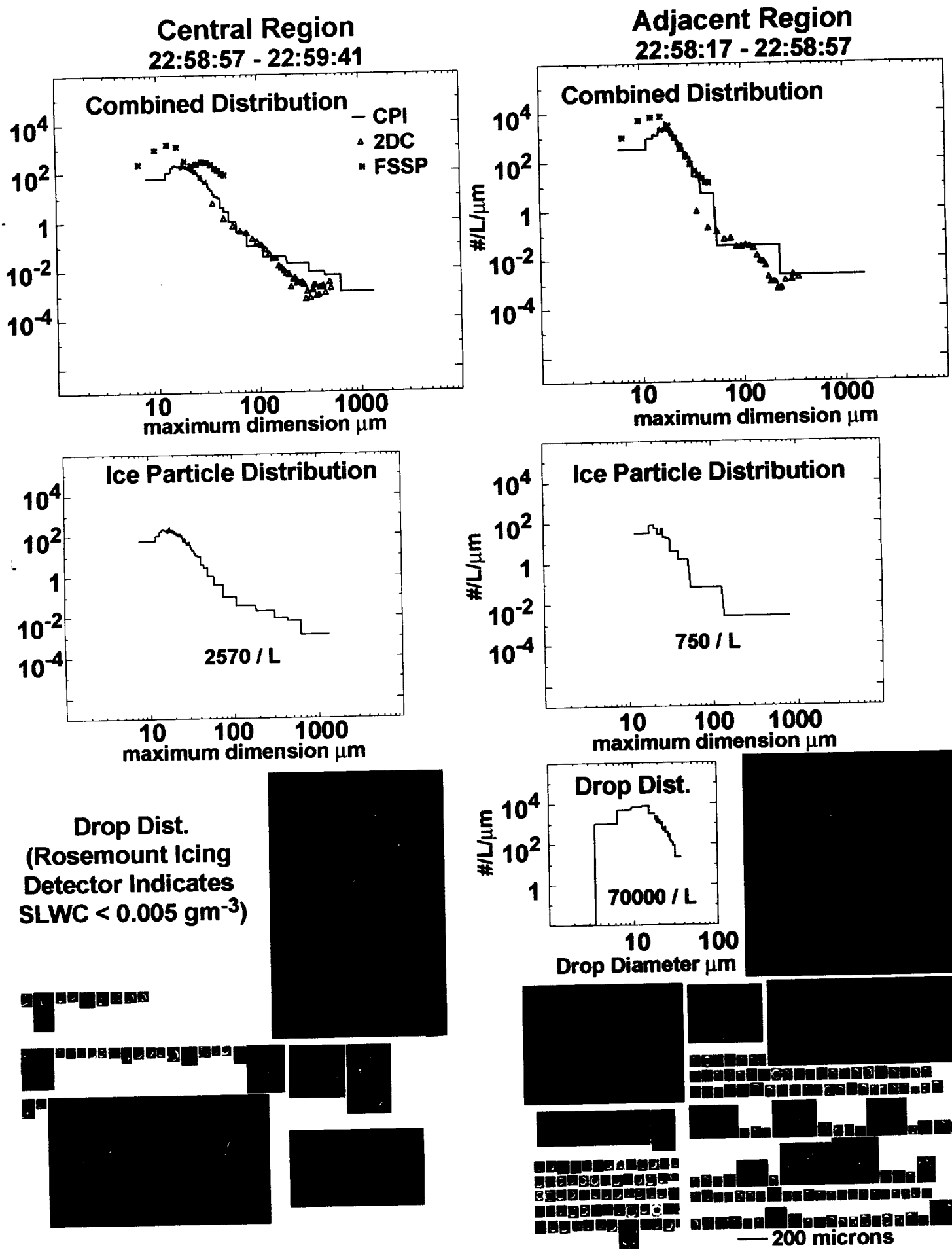
Central Region
22:58:57 - 22:59:41
Combined Distribution
CPI
2DC
FSSP
#/L/μm
maximum dimension μm
Adjacent Region
22:58:17 - 22:58:57
Combined Distribution
maximum dimension μm
Ice Particle Distribution
2570 / L
maximum dimension μm
Ice Particle Distribution
750 / L
maximum dimension μm
Drop Dist.
(Rosemount Icing
Detector Indicates
SLWC < 0.005 gm-3)
Drop Dist.
70000 / L
Drop Diameter μm
200 microns

Figure 15

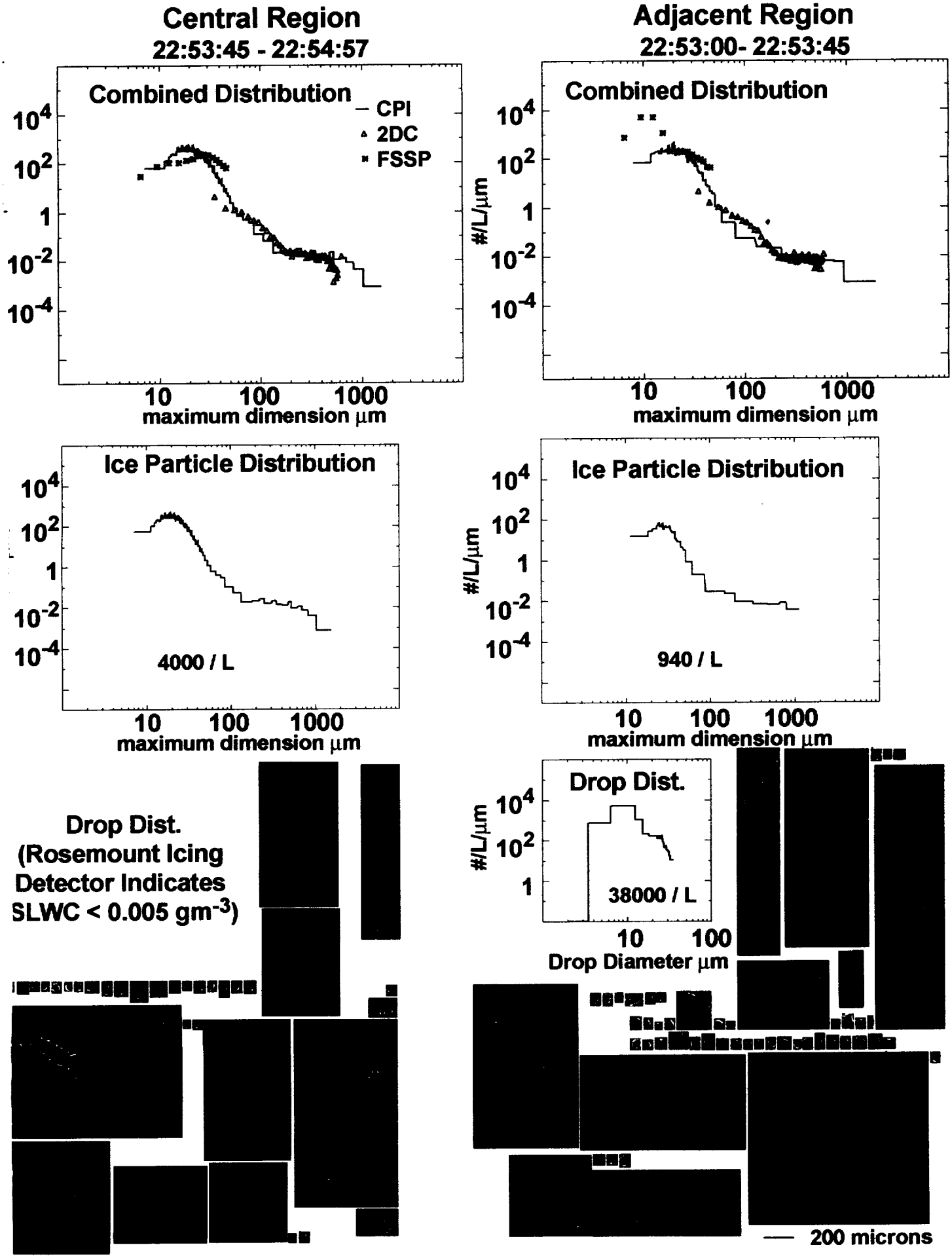
Central Region
22:53:45 - 22:54:57
Combined Distribution
CPI
2DC
FSSP
maximum dimension μm
Ice Particle Distribution
4000 / L
maximum dimension μm
Drop Dist.
(Rosemount Icing
Detector Indicates
SLWC < 0.005 gm-3)
Adjacent Region
22:53:00- 22:53:45
Combined Distribution
#/L/μm
maximum dimension μm
Ice Particle Distribution
940 / L
maximum dimension μm
Drop Dist.
38000 / L
Drop Diameter μm
200 microns

Figure 16

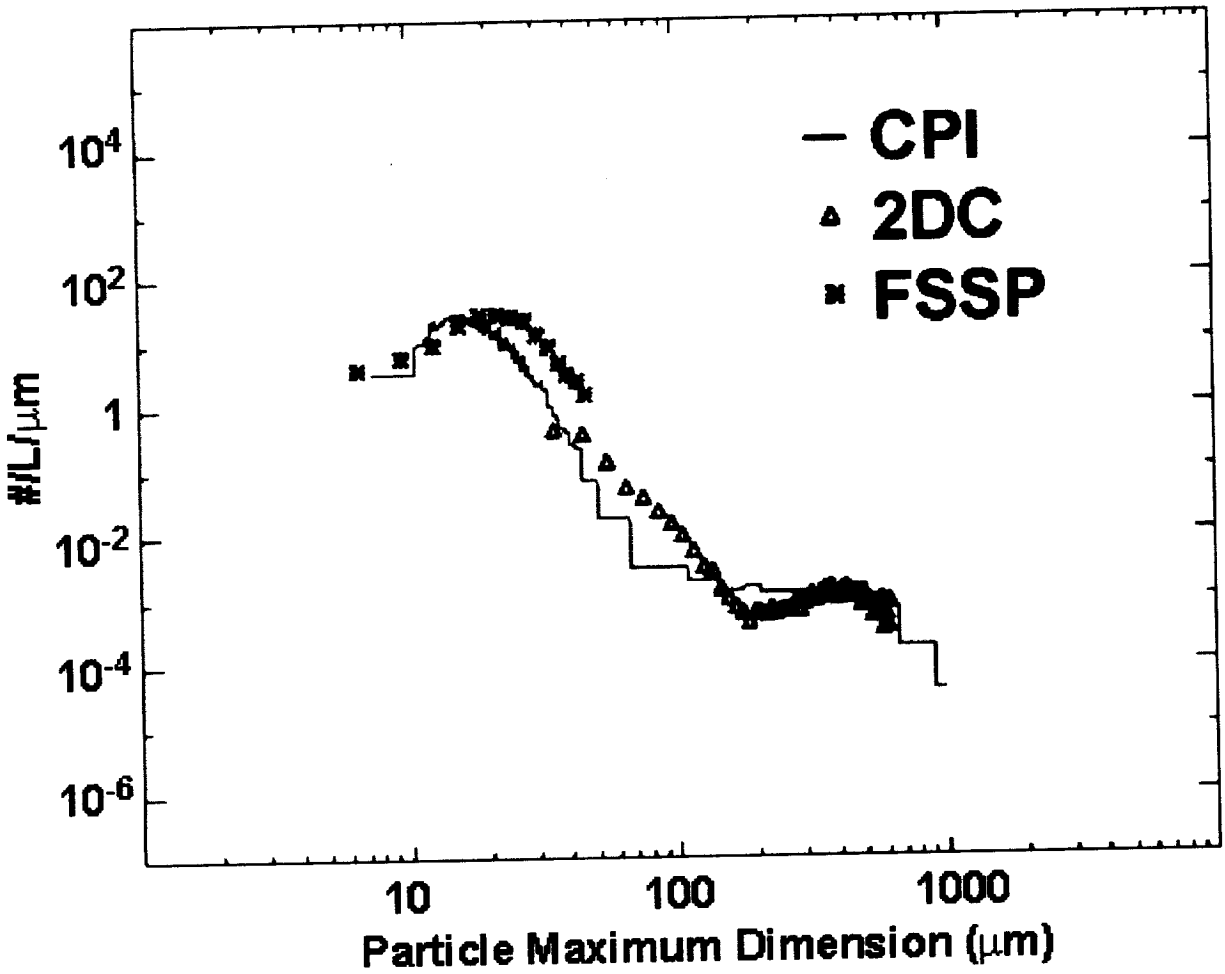
CPI
2DC
FSSP
#/L/μm
10^4
10^2
1
10^-2
10^-4
10^-6
10
100
1000
Particle Maximum Dimension (μm)

Figure 17

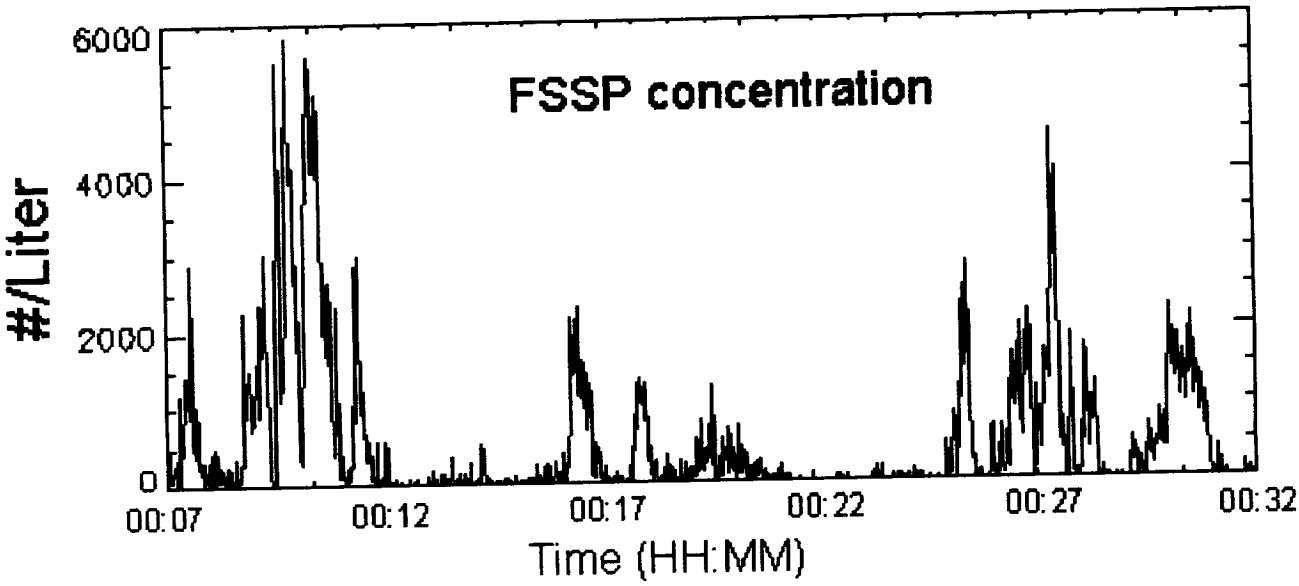
FSSP concentration
#/Liter
6000
4000
2000
0
00:07
00:12
00:17
00:22
00:27
00:32
Time (HH:MM)

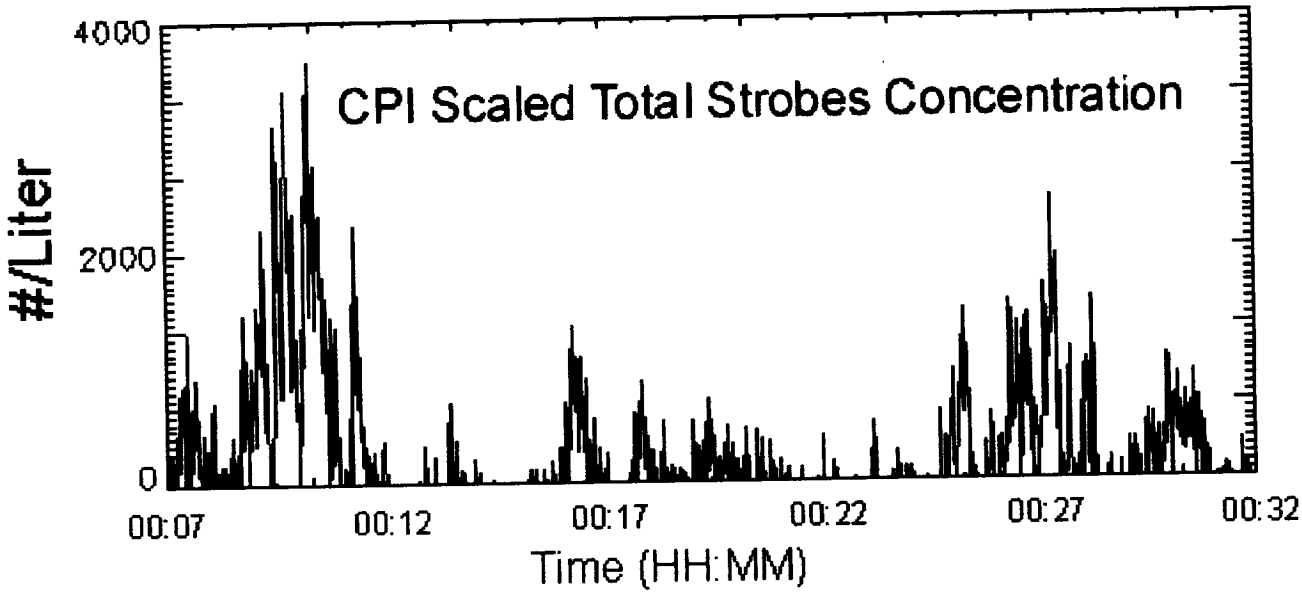
CPI Scaled Total Strobes Concentration
#/Liter
4000
2000
0
00:07
00:12
00:17
00:22
00:27
00:32
Time (HH:MM)

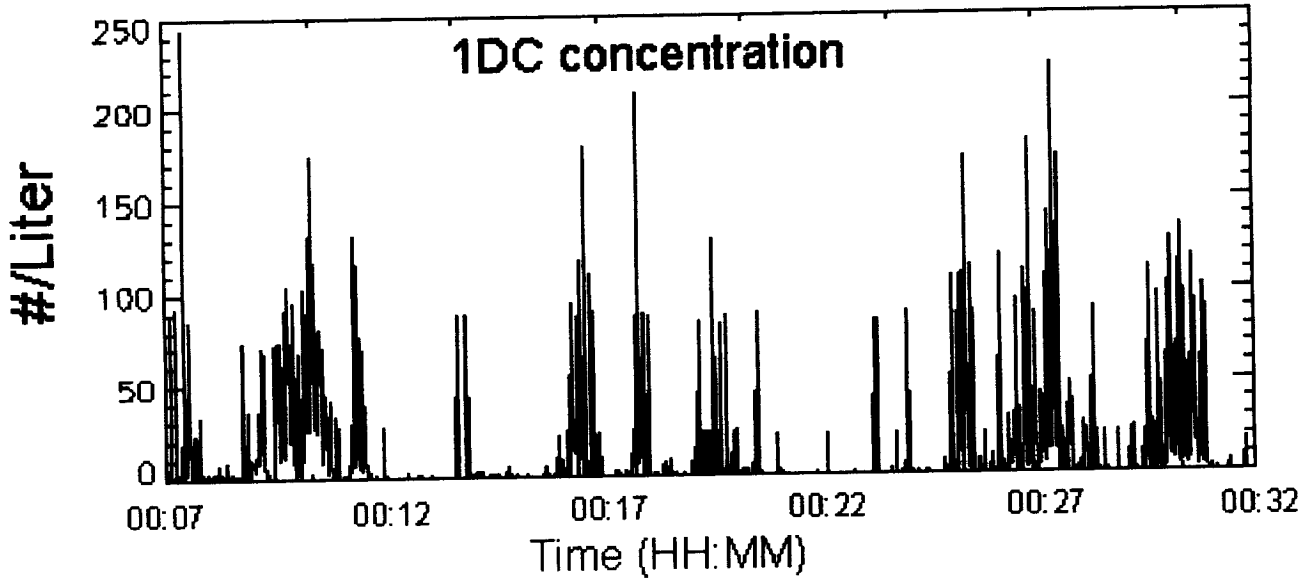
1DC concentration
#/Liter
250
200
150
100
50
0
00:07
00:12
00:17
00:22
00:27
00:32
Time (HH:MM)

Figure 18

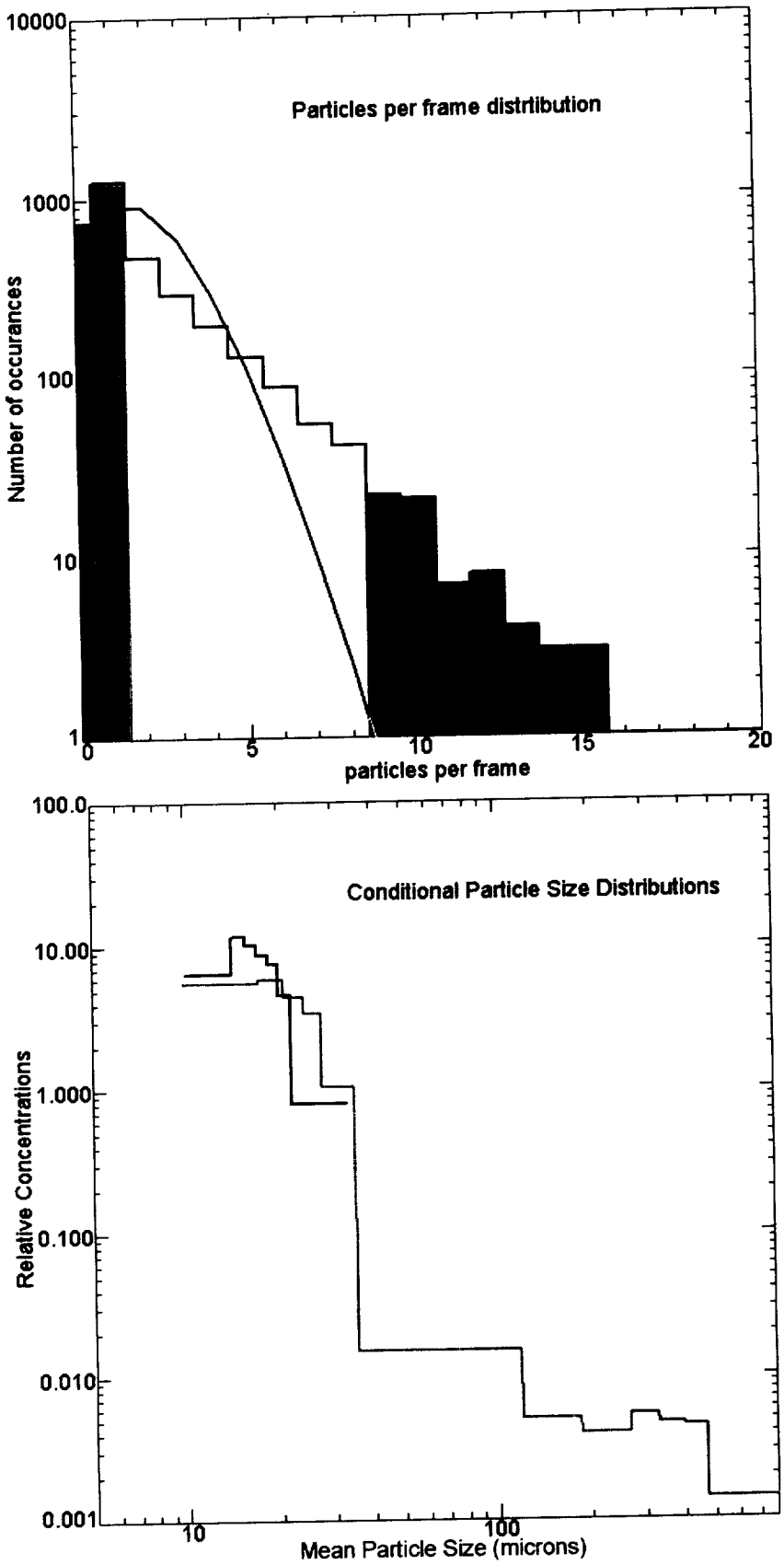
Particles per frame distrtibution
Number of occurances
10000
1000
100
10
1
0
5
10
15
20
particles per frame
Conditional Particle Size Distributions
Relative Concentrations
100.0
10.00
1.000
0.100
0.010
0.001
10
100
Mean Particle Size (microns)

Figure 19

Figure 20

REPORT DOCUMENTATION PAGE

Form Approved
OMB No. 0704-0188

1. AGENCY USE ONLY (Leave blank)	2. REPORT DATE	3. REPORT TYPE AND DATES COVERED
	December 7, 2000	Final Report (9/10/98 - 12/7/00)

4. TITLE AND SUBTITLE

A New Digital Holographic Instrument for Measuring Microphysical Properties of Contrails in the SASS (Subsonic Assessment) Program

5. FUNDING NUMBERS

NAS2-14258

6. AUTHOR(S)

R. Paul Lawson

7. PERFORMING ORGANIZATION NAME(S) AND ADDRESS(ES)

SPEC, Inc.
5401 Western Avenue, Suite B
Boulder, CO 80301

8. PERFORMING ORGANIZATION REPORT NUMBER

N/A

9. SPONSORING/MONITORING AGENCY NAME(S) AND ADDRESS(ES)

NASA Ames Research Center
Moffett Field, CA 94035-1000

10. SPONSORING/MONITORING AGENCY REPORT NUMBER

N/A

11. SUPPLEMENTARY NOTES

12a. DISTRIBUTION/AVAILABILITY STATEMENT

Same as Report (SAR)

12b. DISTRIBUTION CODE

Unknown

13. ABSTRACT *(Maximum 200 words)*

SPEC incorporated designed, built and operated a new instrument, called a Π-Nephelometer, on the NASA DC-8 for the SUCCESS field project. The Π-Nephelometer casts an image of a particle on a 400,000 pixel solid-state camera by freezing the motion of the particle using a 25 ns pulsed, high-power (60 W) laser diode. Unique optical imaging and particle detection systems precisely detect particles and define the depth-of-field so that at least one particle in the image is almost always in focus. A powerful image processing engine processes frames from the solid-state camera, identifies and records regions of interest (i.e. particle images) in real time. Images of ice crystals are displayed and recorded with 5 micron pixel resolution. In addition, a scattered light system simultaneously measures the scattering phase function of the imaged particle. The system consists of twenty-eight 1-mm optical fibers connected to microlenses bonded on the surface of avalanche photo diodes (APDs). Data collected with the Π-Nephelometer during the SUCCESS field project was reported in a special issue of *Geophysical Research Letters*. The Π-Nephelometer provided the basis for development of a commercial imaging probe, called the cloud particle imager (CPI), which has been installed on several research aircraft and used in more than a dozen field programs.

14. SUBJECT TERMS

15. NUMBER OF PAGES
86 (incl.Form298)

16. PRICE CODE

17. SECURITY CLASSIFICATION OF REPORT	18. SECURITY CLASSIFICATION OF THIS PAGE	19. SECURITY CLASSIFICATION OF ABSTRACT	20. LIMITATION OF ABSTRACT

GENERAL INSTRUCTIONS FOR COMPLETING SF 298

The Report Documentation Page (RDP) is used in announcing and cataloging reports. It is important that this information be consistent with the rest of the report, particularly the cover and title page. Instructions for filling in each block of the form follow. It is important to ***stay within the lines*** to meet ***optical scanning requirements***.

Block 1. Agency Use Only *(Leave blank)*.

Block 2. Report Date. Full publication date including day, month, and year, if available (e.g. 1 Jan 88). Must cite at least the year.

Block 3. Type of Report and Dates Covered. State whether report is interim, final, etc. If applicable, enter inclusive report dates (e.g. 10 Jun 87 - 30 Jun 88).

Block 4. Title and Subtitle. A title is taken from the part of the report that provides the most meaningful and complete information. When a report is prepared in more than one volume, repeat the primary title, add volume number, and include subtitle for the specific volume. On classified documents enter the title classification in parentheses.

Block 5. Funding Numbers. To include contract and grant numbers; may include program element number(s), project number(s), task number(s), and work unit number(s). Use the following labels:

C	- Contract	**PR**	- Project
G	- Grant	**TA**	- Task
PE	- Program Element	**WU**	- Work Unit Accession No.

Block 6. Author(s). Name(s) of person(s) responsible for writing the report, performing the research, or credited with the content of the report. If editor or compiler, this should follow the name(s).

Block 7. Performing Organization Name(s) and Address(es). Self-explanatory.

Block 8. Performing Organization Report Number. Enter the unique alphanumeric report number(s) assigned by the organization performing the report.

Block 9. Sponsoring/Monitoring Agency Name(s) and Address(es). Self-explanatory.

Block 10. Sponsoring/Monitoring Agency Report Number. *(If known)*

Block 11. Supplementary Notes. Enter information not included elsewhere such as: Prepared in cooperation with...; Trans. of...; To be published in.... When a report is revised, include a statement whether the new report supersedes or supplements the older report.

Block 12a. Distribution/Availability Statement. Denotes public availability or limitations. Cite any availability to the public. Enter additional limitations or special markings in all capitals (e.g. NOFORN, REL, ITAR).

- **DOD** - See DoDD 5230.24, "Distribution Statements on Technical Documents."
- **DOE** - See authorities.
- **NASA** - See Handbook NHB 2200.2.
- **NTIS** - Leave blank.

Block 12b. Distribution Code.

- **DOD** - Leave blank.
- **DOE** - Enter DOE distribution categories from the Standard Distribution for Unclassified Scientific and Technical Reports.
- **NASA** - Leave blank.
- **NTIS** - Leave blank.

Block 13. Abstract. Include a brief *(Maximum 200 words)* factual summary of the most significant information contained in the report.

Block 14. Subject Terms. Keywords or phrases identifying major subjects in the report.

Block 15. Number of Pages. Enter the total number of pages.

Block 16. Price Code. Enter appropriate price code *(NTIS only)*.

Blocks 17. - 19. Security Classifications. Self-explanatory. Enter U.S. Security Classification in accordance with U.S. Security Regulations (i.e., UNCLASSIFIED). If form contains classified information, stamp classification on the top and bottom of the page.

Block 20. Limitation of Abstract. This block must be completed to assign a limitation to the abstract. Enter either UL (unlimited) or SAR (same as report). An entry in this block is necessary if the abstract is to be limited. If blank, the abstract is assumed to be unlimited.

★U.S.GPO:1991-0-[illegible]-935